

UTTAC-89, 2020

UTTAC

ANNUAL REPORT 2019

TANDEM ACCELERATOR COMPLEX
Research Facility Center for Science and Technology
University of Tsukuba

<https://www.tac.tsukuba.ac.jp/>

UTTAC

ANNUAL REPORT 2019

April 1, 2019– March 31, 2020

UTTAC-89, 2020

Editors : Tetsuaki Moriguchi, Kimikazu Sasa, Yoshihiro Yamato, Masumi Matsumura,
Masao Sataka, Hiroshi Naramoto, Eiji Kita, and Hiroshi Kudo (editor-in-chief)

UTTAC ANNUAL REPORT is a series of issues, which include annual reports of
Tandem Accelerator Complex, Research Facility Center
for Science and Technology, University of Tsukuba.

Copyright © 2019 by Tandem Accelerator Complex, Research Facility Center
for Science and Technology, University of Tsukuba and individual contributors.

All reports are written on authors' responsibility and thus the editors are not liable
for the contents of the report.

Tandem Accelerator Complex, Research Facility Center for Science and Technology,
University of Tsukuba
Tennodai 1-1-1, Tsukuba, Ibaraki 305-8577, Japan

annual@tac.tsukuba.ac.jp

Cover: [Hydrogen aggregates of ten- \$\mu\$ m size in H-charged Al \[AIP Adv. 9 \(2019\) 105111\],
from Report 4.2.](#)

PREFACE

This annual report covers researches carried out at University of Tsukuba Tandem Accelerator Complex (UTTAC) during the fiscal year 2019 (1 April 2019 ~ 31 March 2020). The topics include not only accelerator-based researches using the 6MV Pelletron and 1MV Tandetron accelerators, but also radioisotope-based researches including positron annihilation spectroscopy and Mössbauer spectroscopy.

September 1, 2020
Editorial board



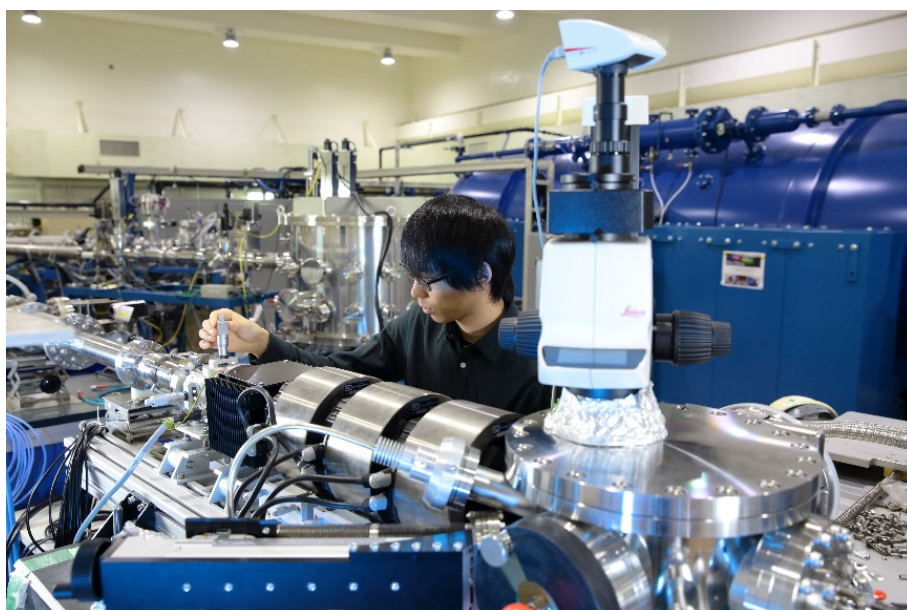
High-school students visited far from Kagoshima prefecture. In FY2019, we had 428 visitors including 290 high-school students. Social activity of UTTAC to promote physical science to young generation has been continued in addition to science and technology researches.

DEEP CONTRIBUTION TO MACHINE OPERATION EXPECTED FOR STUDENTS

Reduction of labor costs in Japan eventually led to the reduced number of technical staff at UTTAC. As a result, users are required more and more to proceed with their experimental researches under minimum technical support. Even partial operation of the accelerator and the beam-transport system by the users, especially students, might be very helpful for the UTTAC staff.



Graduate students watching the control panel of the 6MV tandem accelerator, with a little tension.



Graduate student carefully adjusting the slit system to shape a He micro-beam for materials analysis.

CONTENTS

1. ACCELERATOR AND RELATED FACILITIES

1.1	Accelerator operation 2019	1
1.2	Current distribution of ions accelerated by the 6MV tandem accelerator.....	3
1.3	Air dose rates during deuteron irradiation.....	5

2. NUCLEAR AND ATOMIC PHYSICS

2.1	Studies of nuclear polarization in different types of Si targets.....	7
2.2	Developments of RF system for rotating magnetic field.....	8

3. ACCELERATOR MASS SPECTROMETRY

3.1	Performance report of the Tsukuba 6 MV multi-nuclide AMS system in fiscal 2019.....	10
3.2	Reconstruction of ^{14}C introduction history in the Japan Sea using coral samples.....	12
3.3	Regional dependences of ^{10}Be and ^{36}Cl concentrations in rainwater.....	14
3.4	The Performance of Iodine-129 AMS measurements at the University of Tsukuba in FY 2019.....	16
3.5	Anthropogenic iodine-129 depositions at the Japan Sea and Pacific sides of the archipelago, during 2017-2018.....	18

4. BEAM AND ISOTOPE APPLICATIONS

4.1	Vacancy-type defects in Mg implanted GaN studied by positron annihilation spectroscopy..	20
4.2	Microscopic 3-dimensional mapping of hydrogen bubbles in Al by elastic recoil detection analysis under transmission geometry.....	22
4.3	Depth resolution of hydrogen distribution in Al measured with elastic recoil detection analysis under transmission geometry.....	24
4.4	Trial of ^7Li depth profile determination by $^7\text{Li}(p, \alpha)^4\text{He}$ NRA.....	26
4.5	Depth profiling of lithium by use of TOF-E telescope ERDA.....	28
4.6	High magnetic field Mössbauer study on an antiferromagnetic layered FeNi nitride, FeNiN..	30
4.7	Simultaneous detection of light elements under non-Rutherford scattering.....	32
4.8	Recombination effect in the output pulse height of superconducting tunnel junction for the incidence of keV ions.....	34
4.9	Heteroepitaxial growth of thin films of the perovskite oxynitride CaTaO_2N by reactive magnetron sputtering.....	36
4.10	Electric properties of magnesium titanium oxynitride thin films.....	38

5. BEAM IRRADIATION EFFECT

5.1 Study on microalgae mutagenesis with ^{15}N -resonant nuclear reaction.....	40
--	----

6. LIST OF PUBLICATIONS AND PRESENTATIONS

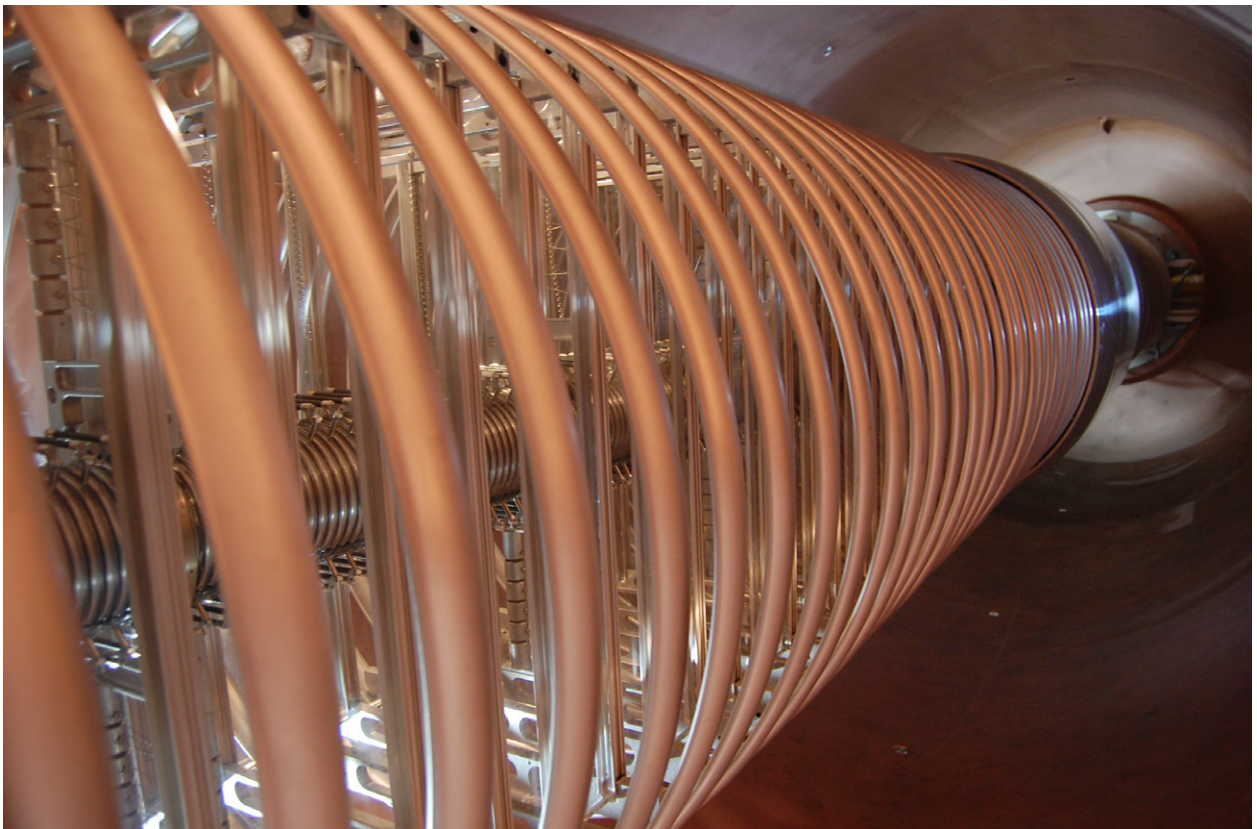
6.1 Journals	42
6.2 Reviews and books.....	47
6.3 Poster or oral presentations at academic meetings.....	48
6.4 UTTAC seminars.....	56

7. THESES	58
------------------------	----

8. LIST OF PERSONNEL	59
-----------------------------------	----

1.

ACCELERATOR AND RELATED FACILITIES



Inside view of the UTTAC 6MV tandem accelerator. The acceleration tube is surrounded by metal hoops of 1-m diameter.

1.1 Accelerator operation 2019

K. Sasa, S. Ishii, Y. Tajima, T. Takahashi, Y. Yamato, M. Matsumura, T. Moriguchi

1 MV Tandetron accelerator

The operating time and the experimental beam time of the 1 MV Tandetron accelerator were 335.7 and 139.5 hours, respectively, during the total service time in fiscal 2019. The total number of operation days was 49 in fiscal 2019. A total of 28 research programs was carried out and a total of 147 researchers used the 1 MV Tandetron accelerator in fiscal 2019. Figures 1 and 2 show classification of the accelerated ions and of the experimental purposes, respectively. This accelerator was maximally used for RBS/ERDA which occupied 64% of the beam time.

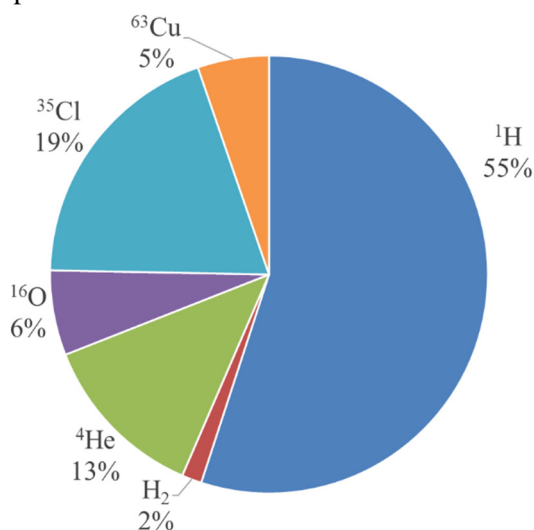


Fig. 1. Accelerated ions by the 1 MV Tandetron accelerator in fiscal 2019.

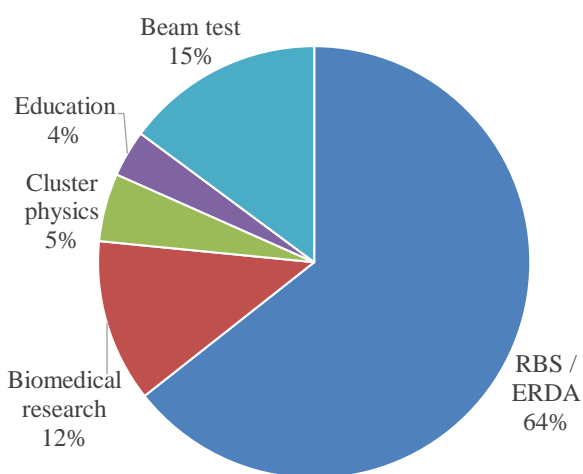


Fig. 2. Purpose of use of the 1 MV Tandetron accelerator in fiscal 2019.

An alignment adjustment of the Tandetron accelerator was performed in March 2019 [1] because there was a beam-axis deviation after the earthquake in 2011. Figure 3 shows the comparison of beam transmissions from the front of the accelerator tank to the C course chamber for 2003 and 2019. The beam transmission was recovered after the alignment adjustment, especially it was improved in the high energy range than before.

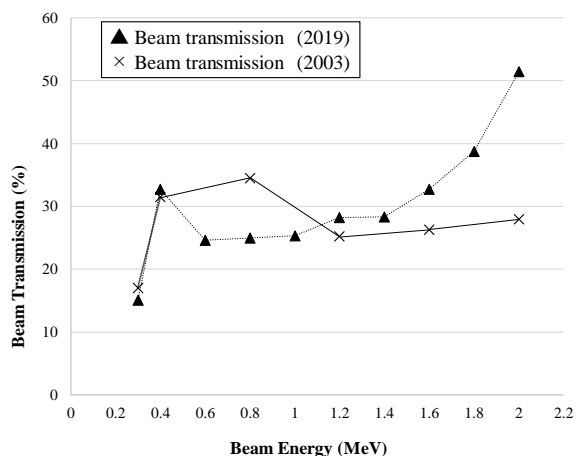


Fig. 3. Comparison of beam transmissions from the front of the accelerator tank to the C course chamber for 2003 and 2019.

6 MV Pelletron tandem accelerator

The operating time and the experimental beam time of the 6 MV Pelletron tandem accelerator were

1349.7 and 1036.6 hours, respectively, during the total service time in fiscal 2019. The total number of operation days was 112 in fiscal 2019. A total of 53 research programs was carried out and a total of 277 researchers used the 6 MV Pelletron tandem accelerator in fiscal 2019. Figure 4 shows the beam time histogram with respect to the terminal voltage. Figures 5 and 6 show classification of the accelerated ions and of the experimental purposes, respectively. The operating time at terminal voltages of 5 and 6 MV accounted for 92% of all the beam time. The terminal voltage at 5 MV was mainly used for ^{129}I AMS. On the other hand, the terminal voltage at 6 MV was applied for ^{36}Cl AMS, nuclear physics and the radiation resistant test of semiconductors. This accelerator was used most often for AMS which occupied 76% of the beam time. The next 11% was occupied by nuclear physics using polarized beams, mainly for study of nuclear moments of unstable nuclei.

In 2019, Typhoon No.19 caused a lot of detriment at the accelerator facility on October. The cooling water chiller for the 1 MV Tandetron and the peripheral equipment were damaged by flooding. In addition, radiation posts were not capable of being used for monitoring. They will be restored with the reconstruction budget in 2020.

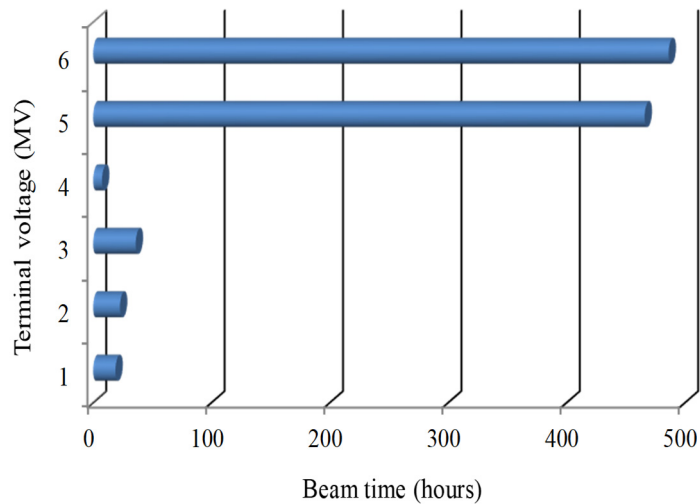


Fig. 4. Beam time histogram as a function of the terminal voltage for the 6 MV Pelletron tandem accelerator in fiscal 2019.

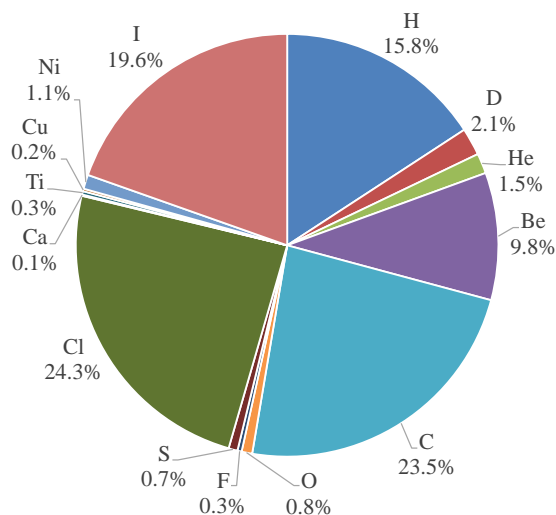


Fig. 5. Accelerated ions for the 6 MV Pelletron tandem accelerator in fiscal 2019.

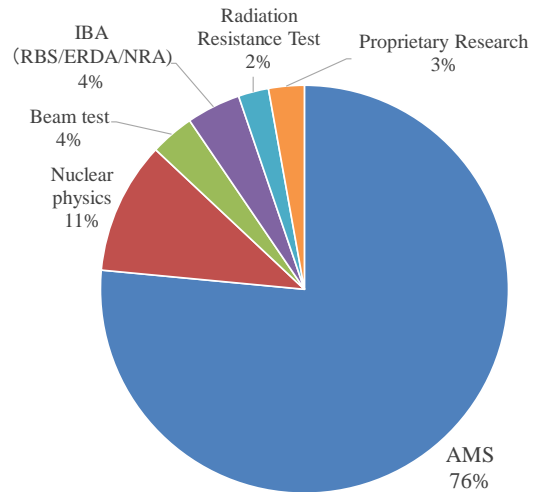


Fig. 6. Purpose of use of the 6 MV Pelletron tandem accelerator in fiscal 2019.

Reference

- [1] K. Sasa et al., UTTAC ANNUAL REPORT 2018, UTTAC-88 (2019) 1.

1.2 Current distribution of ions accelerated by the 6MV tandem accelerator

M. Sataka, T. Takahashi, H. Naramoto, H. Kudo, K. Sasa

Beam current of ions accelerated by the 6MV tandem accelerator has been investigated as a function of the ion charge state since 3 year ago [1-3], mainly at acceleration voltages of 1, 3 and 6 MV. Here, we describe the ion current distribution only for the 6 MV terminal voltage, hence the measured highest charge state of the ion gives the highest energy of the ion obtained by this accelerator. In this fiscal year, Ca, Ti, and Cu ion were newly tested.

Figure 1 shows the beam current distributions of Cu^{n+} as a function of the ion charge state n at a terminal voltage of 6 MV. Either Ar gas or a carbon foil was used as a charge-changing stripper at the high-voltage terminal. The Ar gas pressure was about 5-7 μPa , and the thickness of the carbon foil was about 5 $\mu\text{g}/\text{cm}^2$. The ion current distribution for the foil stripper shifts to higher charge state by about 5 than for the Ar gas stripper. The practical maximum energy of 84 MeV is obtained for Cu^{13+} using the foil stripper.

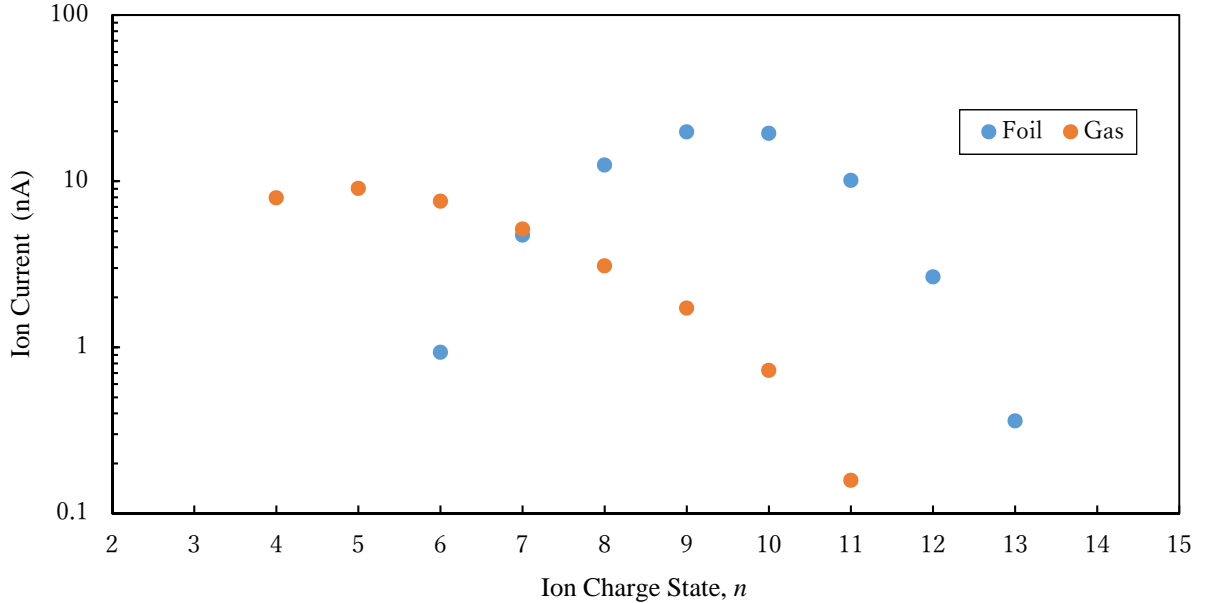


Fig. 1. Beam current distribution of Cu^{n+} for the terminal voltage of 6 MV. Either gas or foil strippers was used at the high-voltage terminal.

We have tested injection of negatively charged molecular ions to the high-voltage terminal. In this year, molecular ions of Ca and Ti hydrides were tested. Since the molecular ions break up into the constituent atoms when they pass through the charge-stripper, the accelerated ion energy cannot be determined uniquely by the terminal voltage and the ion charge state after acceleration. The maximum acceleration energy in this test was slightly less than 66 and 78 MeV for Ca, and Ti, respectively. The slight energy differences from the monoatomic cases are due to the extremely lighter mass of the constituent H than that of Ca or Ti.

Table 1 shows the ion current distribution of Ca and Ti, together with the previous data for Al, Mo, and W. Furthermore, Table 2 shows the ion charge and ion energy obtained in the case of negative atomic-ion injection at the 6 MV terminal voltage, which were investigated from 2016 to 2019.

Table 1. Ion current distribution of N, Al, Ca, Ti, Mo and W at the 6 MV terminal voltage. The measured beam intensities are shown by the symbols: ○: $\geq 1\text{nA}$, △: $\leq 1\text{nA}$. Shown in red are the data with the foil stripper.

charge						
state	N	Al	Ca	Ti	Mo	W
14						
13						
12				△		
11				○		△
10			△	○	△	△
9		○	△	○	○	○
8		○	△	○	○	○
7		○		○	○	
6	△	○	△	○	○	
5	○	○	△	○	○	
4	○			○	○	
3	○			○		
2	○					
1						

Table 2. Summary of the acceleration investigation for negative atomic ion injection at the 6 MV terminal voltage from 2016 to 2019. The measured beam intensity is shown by the symbols: ○: $\geq 1\text{nA}$, △: $\leq 1\text{nA}$. Shown in red are the data with the foil stripper.

charge	energy																		
state	(MeV)	H	He	Li	B	C	O	F	Al	Si	S	Cl	Ca	Ni	Cu	Br	Ag	I	Au
14	90															△	△	○	△
13	84														△	△	△	○	△
12	78													△	○	○	○	○	○
11	72										△			○	○	○	○	○	○
10	66									○	○	○	△	○	○	○	○	○	○
9	60								○	○	○	○	△	○	○	○	○	○	○
8	54						○	○	○	○	○	○	△	○	○	○	○	○	○
7	48						○	○	○	○	○	○		○	○	○	○	○	
6	42					○	○	○	○	○	○	○	△	○	○	○	○		
5	36				○	○	○	○	○	○	○	○	△	○	○	○	○		
4	30				○	○	○	○	△	○	○	○		○	○	○			
3	24			○	○	○	○	○		○	○	○		○					
2	18		○	○	○	○	○	○			○	○							
1	12	○	○	○															

References

- [1] M. Sataka et al., UTTAC Annual Report 2016, UTTAC-86 (2017) 9.
- [2] M. Sataka et al., UTTAC Annual Report 2017, UTTAC-87 (2018) 5.
- [3] M. Sataka et al., UTTAC Annual Report 2018, UTTAC-88 (2019) 5.

1.3 Air dose rates during deuteron irradiation

T. Moriguchi, M. Matsumura, K. Sasa, S. Ishii, T. Takahashi, Y. Yamato

Monitoring air dose rates is necessary for radiation safety management in accelerator facilities. In FY2019, as a test beam, deuteron was accelerated by the 6 MV Pelletron tandem accelerator for the first time. We measured air dose rates in the radiation controlled area during deuteron irradiation. These data are expected to be useful for the radiation safety in UTTAC.

Figure 1 shows the layout of the 6 MV Pelletron tandem accelerator facility. A deuteron beam was extracted from Polarized ion source (PIS) or SNICS-II (S2). The beam energy was changed from 3 to 12 MeV, and the beam current was approximately 30 nA. In the present measurement, tantalum (Ta) and carbon (C) were used as beam stoppers. These stoppers were installed at three positions which are indicated by solid arrows in Fig. 1. Air dose rates were measured by three pairs of area monitors for gamma-ray (DAM-102, Hitachi Ltd.) and neutron (DAM-251, Hitachi Ltd.). These area monitors are located at the shielding walls which are indicated by dashed arrows in Fig. 1. Irradiation time was set to more than ten minutes to stabilize air dose rates. To compare the results of deuteron irradiation with those for proton, we also measured air dose rates during 12 MeV proton irradiation. The proton beam current was adjusted to approximately 300 nA which is acceptable for radiation safety.

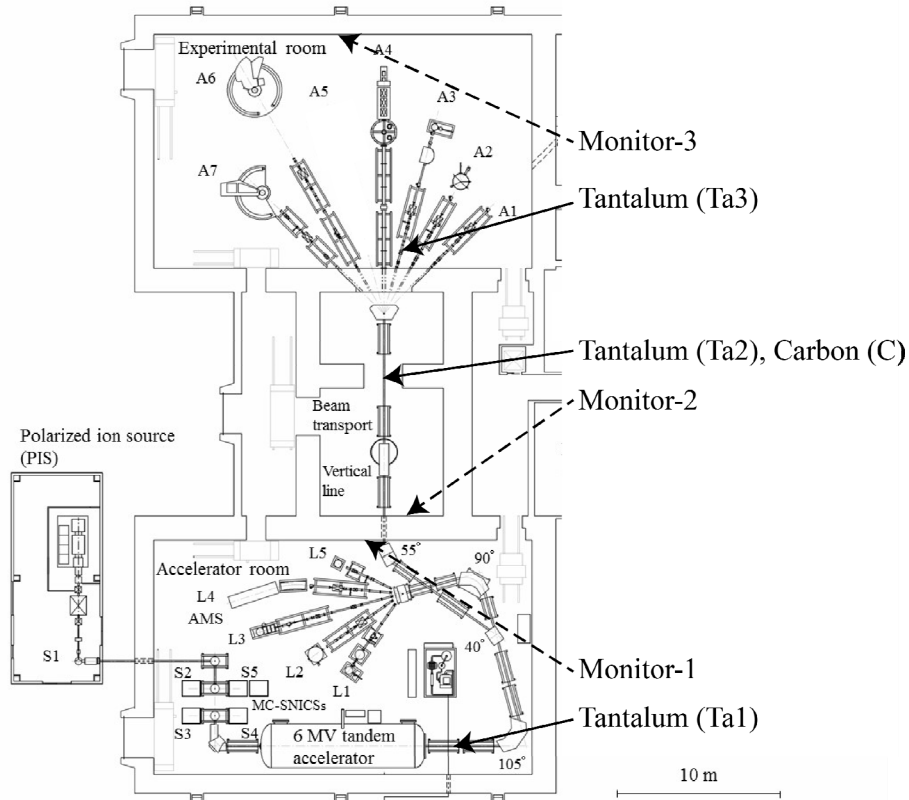


Fig. 1. Layout of the 6 MV Pelletron tandem accelerator facility. Solid arrows indicate the positions of beam stoppers: tantalum (Ta1, Ta2 and Ta3) and carbon (C). Dashed arrows indicate the positions of three pairs of area monitors for gamma-ray and neutron (Monitor-1, Monitor-2 and Monitor-3).

Figure 2 shows air dose rates measured by the nearest area monitor to the irradiated stopper. For tantalum stoppers, air dose rates of both gamma-ray and neutron during deuteron irradiation are lower than those during 12 MeV proton irradiation. As shown in Fig. 2 (b), for irradiation with 6 and 8 MeV deuterons, the air dose rates for tantalum are lower than for carbon. This trend is consistent with the case of 22 MeV deuteron [1]. These results suggest that for deuteron irradiation tantalum is one of the effective materials for reducing air dose rates of both gamma-ray and neutron. For proton irradiation, the tantalum stopper seems effective for reducing air dose rate of gamma-ray, while the carbon stopper seems effective for reducing that of neutron, as shown in Fig. 2 (b). For the radiation safety management in UTTAC, we will collect additional data of air dose rates by varying beam stoppers and radiation shields.

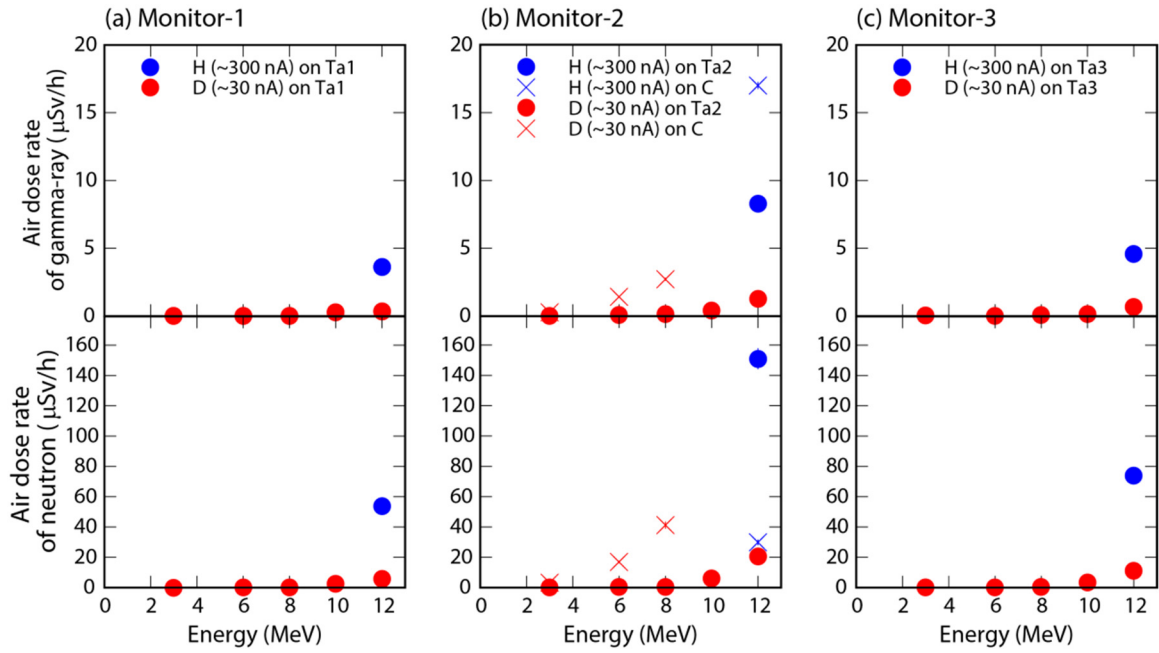


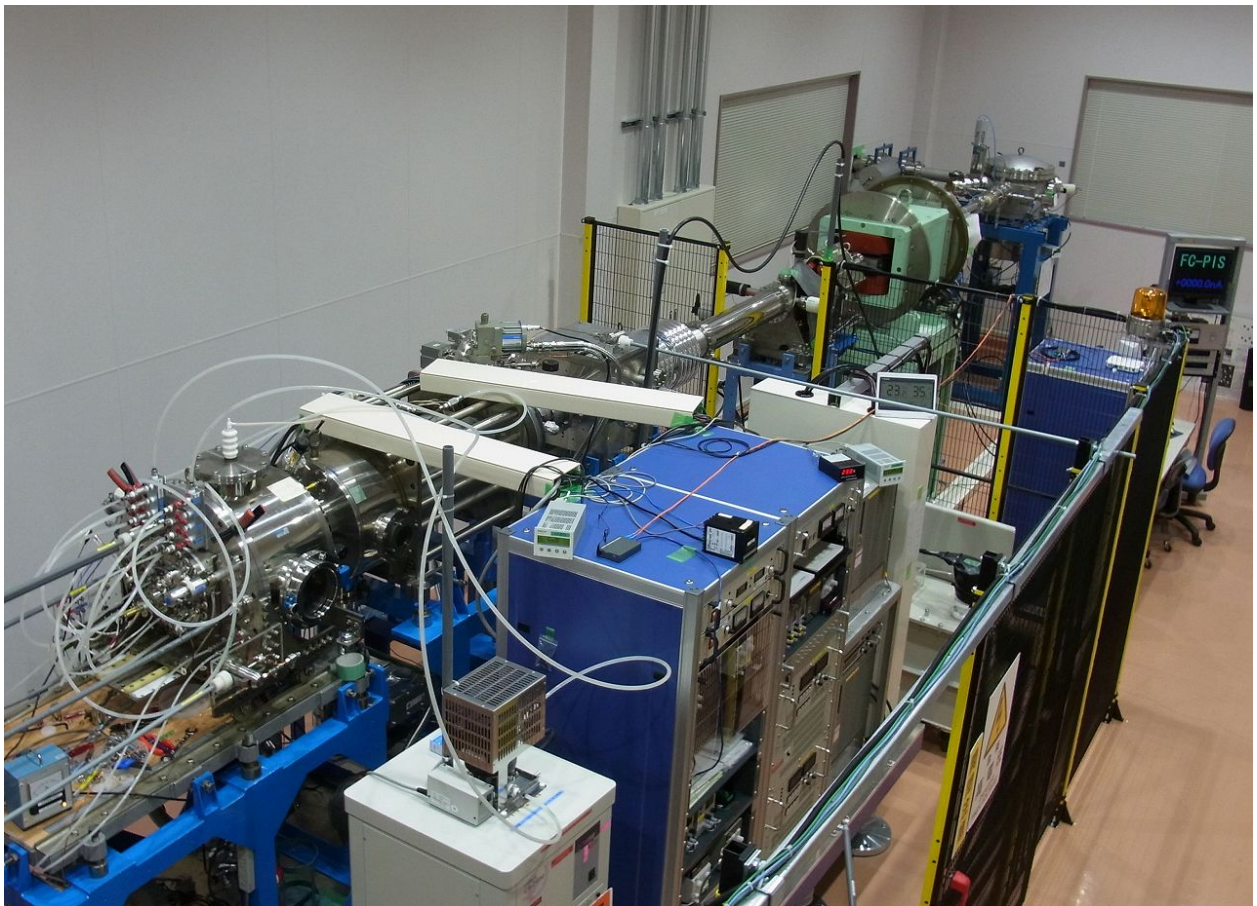
Fig. 2. Air dose rates of gamma-ray (upper panels) and neutron (lower panels) measured by (a) Monitor-1, (b) Monitor-2 and (c) Monitor-3. These results were obtained by the nearest area monitor to the irradiated stopper. Blue and red symbols represent the results of proton (H) with approximately 300 nA and deuteron (D) with approximately 30 nA irradiations, respectively. Circles and crosses represent the results for tantalum (Ta1, Ta2 and Ta3) and carbon (C) stoppers, respectively. Note that backgrounds were already subtracted.

Reference

[1] K. Shima, UTTAC Report No. 12, UTTAC-J-12 (2004) 3 (in Japanese).

2.

NUCLEAR AND ATOMIC PHYSICS



Spin-polarized ion source

2.1 Studies of nuclear polarization in different types of Si targets

A. Ozawa, T. Moriguchi, Y. Yamato, M. Mukai, R. Kagesawa, K. Tomita, T. Yamaguchi

We are attempting to produce polarized unstable nuclei by using polarized proton beams for the aim of measuring nuclear moments of unstable nuclei. In FY2018, we have succeeded to observe magnetic moments of ^{25}Al and ^{29}P at $E_p=12$ MeV with a Si target (n-type, low-impedance (n-Low)) [1]. In FY2019, we have studied nuclear polarization produced in the different types of Si targets. In this time, we tried Si (n-Low), Si (n-High), Si (p-Low) and Si (p-High).

We checked polarization degree in the different targets by using nuclear magnetic resonance system for β -rays (β -NMR system). Experimental setup and experimental procedure are the same as those in the previous measurement [2]. In the present work, a 0.5 mm thick Si target placed in our β -NMR system was irradiated with the polarized proton beams accelerated to 12 MeV by the 6 MV tandem accelerator. Proton polarization-degree was about 70 %. In this work, to obtain the polarization degree for ^{29}P in our β -NMR system, we changed the radio frequency (RF) with the fixed static magnetic field (about 1.6 kG). Figure 1 shows the NMR spectra observed for the different Si targets. Clear dips at 2.95 MHz correspond to the magnetic moment of ^{29}P (1.2349 n.m.). Depths of the dips from those without RF correspond to the polarization degrees. We observed the large polarization degrees for Si (n-High) and Si (p-High), respectively. The large target dependence for the polarization degree may suggest the difference of hyperfine interactions inside the Si targets. In further studies, we will measure relaxation times and precise resonance dips to investigate hyperfine interactions inside the Si targets.

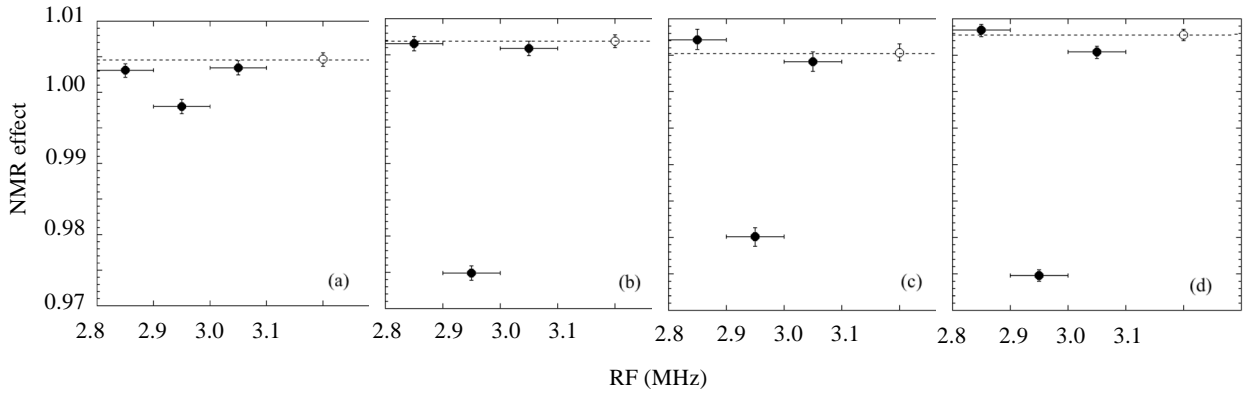


Fig. 1. Typical NMR spectra measured by using the 12 MeV polarized proton beams with different types of Si targets ((a) Si (n-Low), (b) Si (n-High), (c) Si (p-Low) and (d) Si (p-High)). Open circles are data without RF.

References

- [1] A. Ozawa et al., UTTAC ANNUAL REPORT 2018, UTTAC-88 (2019) 7.
- [2] A. Ozawa et al., UTTAC ANNUAL REPORT 2017, UTTAC-87 (2018) 7.

2.2 Developments of RF system for rotating magnetic field

K. Tomita, A. Ozawa, T. Moriguchi, M. Mukai, R. Kagesawa

Magnetic moment ($\pm\mu$) is one of the important physical quantities for nuclear structure. A technique called β -NMR is used to measure the nuclear magnetic moment of unstable nuclei. Using β -NMR, nuclear magnetic resonance is detected by observing the asymmetry of β -rays emitted from unstable nuclei with nuclear polarization. The sign of the nuclear magnetic moment is decided by using a rotating magnetic field produced by a pair of two radiofrequency (RF) coils whose central axes are orthogonal to each other [1]. RF signals for both coils are necessary to adjust to the same amplitude and frequency under 90-degree phase difference to rotate the magnetic field. If the sign of the nuclear magnetic moment is positive, its resonance is detected in the right (left)-handed rotational field for upward (downward) static magnetic field. In FY2019, we were attempting to develop the RF system, including RF coils.

We have made a pair of RF coils with a diameter of 11.3 mm, a gap of 12.0 mm and a size of 30.6 mm (Fig. 1). Copper was used for wire ($\phi 1.1$ mm) of coils. Figure 2 shows a schematic diagram of the RF system. The frequency of the RF coil was set to 3.05–3.15 MHz by using a function generator. The amplitude was adjusted by an attenuator. A cable delay was added to Coil-A for the ± 90 -degree phase shift. The variable condensers were used to adjust the resonance frequencies of the coils. It is important to confirm that the resonance frequencies of the two pairs of coils can be changed independently without interference which might be unintentionally caused by the mutual inductance of the coils.

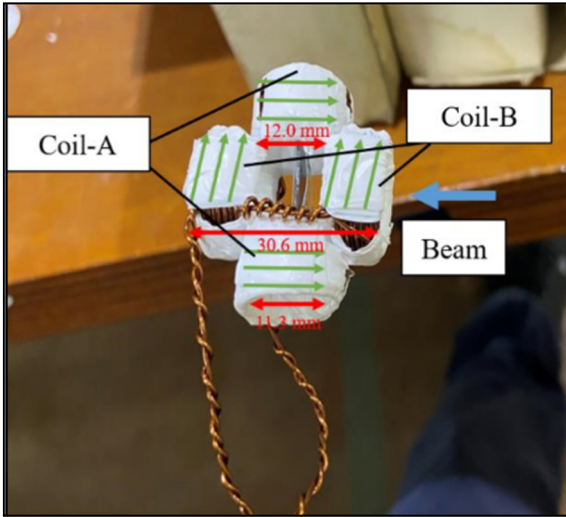


Fig. 1. RF coil for a rotating magnetic field. Coil-A and Coil-B are perpendicular and parallel to the spin-polarized beam, respectively. Green arrows indicate the assumed positive direction of the electric current.

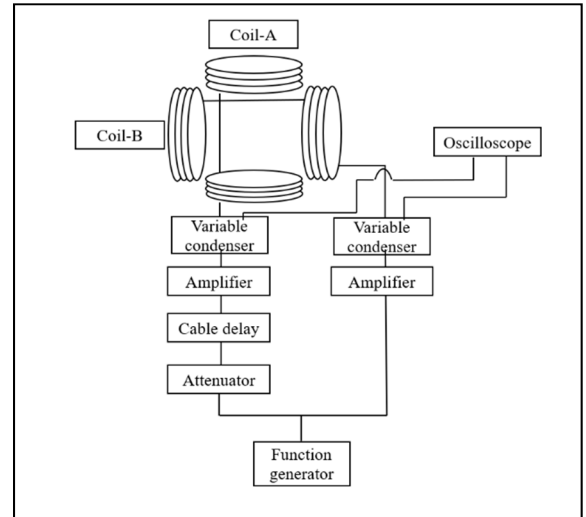


Fig. 2. Schematic diagram of the RF system.

Figure 3 shows the RF signals observed by the oscilloscope. As shown in Fig. 3, we added a 90 (250) ns delay to Coil-A for the -90 ($+90$) degree phase shift. RF signals in Fig. 3 (a) and (b) correspond to right-

and left-handed rotating magnetic fields, respectively.

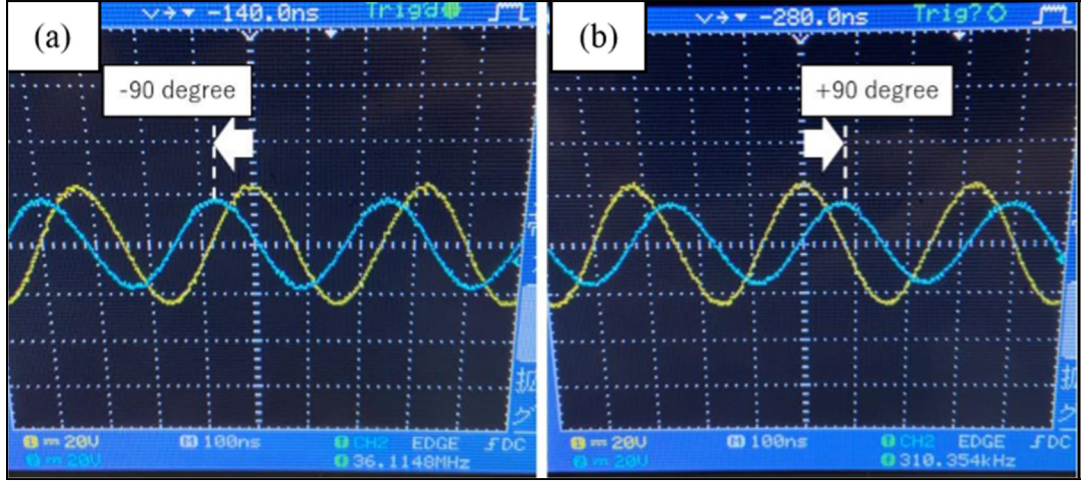


Fig. 3. The RF signals observed by the oscilloscope with (a) 90 ns and (b) 250 ns cable delays. Blue and yellow curves indicate RF signals for Coil-A and Coil-B, respectively.

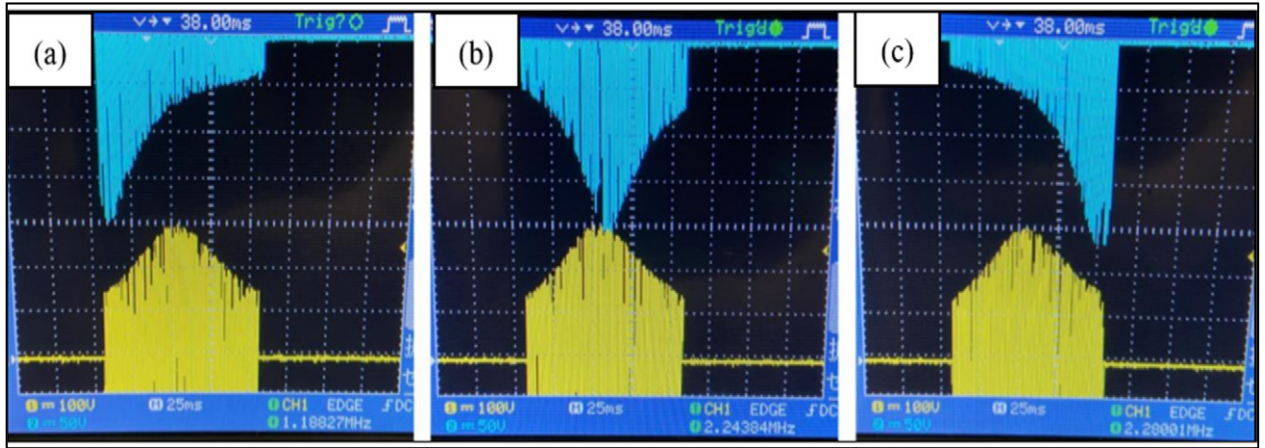


Fig. 4. Amplitudes of RF signals modulated from 3.05 to 3.15 MHz during 100 ms, measured for Coil-A (blue) and Coil-B (yellow). Labels (a), (b), and (c) correspond to three capacitance values of the variable condenser for Coil-A.

Figure 4 shows the amplitudes of RF signals modulated from 3.05 to 3.15 MHz during 100 ms, which were measured for three capacitance values changed by the variable condenser for Coil-A. As seen in Fig. 4, while the resonance frequency for Coil-A changes considerably, that for Coil-B remains unchanged in the middle of the modulation time. This indicates that both resonance frequencies can be controlled independently without any noticeable interference.

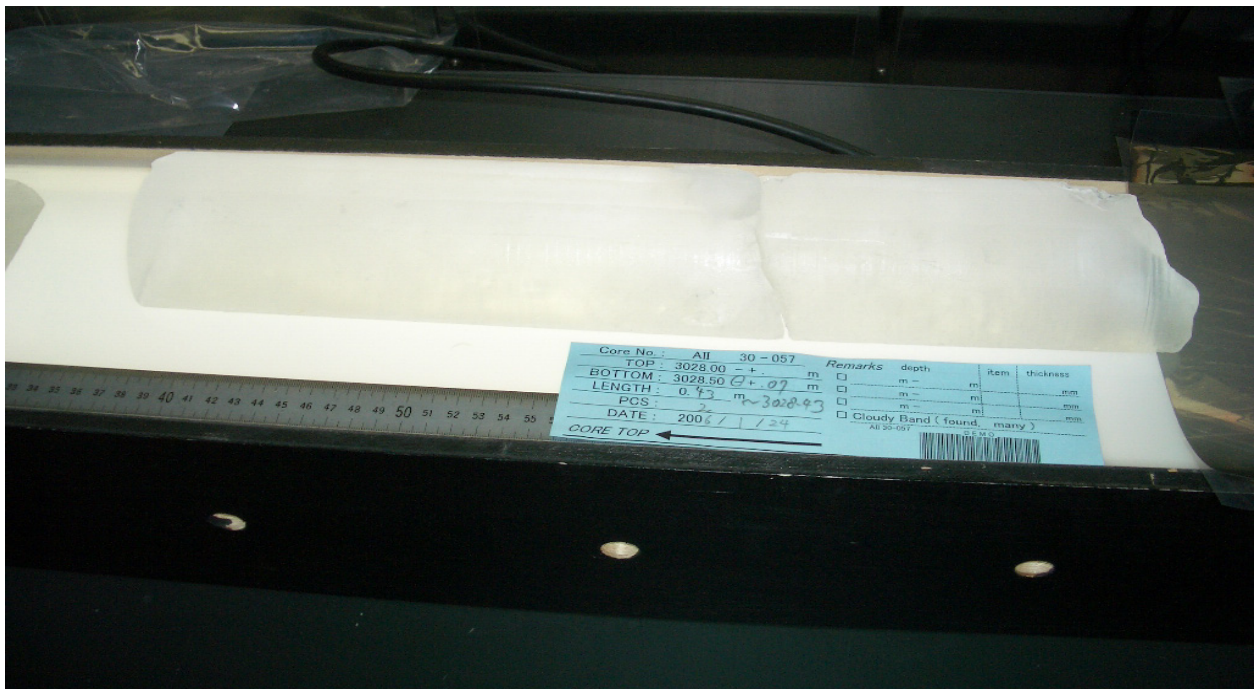
We plan to determine the sign of the nuclear magnetic moment for ^{29}P using the present RF system.

Reference

[1] Y. Ishibashi et al., UTTAC annual report 2014, UTTAC-84 (2014) 8.

3.

ACCELERATOR MASS SPECTROMETRY



AMS sample of the ice (cut to ~50 cm length) obtained from 3028-meter underground of the Dome Fuji, Antarctica, which informs us of the global environment 0.72 million years ago.

3.1 Performance report of the Tsukuba 6 MV multi-nuclide AMS system in fiscal 2019

K. Sasa, T. Takahashi, Y. Ochiai, M. Matsumura

The AMS system on the 6 MV tandem accelerator was operated for a total of 61 days and 792.9 hours in fiscal 2019. We measured 694 samples in total dealing with rare radionuclides such as ^{10}Be , ^{14}C , ^{36}Cl and ^{129}I shown in Table 1. Figure 1 shows details of the measured nuclides. Figure 2 shows monthly-measured nuclides from April 2019 to March 2020. ^{129}I was measured most frequently in fiscal 2019 in order to investigate the radioactive contamination in surface soils, and to trace the oceanic circulation in the Japan Sea. ^{14}C was measured for ^{14}C introduction history in the Japan Sea using coral samples. ^{36}Cl was applied for tracing cosmic ray events remaining in the ice core. In addition, ^{10}Be and ^{36}Cl were measured to investigate regional dependence of their concentrations in rainwater.

Table 1. Number of measured samples in fiscal 2019.

Nuclides	Number
Be-10	85
C-14	187
Cl-36	165
I-129	257
Total	694

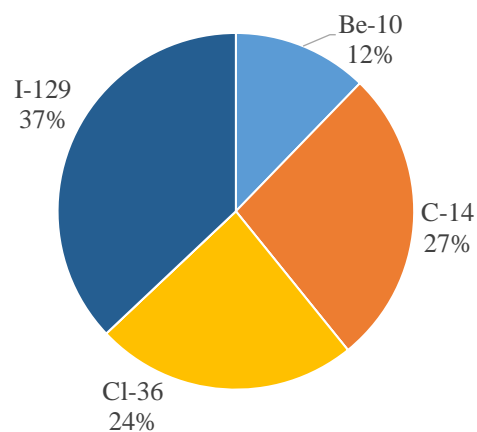


Fig. 1. Measured nuclides by the multi-nuclide AMS system in fiscal 2019.

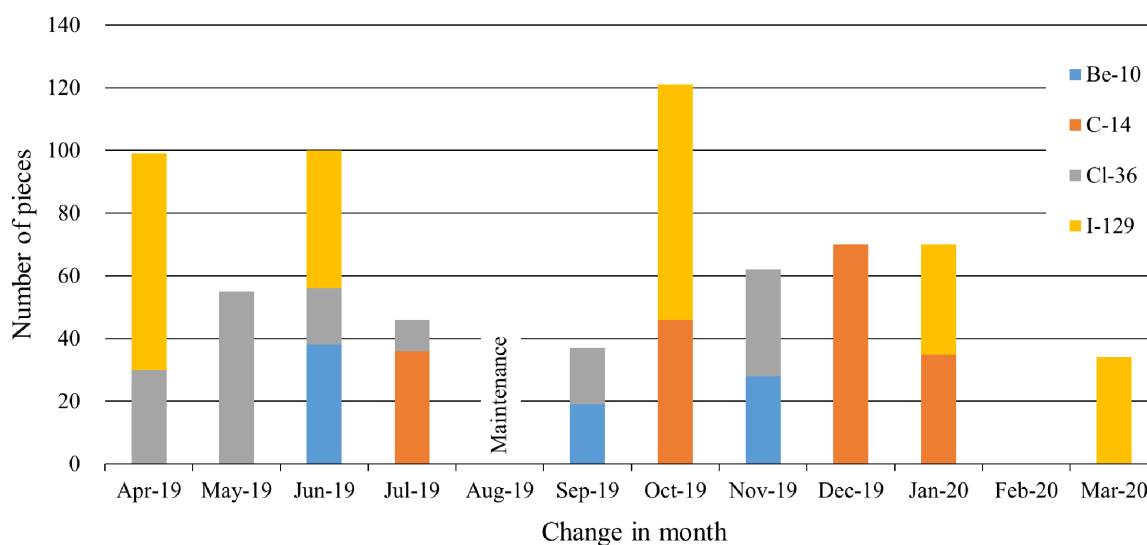


Fig. 2. Monthly-measured nuclides by the multi-nuclide AMS system from April 2019 to March 2020.

The low-background measuring methods were developed for ^{36}Cl AMS by comparing beam conditions at 6 MV. We measured the $^{36}\text{Cl}/\text{Cl}$ background under different beam conditions, i.e., $^{36}\text{Cl}^{5+}$ with the beam energy of 36.0 MeV (using an argon gas stripper), $^{36}\text{Cl}^{7+}$ with 48.0 MeV (using a carbon foil stripper), and $^{36}\text{Cl}^{8+}$ with 54.0 MeV (using a carbon foil stripper). The beam transmissions were 22, 15, and 10% for $^{36}\text{Cl}^{5+}$, $^{36}\text{Cl}^{7+}$, and $^{36}\text{Cl}^{8+}$, respectively. Figure 3 shows $^{36}\text{Cl}/\text{Cl}$ background against separation factors between ^{36}Cl and ^{36}S spectrums [1] obtained for the three beam conditions. It is noted that AgCl blank samples used in the measurements were prepared from ACS-grade NaCl (Fisher Scientific, USA). The background ratios of $^{36}\text{Cl}/\text{Cl} \sim 3 \times 10^{-15}$ were achieved for ^{36}Cl AMS.

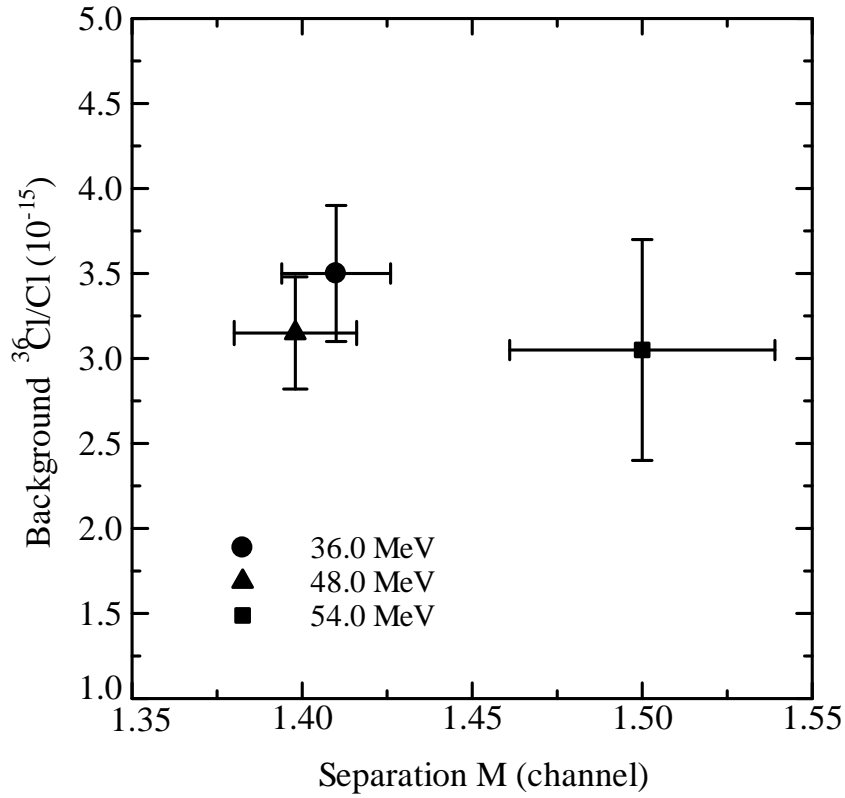


Fig. 3. Background $^{36}\text{Cl}/\text{Cl}$ against separation factors between ^{36}Cl and ^{36}S spectrums for the three beam conditions.

Reference

- [1] S. Hosoya et al., Nucl. Instr. Meth. Phys. Res. B 438 (2018) 131.

3.2 Reconstruction of ^{14}C introduction history in the Japan Sea using coral samples

K. Nishizuka, A. Sakaguchi, T. Omori, K. Sasa, T. Takahashi, M. Matsumura, Y. Ochiai, S. Yamasaki, K. Sueki

A large amount of carbon-14 (^{14}C , $T_{1/2} = 5730$ yr) has been released into the environment by nuclear facilities, and also in nuclear tests conducted by the US and the former USSR in the 1950s and 1960s. Such ^{14}C is quickly oxidized and spreads into the atmosphere as $^{14}\text{CO}_2$, and some part is dissolved in surface seawater and transported to greater depths and to other seas by seawater circulation and/or diffusion. It is known that reef-building corals form annual rings by fixing the carbon dissolved in seawater to their own carbonate skeletons. Therefore, it is possible to reconstruct the isotopic composition of past surface seawater, particularly concerning ^{14}C , by performing isotopic analysis of each annual coral ring.

Studies utilizing the corals in this manner have been conducted in the North West Pacific, from the low latitudes around the equator to the Tsushima Strait which is the northern-most limit of reef-building corals [1–3]. However, no dataset of carbon isotopes before 1966 exists in the study using a coral core sample from the Tsushima Strait, the entrance to the Japan Sea. Although Tsushima Strait is located on the latitude where numerous atmospheric nuclear tests were conducted and the temperature of the seawater in the strait is low compared to other sampling sites, lower ^{14}C concentrations there than in lower latitudes have been reported [3]. In the present study, we measured the carbon isotopic compositions in a coral core collected from Iki Island, Tsushima Strait, in order to reconstruct the history of the introduction of ^{14}C into the Japan Sea since the 1940s (i.e., before any atmospheric nuclear test was conducted).

The coral (*Dipsastraea Speciosa*) cores were collected from Iki Island in the Tsushima Strait in November 2012 and dated using soft X-ray photographs and LA-ICP-MS Sr/Ca ratio measurements [4]. To determine which pretreatment leaching method should be employed, the coral powders (1930s) were leached with different concentrations of hydrochloric acid ($2\text{--}6 \times 10^{-3}$ M). The coral sample residues were analyzed by accelerator mass spectrometry (AMS), powder X-ray crystal structure analysis, scanning electron microscopy, and also by isotope ratio mass spectrometry for stable isotopic composition of carbon and oxygen ($^{13}\text{C}/^{12}\text{C}$, $^{18}\text{O}/^{16}\text{O}$). Using the appropriate pretreatment method, the carbon isotope ratios ($^{14}\text{C}/^{12}\text{C}$, $^{13}\text{C}/^{12}\text{C}$) in annual rings were measured by AMS for 23 samples over the period 1943 to 2011. It should be noted that no remarkable effects were observed on the surfaces of the coral samples after removing surface contamination by hydrochloric acid leaching. Thus, we concluded that no specific chemical leaching was necessary for the actual samples.

Figure 1 shows the variations of $\Delta^{14}\text{C}$, which represents the relative ^{14}C amount [5], in the past surface seawater reconstructed from the annual rings in the coral cores from Iki Island. The $\Delta^{14}\text{C}$ value before commencement of atmospheric nuclear testing was -59 ‰, then increased rapidly from around 1960 before reaching its maximum (147 ‰) in 1971, and then gradually decreased over the following years. While the $\Delta^{14}\text{C}$ values for the 1960s are larger than those in the previous study [3], the reason for this discrepancy is not clear at present. For further discussion of this subject, it is necessary to investigate the crystal structure

of the coral skeleton to determine whether diagenesis occurred, as well as to reconsider the dating method employed. However, the following are conceivable explanations for the higher $\Delta^{14}\text{C}$ values in Iki coral compared to more southern areas such as Guam and Ishigaki island. The Tsushima Current passing around Iki island is a combination of the Kuroshio Current and the Taiwan Warm Current, which stems from the East China Sea. The East China Sea is, in turn, considered to be “an important carbon dioxide sink” [6]. Furthermore, the water temperature around Iki island is lower than that of the low latitude areas of the North Pacific. As is already known, the concentration of ^{14}C in the atmosphere in the early 1960s was high, and therefore, it is possible that Iki island corals reflect the changes in ^{14}C concentration in the atmosphere/surface seawater more sensitively than corals in other areas.

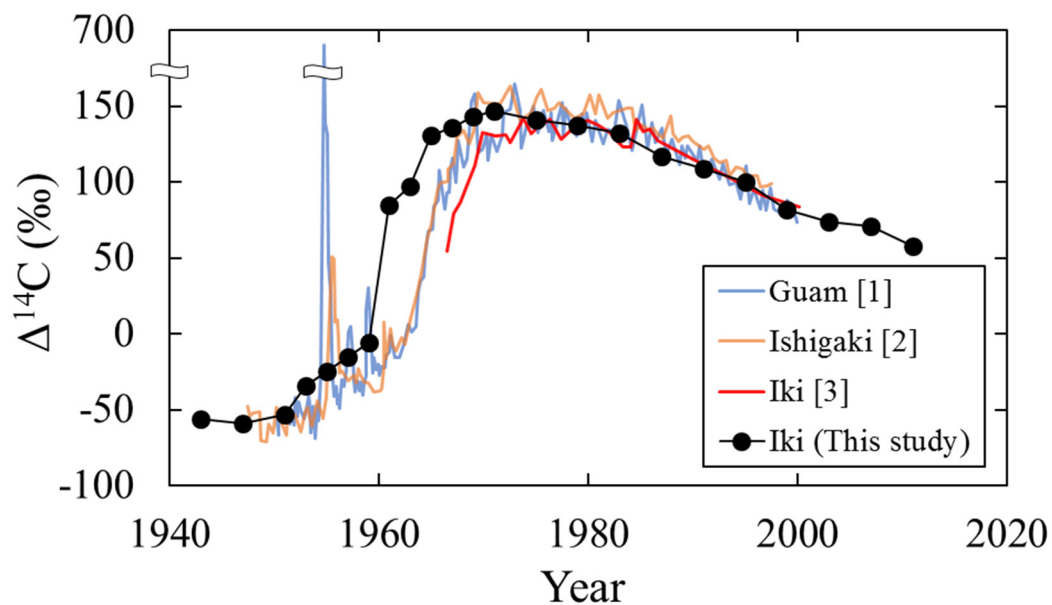


Fig. 1. Variations of $\Delta^{14}\text{C}$ reconstructed from the annual rings in coral cores from Guam [1], Ishigaki [2] and Iki Island ([3] and this study).

References

- [1] A.H. Andrews et al., J. Geophys. Res. Oceans 121 (2016) 6351.
- [2] S. Hirabayashi et al., Geochem. Geophys. Geosyst. 18 (2017) 1608.
- [3] T. Mitsuguchi et al., Geo-Mar. Lett. 36 (2016) 371.
- [4] A. Sakaguchi et al., J. Geophys. Res. Oceans 121 (2015) 4.
- [5] M. Stuiver and H. A. Polach, Radiocarbon 19 (1977) 355.
- [6] C.M. Tseng et al., Geophys. Res. Lett. 38 (2011) L24609.

3.3 Regional dependences of ^{10}Be and ^{36}Cl concentrations in rainwater

Y. Ochiai, K. Sasa, Y. Tosaki¹, T. Matsunaka², T. Takahashi, M. Matsumura, K. Sueki

This study focused on ^{10}Be (half-life = 1.36×10^6 years) and ^{36}Cl (half-life = 3.01×10^5 years), which are produced in the upper atmosphere by reactions between cosmic rays and elements in the atmosphere (e.g. $^{16}\text{O}(\text{p}, \text{X})^{10}\text{Be}$ or $^{40}\text{Ar}(\text{n}, \text{X})^{36}\text{Cl}$). The ^{10}Be and ^{36}Cl concentrations in rainwater were measured at the Pacific side and the Sea of Japan side, to discuss the regional dependencies of seasonal variation.

We have collected monthly rainwater samples in Tsukuba city, Ibaraki ($36^\circ 06' \text{N}$, $140^\circ 06' \text{W}$) since April 2004 and in Nomi city, Ishikawa ($36^\circ 25' \text{N}$, $136^\circ 32' \text{W}$) since July 2017. In this report, ^{10}Be and ^{36}Cl concentrations were analyzed after 2017. Added 0.5 mg of Be carrier, Be^{2+} and Cl^- , which are chemical forms of Be and Cl in the rainwater samples, were extracted by an ion-exchange method. Be^{2+} was precipitated as $\text{Be}(\text{OH})_2$ with 15 M NH_4OH and converted to BeO by heating in an electric furnace at 850°C . Cl^- was precipitated as AgCl with 0.3 M AgNO_3 and washed with ultrapure water and ethanol. ^{10}Be and ^{36}Cl were measured with the accelerator mass spectrometry system at UTTAC [1]. The background values are $^{10}\text{Be}/\text{Be} < 1.0 \times 10^{-15}$ and $^{36}\text{Cl}/\text{Cl} < 3 \times 10^{-15}$, and the precision for both ^{10}Be and ^{36}Cl analysis is $\sim 2\%$. The measurement values were corrected with KN standards prepared by Dr. K. Nishiizumi [2, 3].

Figure 1 shows temporal variations of the (a) ^{10}Be and (b) ^{36}Cl concentrations in rainwater at Tsukuba and Nomi. The ^{36}Cl concentration in September and October 2017 at Nomi could not be analyzed due to a small amount of precipitation and the ^{10}Be concentration in September 2018 at Tsukuba could not be quantified because of experimental failure. The ^{10}Be concentrations ranged from $(6.6 \pm 0.3) \times 10^6$ to $(5.9 \pm 0.6) \times 10^7$ atoms L^{-1} and from $(1.9 \pm 0.1) \times 10^6$ to $(4.7 \pm 1.2) \times 10^7$ atoms L^{-1} at Tsukuba and Nomi, respectively. The ^{36}Cl concentrations ranged from $(1.5 \pm 0.7) \times 10^5$ to $(2.0 \pm 0.1) \times 10^6$ atoms L^{-1} and from $(1.2 \pm 0.7) \times 10^5$ to $(2.6 \pm 0.7) \times 10^6$ atoms L^{-1} at Tsukuba and Nomi, respectively. The concentrations at Tsukuba and Nomi had poor correlation (^{10}Be ; correlation coefficient $r = 0.3$, $p < 0.2$, ^{36}Cl ; $r = 0.2$, $p < 0.6$), therefore it was confirmed that the variations of ^{10}Be and ^{36}Cl concentration had different trend

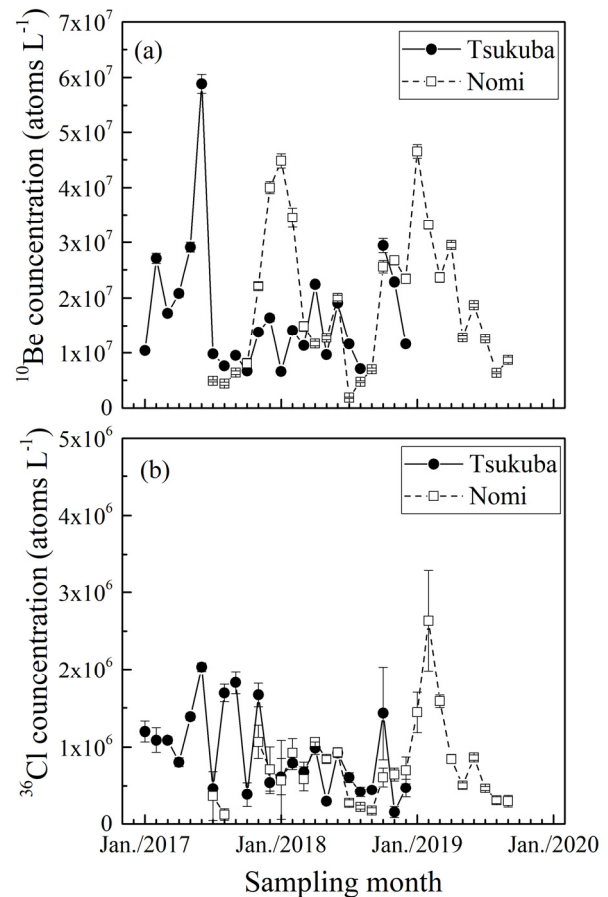


Fig. 1. Temporal variations of ^{10}Be and ^{36}Cl concentration in rainwater at Tsukuba and Nomi.

¹ Geological Survey of Japan, AIST, ² Kanazawa University

between the Pacific side and Sea of Japan side.

Figure 2 gives comparisons of the seasonal variation of (a) ^{10}Be and (b) ^{36}Cl concentrations between Tsukuba and Nomi. The monthly averages of ^{10}Be and ^{36}Cl concentration were calculated. It was noted that the concentrations at Tsukuba were based on the data after April 2004 [2]. In terms of Nomi, the variation of ^{10}Be had a similar trend with Tsukuba in summer while the ^{10}Be concentration was higher than Tsukuba in winter. The strong north-west wind blows down around the Sea of Japan side in winter, which transports much ^7Be from the Arctic region [3] because the production rates of ^7Be in the polar regions are higher than in mid-latitude [4]. Also ^{10}Be is produced much in polar atmosphere, hence, the strong wind contain huge ^{10}Be , which makes high ^{10}Be concentration in rainwater at Nomi. The concentration of ^{36}Cl in winter was also higher than in summer at Nomi, corresponding to the large ^{36}Cl production in the polar regions [4]. In contrast, at Tsukuba, ^{10}Be and ^{36}Cl concentration increased in mid-spring. The strong stratosphere-troposphere exchange occurs around Japan in spring due to the westerly wind. The air mass that has a high concentration of ^{10}Be or ^{36}Cl in the stratosphere is easy to be transported to the boundary layer. Therefore, a high concentrations of ^{10}Be and ^{36}Cl were observed in rainwater at Tsukuba. A similar trend of ^{10}Be was reported on the Pacific side (e.g. [5]).

References

- [1] K. Sasa et al., Nucl. Instr. Meth. Phys. Res. B 437 (2018) 98.
- [2] Y. Ochiai, Master Thesis (2020).
- [3] M. Yamamoto et al., J. Environ. Radioactiv. 86 (2006) 110.
- [4] J. Masarik and J. Beer., J. Geophys. Res-Atmos. 114 (D11) (2009) D11103.
- [5] T. Yamagata et al., Nucl. Instr. Meth. Phys. Res. B 455 (2019) 265.

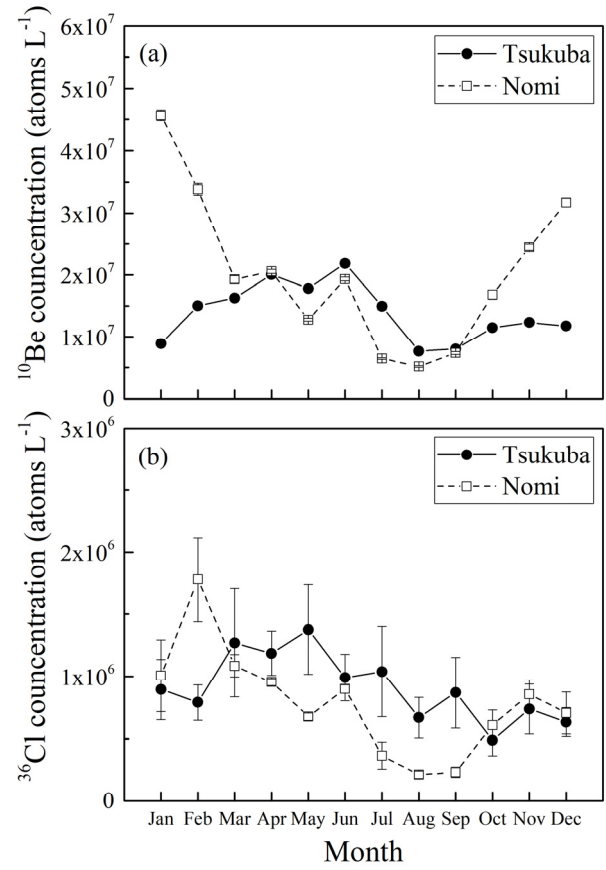


Fig. 2. Seasonal variations of ^{10}Be and ^{36}Cl concentration at Tsukuba and Nomi.

3.4 The Performance of Iodine-129 AMS measurements at the University of Tsukuba in FY 2019

M. Matsumura, K. Sasa, T. Takahashi, Y. Ochiai, T. Matsunaka¹, H. Yokoyama, Y. GAO, M. Hashimoto, A. Sakaguchi, K. Sueki

This report focuses on the performance of ^{129}I measurement by accelerator mass spectrometry (AMS) for the development of the standard reference materials (STD) of ^{129}I in the near future. Details of the ^{129}I AMS measurements were shown in the references [1-3].

From April 2019 to March 2020, we measured 257 samples of ^{129}I , the details of which are shown in Fig. 1. The test samples were chosen from environmental materials such as sea, rain, and river water, as well as soil and coral. Figure 2 shows the measured values of carrier-reagent blanks. The machine background is estimated to be on the order of 10^{-15} in the $^{129}\text{I}/^{127}\text{I}$ ratio, which is sufficiently lower than the background level of the ratio of 2×10^{-14} for "Old Iodine" provided from DeepWater. However, sometimes, the measured $^{129}\text{I}/^{127}\text{I}$ values in blanks ranged over ten times higher than 2×10^{-14} . One of the causes for this might be the memory effect [3,4]. The rise in blank values in 2018 and 2019 is most likely to be caused by this memory effect.

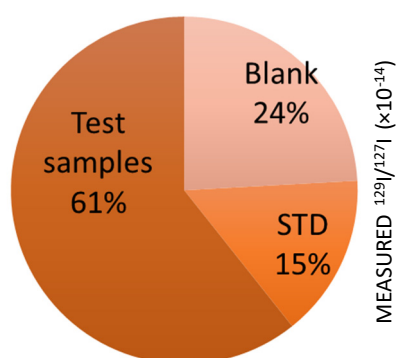


Fig. 1. Details of measured ^{129}I by the AMS system in fiscal 2019.

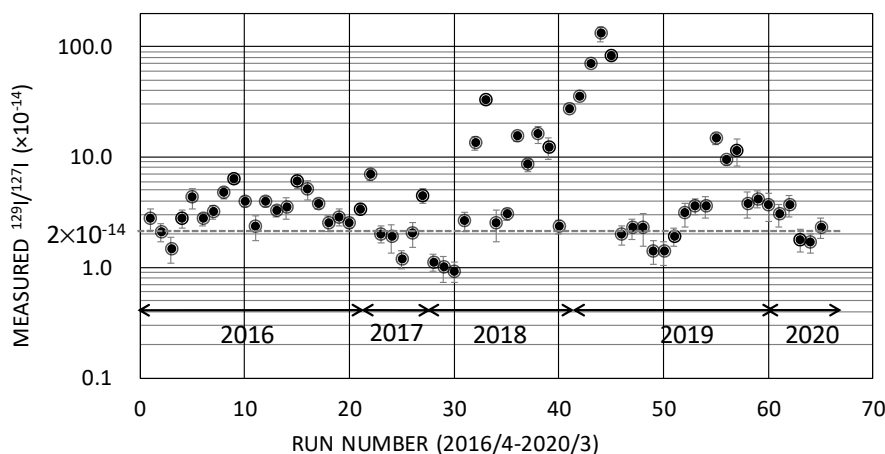


Fig. 2. $^{129}\text{I}/^{127}\text{I}$ ratios in blanks.

Figure 3 shows the results of measurement for JAEA 1-1, 2-1, 3-1 STD samples [5] provided by Japan Atomic Energy Agency (JAEA). They were normalized by using Purdue-2 STD (Z94-0596) with an $^{129}\text{I}/^{127}\text{I}$ ratio of 6.54×10^{-11} in the measurement [6] (the value was revised in 2014 [7]), which was provided by the Purdue Rare Isotope Measurement Laboratory (PRIME Lab) at Purdue University, USA. The nominal $^{129}\text{I}/^{127}\text{I}$ ratios are 3.948×10^{-11} , 2.406×10^{-11} , and 5.05×10^{-12} for JAEA 1-1, JAEA 2-1, and JAEA 3-1, respectively. However, the normalized ratios are greater than the nominal values by factors of, on the average, 1.38, 1.39, and 1.40 for JAEA 1-1, 2-1, and 3-1, respectively. These results are similar to those obtained at the Micro Analysis Laboratory, Tandem Accelerator, the University of Tokyo (MALT), Tokyo, Japan [5].

¹ Kanazawa University

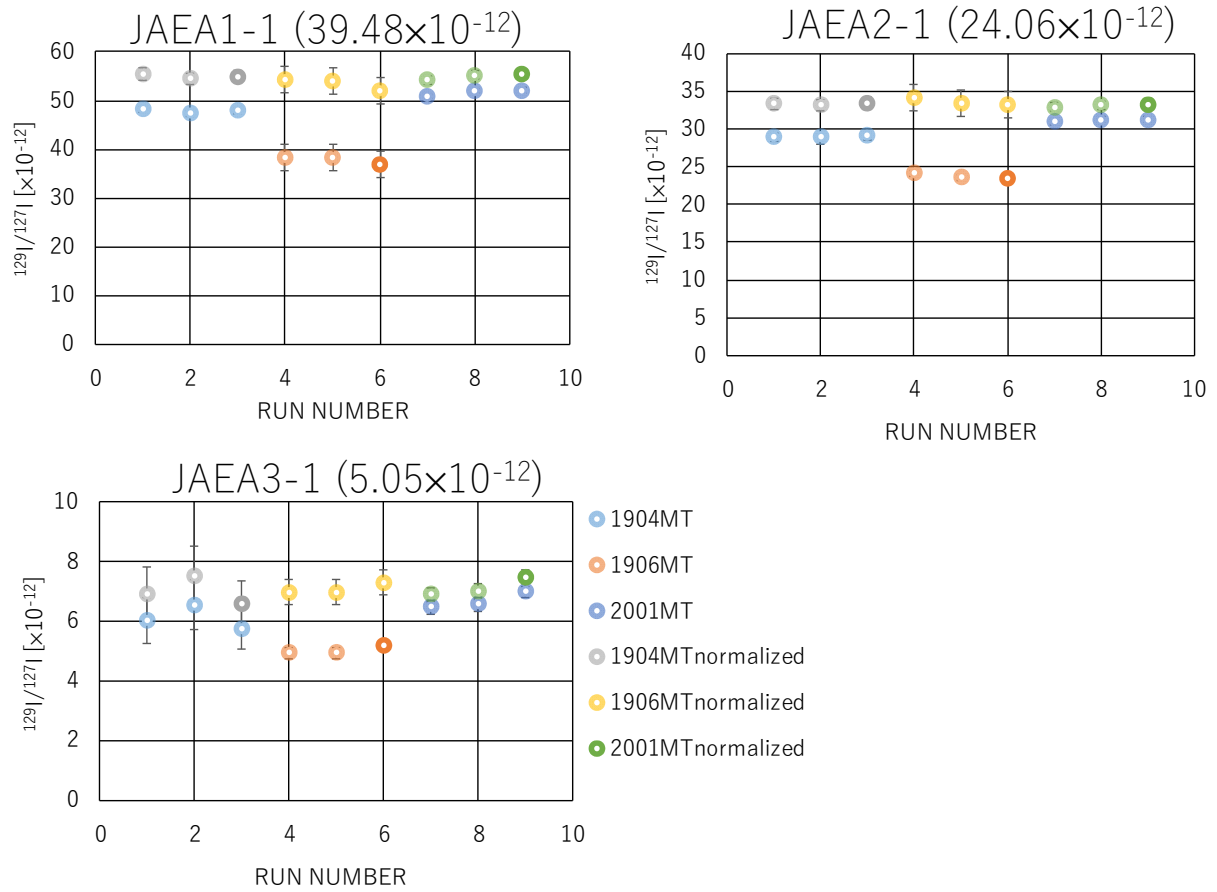


Fig. 3. Measured $^{129}\text{I}/^{127}\text{I}$ ratios for the JAEA-STD samples. The measurement time for each run was 2min.

This work was supported by JSPS KAKENHI Grant Numbers 15H02340 and 19H04252.

References

- [1] K. Sasa et al., Nucl. Instrum. Meth. Phys. Res. B 437 (2018) 98.
- [2] M. Matsumura et al., UTTAC Annual Report 2016 (2017) 25.
- [3] M. Matsumura et al., UTTAC Annual Report 2018 (2019) 27.
- [4] S. Xu et al., Nucl. Instrum. Meth. Phys. Res. B 438 (2019) 96.
- [5] T. Suzuki, (JAEA), Private communication.
- [6] P. Sharma et al., Nucl. Instrum. Meth. Phys. Res. B 123 (1997) 347.
- [7] M. Caffee, (Purdue University), Private communication (2014).

3.5 Anthropogenic iodine-129 depositions at the Japan Sea and Pacific sides of the archipelago, during 2017-2018

T. Matsunaka¹, S. Nagao¹, S. Ochiai¹, T. Takahashi, M. Matsumura, K. Sueki, K. Sasa

The investigation of water dynamics change in the Japan Sea caused by the recent global warming is essential for forecasting the response of ocean circulation with climate change. Anthropogenic ^{129}I ($T_{1/2} = 15.7$ million years) produced from the thermal neutron fission, is dominated by release from nuclear fuel reprocessing plants in the Europe and supplied at the Japan Sea via atmospheric deposition and surface runoff. The long-lived ^{129}I is expected as an oceanic tracer of surface and vertical circulations in the Japan Sea. This study aimed to illuminate the atmospheric deposition flux of ^{129}I in the Japan Sea through the monthly monitoring of ^{129}I in precipitation at Nomi located in middle area of the Japan Sea side of the archipelago during 2017–2018, by contrasting with the ^{129}I depositions in Tsukuba (Pacific side) about 300 km ESE of Nomi and Hirosaki (Japan Sea side) [1] about 600 km NE of Nomi.

Rain water samples were collected at each station in Nomi and Tsukuba cities using a funnel placed on the buildings of Low Level Radioactivity Laboratory (Kanazawa University) and Tandem Accelerator Complex (University of Tsukuba) on a monthly basis from July 2017 to December 2018. After adding 1 mg of iodine carrier (Woodward old iodine) with an $^{129}\text{I}/^{127}\text{I}$ ratio of 1.5×10^{-14} to the filtered 200–500 ml rainwater sample, the iodine was isolated by solvent extraction with CCl_4 . The purified iodide was precipitated as AgI by adding AgNO_3 . The AgI precipitate was then washed with NH_4OH and ultra-pure water, and was dried and loaded into an Al holder with Nb powder. The $^{129}\text{I}/^{127}\text{I}$ ratio of the AgI targets was measured using the accelerator mass spectrometry (AMS) system at the Tandem Accelerator Complex. A terminal voltage of 5 MV and a charge state of 5^+ were chosen for acceleration and detection. The measurement ratios were normalized against the Purdue-1 reference material, which had an $^{129}\text{I}/^{127}\text{I}$ ratio of 8.37×10^{-12} and was obtained from the Purdue University, USA. Stable iodine (^{127}I) in the rainwater was measured by an inductively coupled plasma–mass spectrometry (ICP–MS). The original $^{129}\text{I}/^{127}\text{I}$ ratios and ^{129}I concentrations in the rainwater were calculated using $^{129}\text{I}/^{127}\text{I}$ ratio from AMS and ^{127}I concentration from ICP-MS.

The overall dissolved ^{129}I concentrations in rainwater varied from 18.3 to 326 nBq L^{-1} (mean 129 nBq L^{-1}) at Nomi and from 32.7 to 223 nBq L^{-1} (mean 134 nBq L^{-1}) at Tsukuba. Mean monthly deposition fluxes of ^{129}I during 2017–2018 were in the range 0.144–1.73 $\mu\text{Bq m}^{-2} \text{ day}^{-1}$ at two sites (mean 0.834 $\mu\text{Bq m}^{-2} \text{ day}^{-1}$ at Nomi and 0.488 $\mu\text{Bq m}^{-2} \text{ day}^{-1}$ at Tsukuba, Fig. 1), about one-third to one-half of the mean values observed at Hirosaki (1.28 $\mu\text{Bq m}^{-2} \text{ day}^{-1}$) [1] located 600 km NE of Nomi and 500 km N of Tsukuba. Clear seasonal variations of ^{129}I depositions were found at the Japan Sea side (Nomi and Hirosaki), with the higher levels being recorded in winter (November to February). These latitude and seasonal dependences revealed that the deposited ^{129}I at the Japan Sea was mainly transported by the prevailing northwesterly winter monsoon from higher latitude area of the North Hemisphere.

¹ Kanazawa University

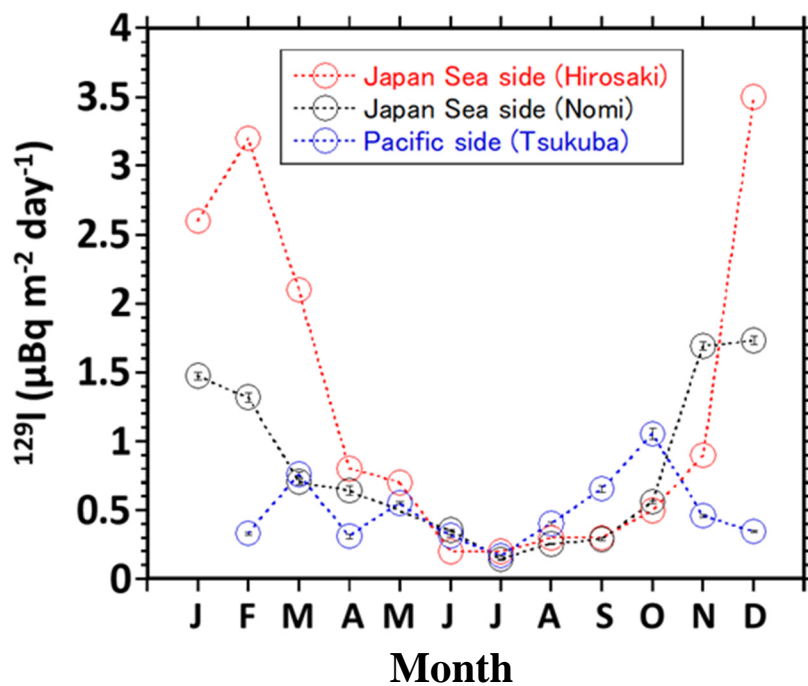


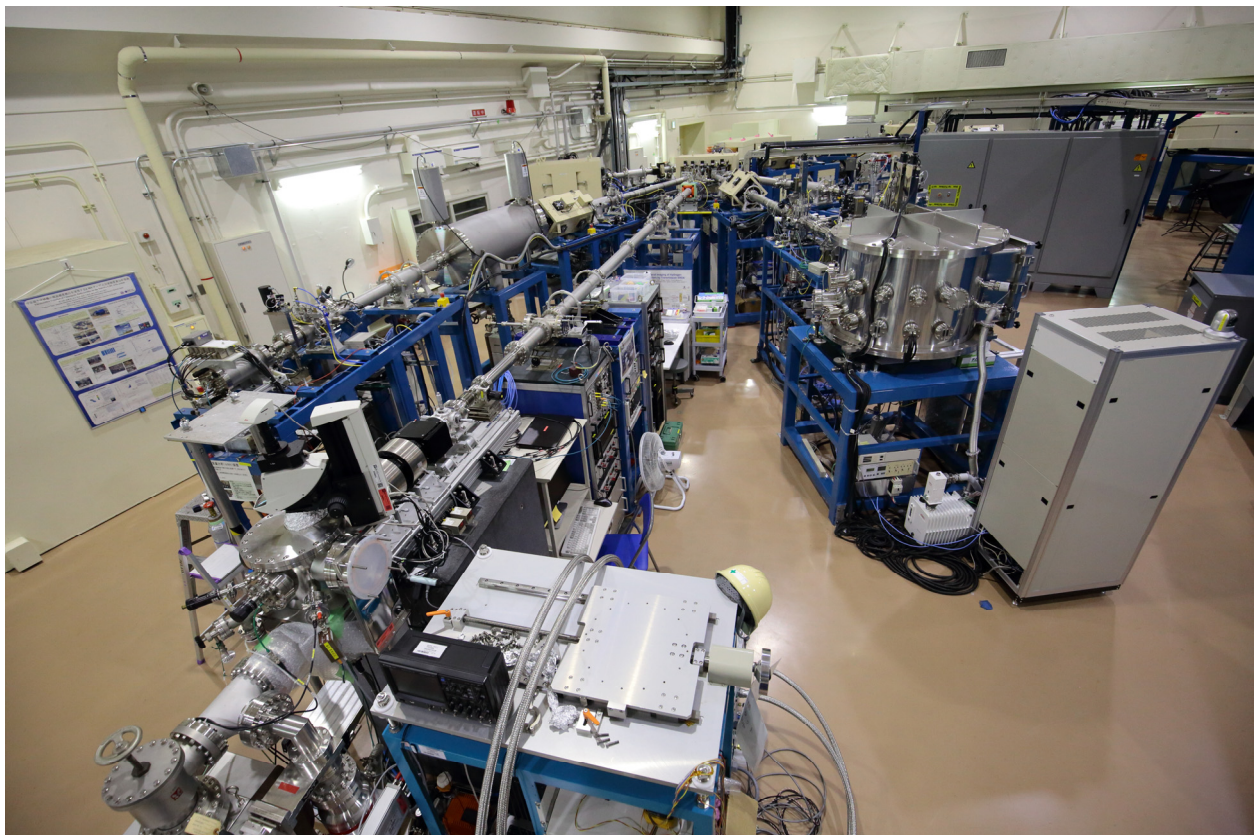
Fig. 1. Mean monthly depositions of ^{129}I at the Japan Sea side (Nomi) and Pacific side (Tsukuba) during 2017-2018 contrasting with the ^{129}I deposition at Hirosaki during 2012-2015 [1].

Reference

[1] Hasegawa et al., Journal of Environmental Radioactivity 171 (2017) 65.

4.

BEAM AND ISOTOPE APPLICATIONS



Micro-beam line for materials analysis (front left)

4.1 Vacancy-type defects in Mg implanted GaN studied by positron annihilation spectroscopy

A. Uedono, M. Dickmann¹, W. Egger¹, C. Hugenschmidt², S. Ishibashi³, S. F. Chichibu⁴

GaN has been studied extensively as next generation power semiconductors [1]. In device structure fabrication, controlled impurity doping in a selective area is essential. Ion implantation is the most commonly used technique to control carrier concentrations. A drawback of ion implantation is the introduction of defects. Because the mechanisms that cause damage during GaN ion implantation and the damage recovery processes are complicated [2], controlling damage during and after ion implantation is a key for the reduction of residual defects in GaN. In the present study, we report the annealing properties of vacancies in Mg-implanted GaN using monoenergetic positron beams [3].

Mg⁺ ions were implanted into GaN(0001) with energies of 20 to 430 keV to obtain 0.5- μ m-deep box profiles with Mg concentrations [Mg] of 1×10^{17} , 1×10^{18} , and 1×10^{19} cm⁻³. All samples were annealed at temperatures between 1000°C and 1300°C (5 min) in flowing N₂ gas at atmospheric pressure. Figure 1 shows the *S* values of Mg-implanted GaN with a Mg concentration of 1×10^{17} , 1×10^{18} , and 1×10^{19} cm⁻³ after annealing at 1300°C as a function of the incident positron energy *E*. The results for the as-implanted sample with [Mg] = 1×10^{17} cm⁻³ are also shown. The *S* value corresponding to positron annihilation in HVPE-GaN was reported to be 0.441, and this value corresponds to positron annihilation in defect-free GaN. For the as-implanted sample, the measured *S* values were larger than this value, suggesting positron trapping by vacancy-type defects introduced by ion implantation. The solid curves in Fig. 1 are fits to the experimental data.

Figure 2 shows the derived depth distributions of *S* from the analysis. For the as-implanted sample, the damaged region was introduced up to a depth 1000 nm, and this region was deeper than the block profile of Mg (0–500 nm). This discrepancy was due to defect introduction by Mg implanted below 500 nm and the high sensitivity of positrons to vacancy-type defects. After annealing at 1300°C, although the *S* value below 400 nm decreased, the value at 50–500 nm increased, suggesting the agglomeration of vacancy-type defects in the region with high [Mg].

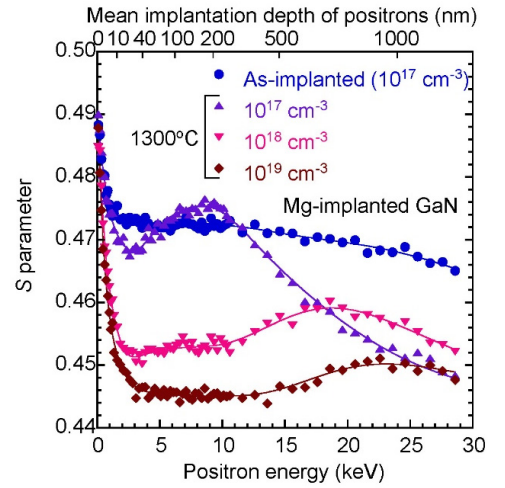


Fig. 1. *S* parameters as a function of the incident positron energy *E* for Mg-implanted GaN annealed at 1300°C with [Mg] = 1×10^{17} , 1×10^{18} , and 1×10^{19} cm⁻³.

¹Universität der Bundeswehr München

²Technische Universität München

³National Institute of Advanced Industrial Science and Technology (AIST)

⁴Tohoku University

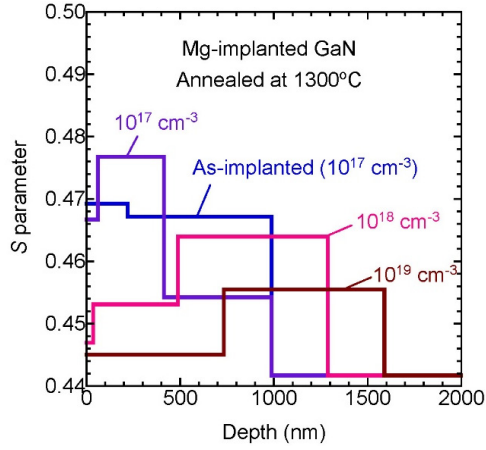


Fig. 2. Depth distributions of S for Mg-implanted GaN annealed at 1300°C with $[Mg]=1\times 10^{17}$, 1×10^{18} , and 1×10^{19} cm $^{-3}$. The result for the as-implanted sample ($[Mg]=1\times 10^{17}$ cm $^{-3}$) was also shown.

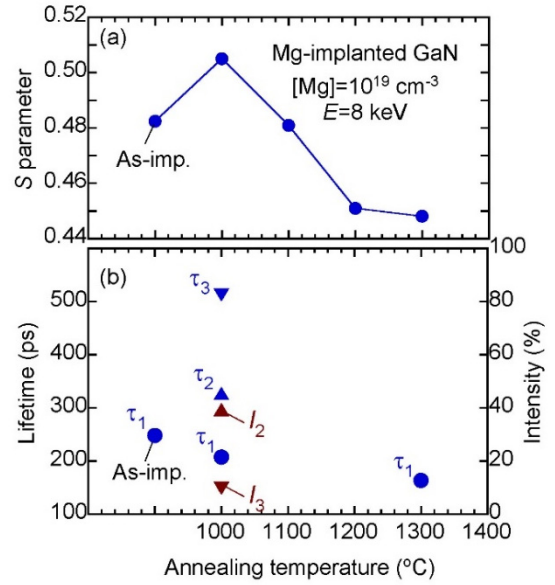


Fig. 3. Annealing behaviors of S , lifetimes (τ_i), and corresponding relative intensities (I_i) for Mg-implanted GaN with $[Mg]=1\times 10^{19}$ cm $^{-3}$.

For the samples with $[Mg]=1\times 10^{19}$ cm $^{-3}$, the lifetime spectra of positrons were measured, and the obtained spectra were decomposed into one or three components. Figure 3 shows the annealing behaviors of S , τ_i and I_i measured at $E = 8$ keV, where τ_i and I_i show i -th positron lifetime and corresponding intensity. The lifetime spectra for the as-implanted sample and the one annealed at 1300°C were analyzed assuming a one-annihilation mode. The observed increase in S after annealing at 1000°C was due to the formation of vacancy clusters. The decrease in the S value started above 1100°C, which was due to the activation of Mg, and the resultant change in the charge state of vacancy-type defects. For the as-implanted sample, the lifetime of positrons was obtained as 248 ± 1 ps. Using the computer simulation, the positron lifetimes for Ga-vacancy (V_{Ga}), divacancy ($V_{Ga}V_N$), $(V_{Ga}V_N)_2$, $(V_{Ga}V_N)_3$ were obtained to be 239, 246, 296, and 330 ps, respectively. Thus, for the as-implanted samples, the major defect species was identified as Ga-vacancy (V_{Ga}) related defects such as $V_{Ga}V_N$ and/or their complexes with impurities. For the sample annealed at 1000°C, the second annihilation mode can be attributed to the trapping of positrons by vacancy clusters such as $(V_{Ga}V_N)_3$. The third lifetime was obtained at 510 ± 60 ps. A similarly long positron lifetime was observed for plastically deformed GaN [4], attributing to positron trapping by large vacancy clusters or microvoids.

The present research showed that the positron annihilation technique is suited to study the vacancies in GaN. Knowledge on the annealing behaviors of vacancy-type defects is useful for optimizing the process of fabricating p-type GaN by using ion implantation.

References

- [1] H. Amano et al., J. Phys. D: Appl. Phys. 51 (2018) 163001.
- [2] S. O. Kucheyev et al., Mat. Sci. Eng. R-Rep. 33 (2001) 51.
- [3] A. Uedono et al., Phys. Stat. Sol. B 256 (2019) 1900104.
- [4] A. Uedono et al., J. Appl. Phys. 114 (2013) 084506.

4.2 Microscopic 3-dimensional mapping of hydrogen bubbles in Al by elastic recoil detection analysis under transmission geometry

A. Yamazaki, K. Sasa, S. Tomita, S. Ishii, H. Naramoto, M. Sataka, H. Kudo, G. Itoh¹, M. Ohkubo²

Hydrogen in Al typically becomes gas bubbles which may cause brittleness of Al-based structural materials since the gas bubble behaves effectively like lattice defects or solid solutions. To understand mechanical influence caused by hydrogen in Al and Al alloys, it is crucial to establish a method for observing 3-dimensional distributions of hydrogen in materials.

In response to such technical requirement, we have demonstrated to measure microscopic 3-dimensional distribution of plasma-charged hydrogen in polycrystalline Al. The measurements have been carried out nondestructively by using elastic recoil detection analysis under transmission geometry (T-ERDA) of a collimated 8 MeV $^4\text{He}^{2+}$ beam. The recoil cross section as large as 2×10^3 mb/sr due to the nuclear elastic collision allowed observation of the spatial distribution of hydrogen in the Al sample of 80 μm thickness.

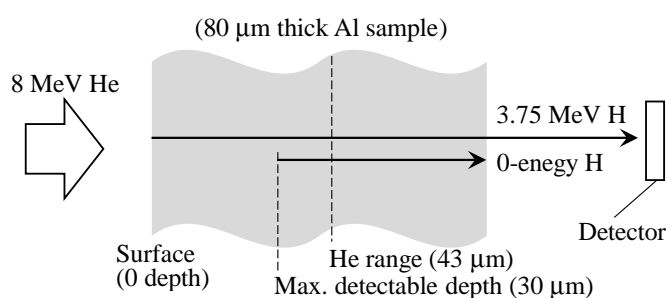


Fig. 1. Schematic diagram of the present T-ERDA. Deeper H recoil results in lower exit energy.

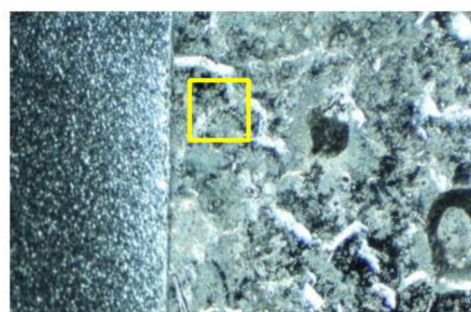


Fig. 2. Optical photograph of the surface of the Al sample placed on the right. The Al-coated mylar film placed on the left is for reference of a hydrogen-containing sample. The square marked in yellow shows the $250 \times 250 \mu\text{m}^2$ area analyzed by T-ERDA.

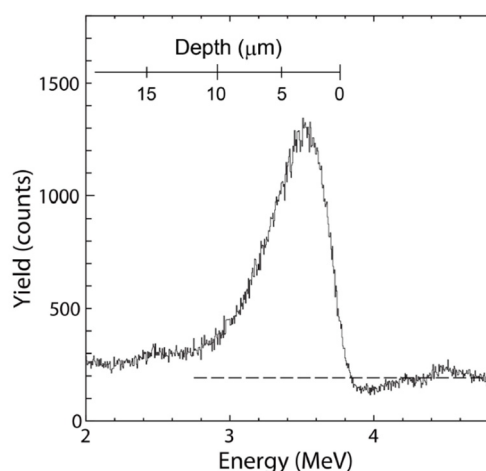


Fig. 3. T-ERDA energy spectrum measured for the $250 \times 250 \mu\text{m}^2$ area on the Al sample. The scale of depth where the H recoil occurred is indicated. The dashed line shows the assumed background of 192 counts.

¹ Ibaraki University

² AIST

The distribution maps of hydrogen (Fig. 4) clearly visualize 3D hydrogen bubbles of 10-20 μm diameter in the surface layer of about 12 μm thickness. The critical concentration of hydrogen minimally needed for growth of the hydrogen bubble of ten- μm size has been determined to be $1.6 \times 10^{20} \text{ cm}^{-3}$. T-ERDA combined with nuclear elastic scattering thus provides 3D data from which we obtain direct information about microscopic behavior of hydrogen in materials.

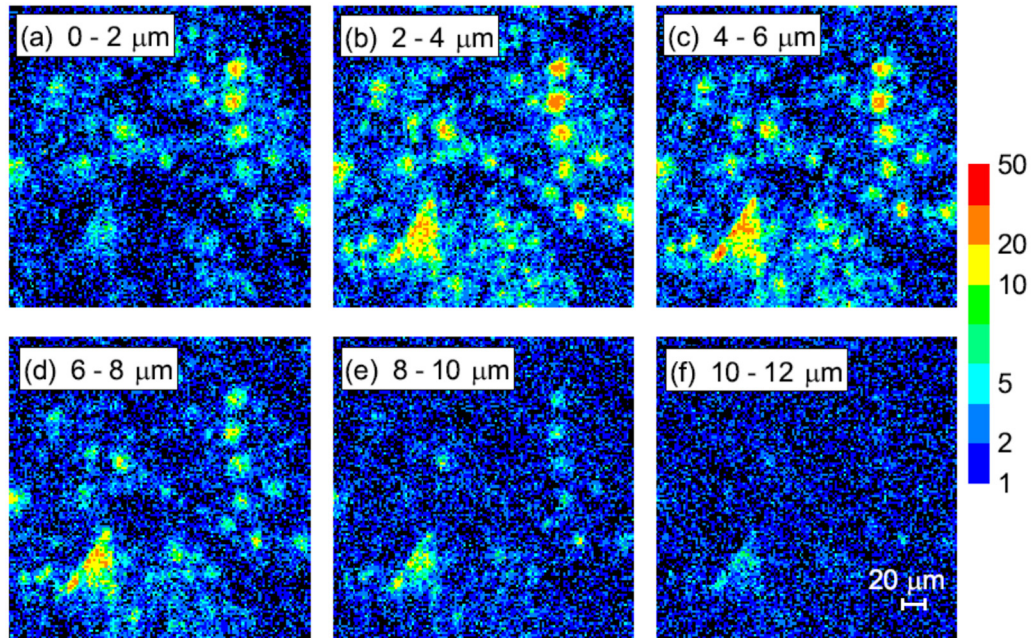


Fig. 4. 3-dimensional mapping of plasma-charged hydrogen in the Al sample of 80 μm thickness, shown for the 6 slices, (a)–(f), of 12 μm depth. The scanned area is $250 \times 250 \mu\text{m}^2$ which is marked in yellow in Fig. 2. The lateral resolution is 3.5 μm and the depth resolution is $\sim 1.2 \mu\text{m}$, see text. Note that the color scale is logarithmic and the pixels of zero count are shown in black. The average He^{2+} beam current was 80 pA and the measurement time was about 1 hour.

Notably, a triangle-like distribution of hydrogen is seen near the left-bottom corners of the 6 images in Fig. 4. Since the Al foil is polycrystalline, such an anisotropic distribution in a ten- μm space is not expected to arise from local lattice disorder in Al, which is in contrast to the lattice-dependent precipitation of implanted atoms in a single crystal [2]. A possible origin might be the growth of tetrahedral AlH_3 [3].

References

- [1] A. Yamazaki et al., AIP Advances 9 (2019) 105111.
- [2] For example, M. Ohkubo and N. Suzuki, Philos. Mag. Lett. 57 (1988) 261.
- [3] G. Itoh, et al., Keikinzoku (Light metals) 40 (1990) 36 (in Japanese).

4.3 Depth resolution of hydrogen distribution in Al measured with elastic recoil detection analysis under transmission geometry

A. Yamazaki, K. Sasa, S. Tomita, S. Ishii, H. Naramoto, M. Sataka, H. Kudo

In a previous study, we have measured 3D hydrogen distribution in an H-charged Al foil of 80 μm thickness applying elastic recoil detection analysis under transmission geometry (T-ERDA) using 8-MeV He^{2+} [1]. In this case, the depth resolution for hydrogen at the Al surface was $\sim 1.2 \mu\text{m}$ which was estimated from the width of the spectrum peak of hydrogen localized near the Al surface. In this case, the depth resolution results from the energy straggling of recoil H in the outgoing path through the Al foil. However, the depth resolution at a given depth should result from straggling of both incident He and recoil H. For wide application of T-ERDA in future, we need to investigate how the depth resolution varies in the depth range of interest.

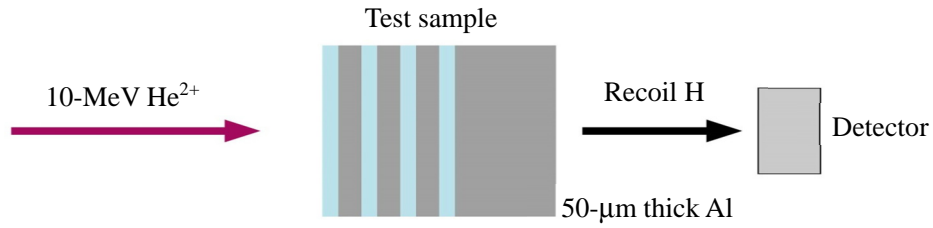


Fig. 1. Schematic diagram of the test sample consisting of a layered structure of four sheets of 1.2 μm thick PPS (blue) and three sheets of 10 μm thick Al (gray), which are mounted on Al of 50 μm thickness.

For this purpose, we have prepared a multilayered sample of 1.2- μm thick polyphenylene sulfide (PPS) and 10- μm thick Al, which were mounted on an Al foil of 50 μm thickness, as shown in Fig. 1. In the experiments, 10 MeV He^{2+} was incident on the sample and the recoil H from PPS was energy-analyzed with a semiconductor particle detector.

Figure 2 shows the measured energy spectrum of H after passing through the sample. The four peaks correspond to the depths of the PPS layers, as indicated near the peaks. The peak widths result from energy straggling of incident He and recoil H. On the other hand, the peak areas result not only from energy straggling which might deflect the recoil H away without entering the detector, but also from energy dependence of the recoil cross section for H. None of these peaks have a flat top, which indicates only minor energy losses in the thin PPS layers. Therefore, the energy difference between the

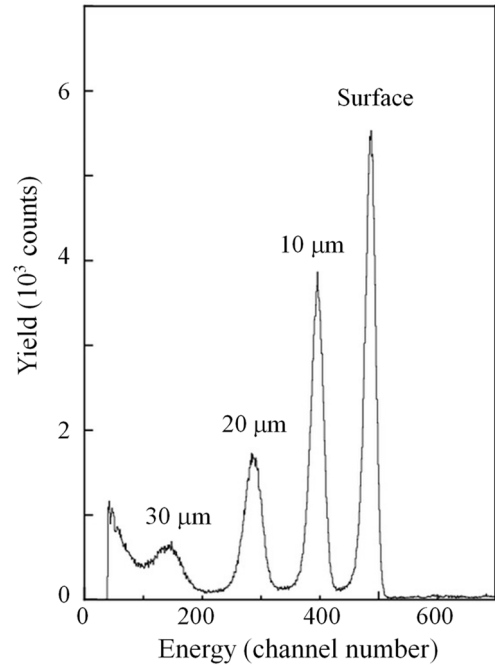


Fig. 2. Hydrogen energy spectrum of measured by T-ERDA. The peaks correspond to the depths of the four PPS layers.

adjacent peaks ΔE is mainly due to the Al thickness of 10 μm . It should be noted that ΔE increases slightly with increasing the depth, corresponding to larger stopping power of Al for lower-energy H in the present case. The depth resolution ΔD at a given depth can be estimated from the FWHM value of the spectrum peak. Hence, we obtain ΔD at depths of 0 (surface), 10, 20 and 30 μm .

The results are shown in Fig. 3. The value of ΔD increases rapidly with increasing the depth beyond 20 μm . It is pointed out that comparison of the peak areas provide effective counting efficiency of recoil H at a given depth. In the present case, for example, the counting efficiency at 10 μm depth is less than at the surface by $\sim 10\%$. Further measurements concerning not only the depth resolution, but also the lateral resolution are now under way for precise analysis of T-ERDA data, in particular, 3D images of hydrogen distribution.

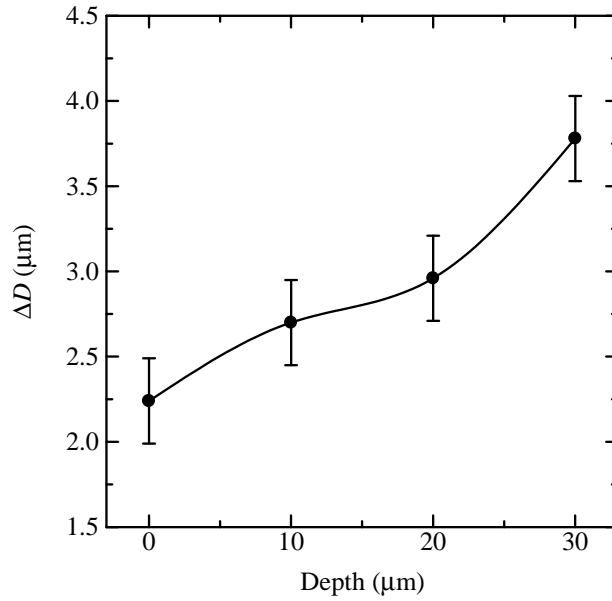


Fig. 3. ΔD vs. depth, determined from the H spectrum shown in Fig. 2. The spline curve was drawn to guide the eye.

Reference

- [1] A. Yamazaki et al., AIP Advances 9 (2019) 105111.

4.4 Trial of ^7Li depth profile determination by $^7\text{Li}(p, \alpha)^4\text{He}$ NRA

D. Sekiba, Y. Sugisawa, N. Kishi

Development of all-solid lithium ion battery has been required from the viewpoint of large and safe electric storage. The most serious problem of all-solid lithium ion battery, that we must overcome, is the current restraint during the discharge. It is widely believed that there is a non-desirable block layer between the solid-state electrolyte and the anode. At present, we usually use Li_3PO_4 and LiCoO_2 for the electrolyte and the anode, respectively. The scenario, that there could be a block layer against the Li ion migration, remains a matter of speculation among the engineers in this field. In order to examine the scenario, we are intending to measure the Li depth profile non-destructively during the device operations. For the first step, we made $^7\text{Li}(p, \alpha)^4\text{He}$ NRA measurements [1] to estimate the depth resolution of this technique, which depends considerably on the experimental setup.

Figure 1 shows a schematic of the sample prepared for the present study. The three Li_3PO_4 layers of 100 nm thickness are separated by the two Au layers of 100 nm thickness, and they are deposited on the substrate of ordinary quartz. The topmost 100 nm thick Au layer is a cap to suppress the oxidation. The NRA measurements were carried out using the conventional RBS/ERDA chamber at D-course of 1 MV Tandetron in UTTAC [2]. H^- ions extracted from the sputtering ion source were charge-exchanged and accelerated up to 1.5 MeV, and used as a probe beam after shaped as $1 \times 1 \text{ mm}^2$ by a double slit system. The emitted α particles ($\sim 7.8 \text{ MeV}$) were detected by a Si surface barrier detector placed at $\theta' = 150^\circ$ with respect to the beam direction, as schematically shown in Fig. 2. The angle θ between the detection direction and the surface normal is an experimental parameter mainly to change the length of the outgoing path of the emitted α .

Figure 3 shows the NRA spectra obtained at (a) $\theta = 75^\circ$ and (b) 80° . In both spectra, we clearly see three peaks corresponding to the $^7\text{Li}(p, \alpha)^4\text{He}$ reaction in the three Li_3PO_4 layers as annotated in Fig. 1. First of all, we concluded

that with this technique 100 nm or better depth resolution is achieved. This conclusion was also supported by using a similar sample of 50 nm layer thickness, instead of 100 nm layer thickness. At $\theta = 80^\circ$, we notice that the peak width of the third layer is considerably deformed probably due to the energy struggling of the emitted α particles, nevertheless the sufficient separation between the two peaks corresponding to the first and the second layers might provide local but valuable information. These results seem helpful to choose the NRA depth resolution needed to investigate the depth range of interest in the sample.

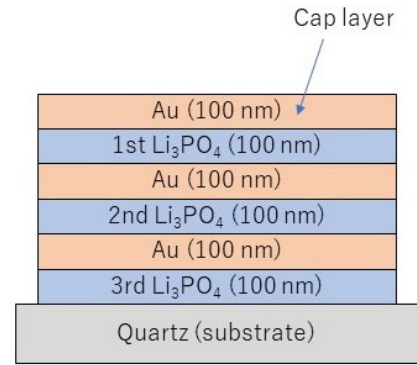


Fig. 1. Schematic of the sample structure.

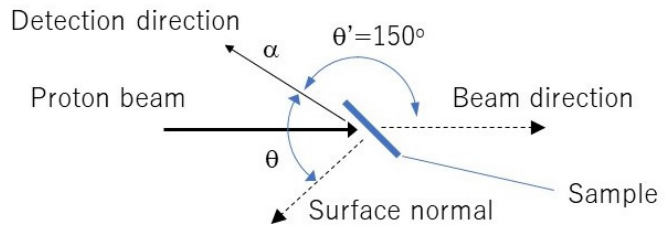


Fig. 2. Schematic of the experimental setup.

Apart from the intense three peaks due to the first, second and third Li_3PO_4 layers, we see weak α signals in the energy range of 2400 ~ 2600 channels in Fig. 3 (a) and (b). While the origin of these signals is so far not clear, we guess that Li migrates into the Au cap layer. In the next experiment, we are intending to use Ni instead of Au because Li does not make any alloy with Ni.

As conclusion, we confirmed that non-destructive NRA is useful to investigate the real devices currently developed in many facilities all over the world because the all-solid Li ion batteries usually have ~100 nm thickness for the anode and cathode and several mm thickness for electrolyte. The Li profile measurements during the device operation are also promising with this method.

We thank Prof. T. Hitosugi, Dr. R. Shimizu and Mr. S. Kobayashi of Tokyo Institute of Technology for their sample preparations and critical discussions.

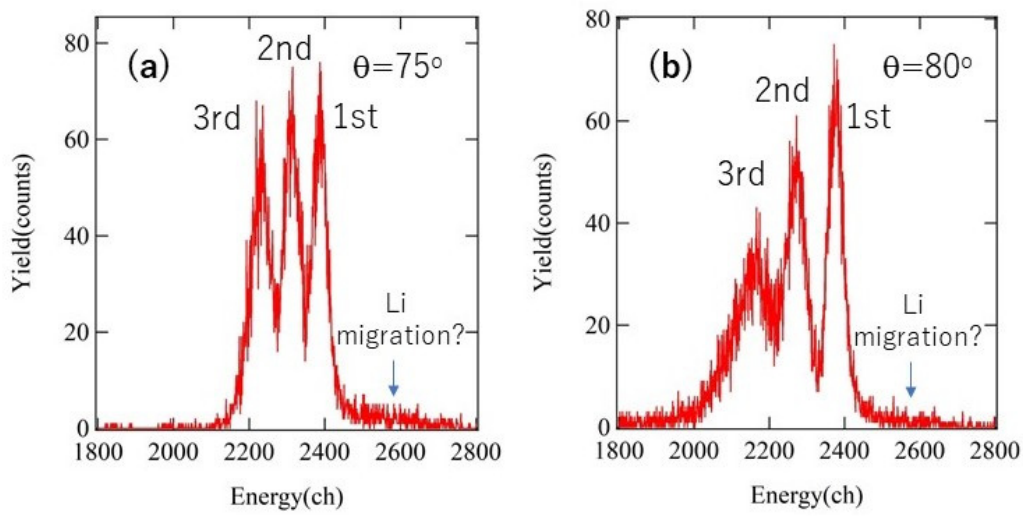


Fig. 3. NRA spectra taken on the multi-layered sample with the setup of (a) $\theta=75^\circ$ and (b) 80° .

References

- [1] J. Räisänen, Nucl. Instr. Meth. Phys. Res. B 66 (1992) 107.
- [2] D. Sekiba, et al., Diamond & Related Materials 27-28 (2012) 60.

4.5 Depth profiling of lithium by use of TOF-E telescope ERDA

Y. Sugisawa, D. Sekiba, I. Harayama

Li-ion batteries are widely applied to various portable devices and have distinct potential as power sources. However, the risk of combustibility of organic solvent has limited its application. All-solid-state Li-ion batteries have been developed to remove this limit by using non-combustible electrolyte [1]. Apart from the safety, all-solid-state Li-ion battery would enable us to obtain the capacity increase or micro-fabrication. For the realization of such a battery, the poor Li conductivity at the electrode-electrolyte interface should be improved [2]. Hence, it is important to understand the dynamic transport of Li at the electrode-electrolyte interface of Li-ion batteries. Time of flight-energy telescope elastic recoil detection analysis (TOF-E telescope ERDA) is an effective technique for quantitative depth profiling of light elements in thin films [3, 4]. This technique can be also applied to the analysis of the electrode-electrolyte interface of Li-ion batteries. In our present work, we observed Li in a $\text{Li}(\text{CoNi})\text{O}_2$ film deposited on Al_2O_3 , which is typically used as a positive electrode, as the first step for observation of the electrode-electrolyte interface.

The TOF-E telescope ERDA measurement was performed at 1 MV Tandetron in UTTAC. Figure 1 shows the experimental setup of the scattering chamber and TOF tube. The system consists of two time-detectors (T1 and T2) each equipped with a micro-channel plate (MCP) and a particle detector (SSD) of 300 mm^2 sensitive area. T1 and T2 generate the start and stop triggers in the TOF measurement, respectively, while SSD determines the kinematic energy of the recoils. T1 is placed at 376 mm from the sample and the distance between the two time-detectors is 640 mm. The SSD is placed at 1093 mm from the sample. We can adjust the solid angle of the measurement system by the aperture at T1. The aperture with the diameter of 2.5 mm is usually set to limit the solid angle to be smaller than that defined by the sensitive area of SSD. In the present study, the typical incident beam was 4 MeV $^{35}\text{Cl}^{4+}$ and the beam size was shaped as $1 \times 1 \text{ mm}^2$ with a slit system. The beam incident angle on the sample was usually 75° from the surface normal. The recoil and backscattering angles are 30° and 150° from the beam incidence direction, respectively.

Figure 2 shows the two-dimensional histograms of the TOF-E telescope ERDA taken for the $\text{Li}(\text{CoNi})\text{O}_2$ film deposited on the Al_2O_3 substrate. The assignment of each element is notated in Fig. 2. ^7Li , O, and Al are clearly seen, while Co and Ni are not distinguished. In addition, we can see slight signals under the ^7Li curve, which are assigned to the recoils of ^6Li . The mass resolution Δm is expressed by

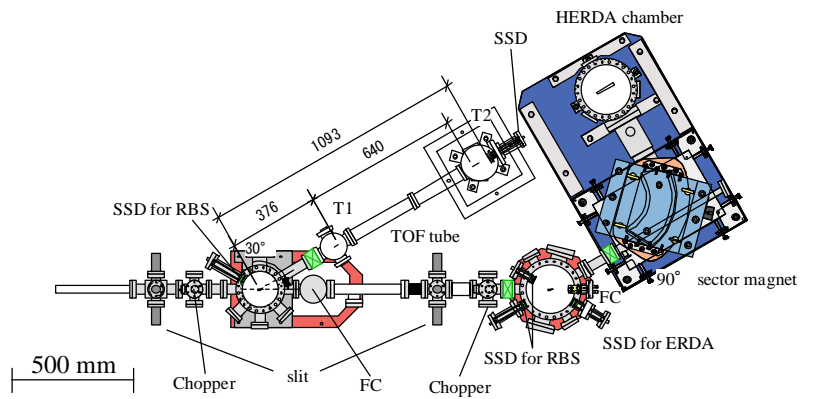


Fig. 1. Experimental setup of our scattering chamber and TOF tube at 1 MV Tandetron in UTTAC.

$$\Delta m = m \sqrt{\left(\frac{\Delta E}{E}\right)^2 + \left(\frac{2\Delta t}{t}\right)^2},$$

where m , E , t , ΔE , and Δt are the atomic mass, recoil energy, energy resolution, and time resolution of recoils, respectively. The mass resolution for ^7Li is calculated as 0.6 u, suggesting that our measurement system can separate ^7Li and ^6Li .

We obtained the depth profiles of each element in the film as shown in Fig. 3 by converting the TOF to depth by using the stopping power. The relatively weak ^7Li yield is indicated on the expanded right scale. The $\text{Li}(\text{CoNi})\text{O}_2$ film was observed at ~ 30 nm in Fig. 3. The O/CoNi and Li/CoNi ratios in the film estimated from the depth profiles are 1.8 and 0.2, respectively. The former, approximately equal to 2, corresponds to the stoichiometric ratio. However, the latter ratio 0.2 largely deviates from the stoichiometric ratio of Li/CoNi=1. This might imply that signal loss in our TOF measurement system is significant for the detection of Li. In the future work, we investigate the cause of signal loss and improve the measurement system.

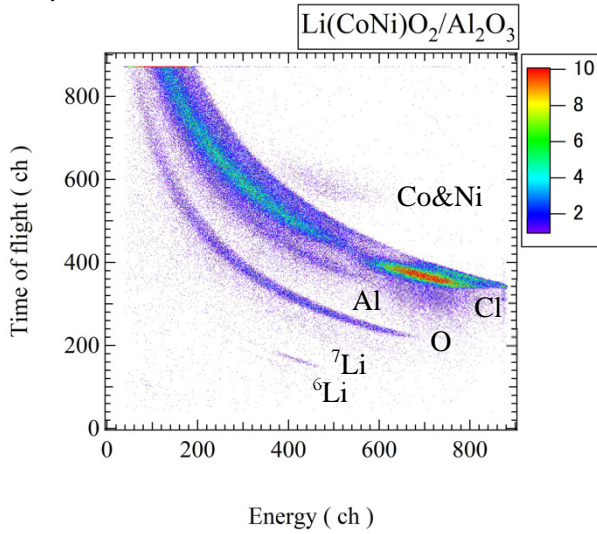


Fig. 2. Two-dimensional histograms of the TOF-E telescope ERDA taken on the $\text{Li}(\text{CoNi})\text{O}_2$ film deposited on the Al_2O_3 substrate.

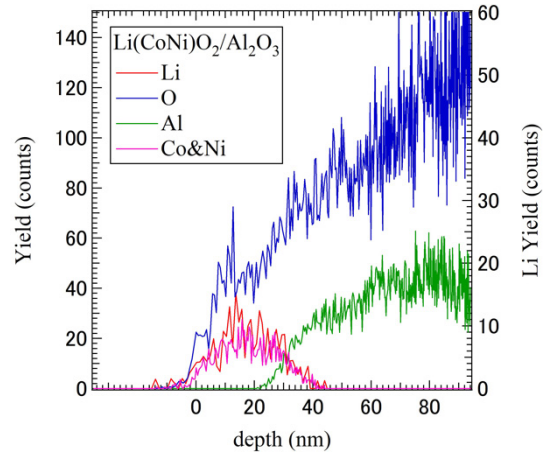


Fig. 3. Depth profile of each element in the $\text{Li}(\text{CoNi})\text{O}_2$ film deposited on the Al_2O_3 substrate.

References

- [1] Y. Sun et al., Chem. Mater. 29 (2017) 5858.
- [2] T. Minato and T. Abe, Progress in Surface Science 92 (2017) 240.
- [3] M. Chicoine et al., Nucl. Instr. Meth. Phys. Res. B 406 (2017) 112.
- [4] B. Brijs et al., Microelectron. Eng. 80 (2005) 106.

4.6 High magnetic field Mössbauer study on an antiferromagnetic layered FeNi nitride, FeNiN

S. Goto¹, H. Yanagihara, E. Kita²

Fe nitrides show various physical, electronic, and chemical properties where nitrogen atoms have played an important role on their electronic structures. For example, a larger magnetic moment than that of α -Fe has been reported on Fe_{16}N_2 . With increasing concentration of nitrogen, Fe nitrides change from Fe_4N , Fe_3N , to Fe_2N . Their structures are a cubic perovskite for Fe_4N and a hexagonal for Fe_{2-3}N , respectively. Basically in Fe nitrides, nitrogen atoms occupy at interstitial crystallographic sites and basic structure is not deformed much. It was reported that the increase of nitrogen concentration resulted in the decrease of ferromagnetic transition temperature (T_C) and T_C goes down to room temperature at around $\text{Fe}_{2.5}\text{N}$.

Fe_2N has an orthorhombic structure and by substituting Fe atoms by Ni atoms, a face centered tetragonal FeNiN is formed where Fe and Ni layers are interlaminated along the z-direction (see Fig. 1) [1]. As seen in Fig. 1, nitrogen atoms are only located on Fe layers at interstitial sites. This structure has been utilized to synthesize an L_{10} -FeNi alloy, a viable candidate of high magnetic anisotropy material, by removing nitrogen atoms from FeNiN [2]. For this purpose, the uniform high grade FeNi particles are required and basic properties of FeNiN as a starting material should be well understood [5]. We have performed Mössbauer study on FeNiN at low temperatures with/without an external magnetic field to understand the magnetism of FeNiN,

The FeNiN powder samples were synthesized by a gas phase nitridation of FeNi powders [2, 5]. A layer structure was confirmed with an X-ray diffraction study [5]. ^{57}Fe Mössbauer spectroscopy was performed at a transmission setup with a constant acceleration mode. A γ -ray source of ^{57}Co radio isotope with 1.85 GBq was used. An experimental setup was composed of a commercial linear motion driver (WissEL) and a conventional data acquisition system. An external magnetic field up to 5 T was applied parallel to the γ -ray direction by a superconducting magnet [3]. Measurement temperatures were room temperature, 77 K and 10 K. Data were analyzed with a commercial fitting software [4]. The powder sample with 10 mg was mixed with BN powder and the mixture was set into a sample holder made of a 1 mm thickness lead plate with a 10 mm diameter hole where the γ -ray passed through.

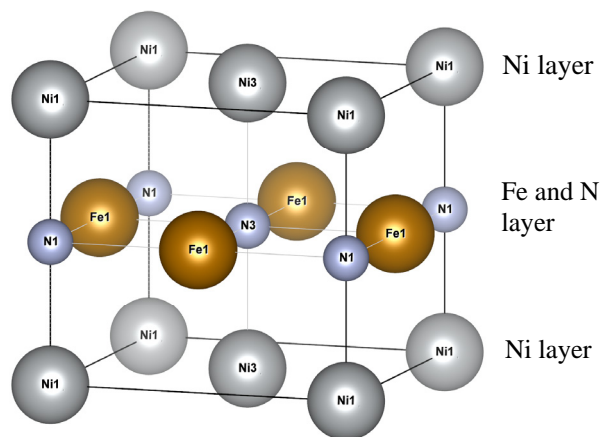


Fig. 1. Unit cell of FeNiN. Ni and Fe atoms form a face centered tetragonal structure (drawn with VESTA).

¹ DENSO Corporation

² NIT Ibaraki College

Figure 2 shows Mössbauer spectra for the FeNiN powder. The room temperature spectrum is composed of a set of a singlet and a doublet with small area, and there is no trace of magnetic sextets. This clearly shows that FeNiN is paramagnetic at room temperature. The area for the doublet is about 5 % and most Fe atoms are located at high symmetric positions proofing a high quality of sample. At low temperatures,

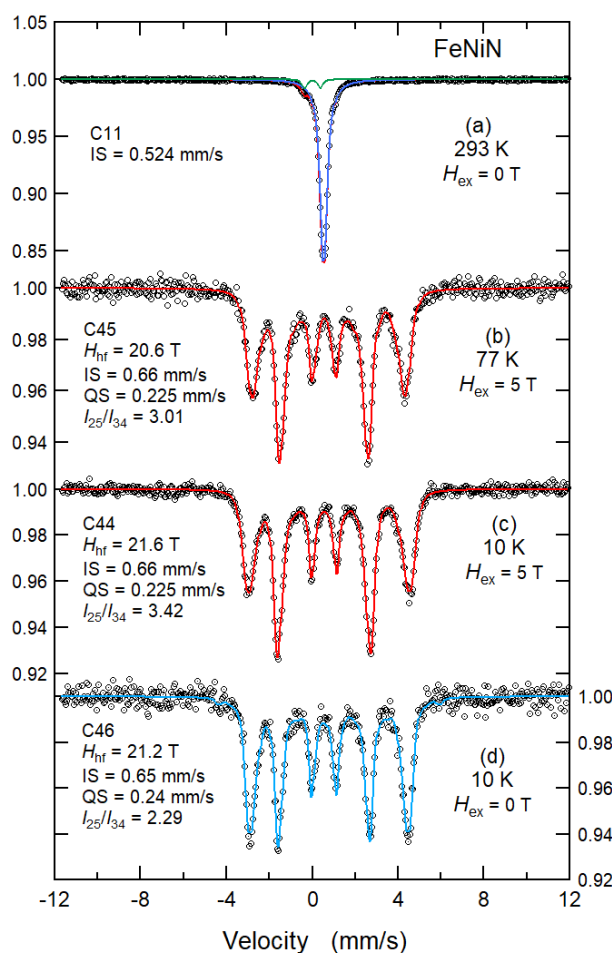


Fig. 2. Mössbauer spectra of FeNiN powder recorded (a) at room temperature, (b) at 77 K with $H_{\text{ex}} = 5$ T, (c) at 10 K with $H_{\text{ex}} = 5$ T and (d) at 10 K without H_{ex} . Experimental data and the results of fitting were depicted by open circles and solid lines, respectively.

magnetically split spectra were observed at 77 K and 10 K. It is simply concluded that the magnetic transition temperature of FeNiN is noticed between room temperature and 77 K. Actually, the transition temperature was determined at 178 K by a magnetic susceptibility measurement [5]. To understand the sort of magnetism at the specific temperature, ferromagnetism or antiferromagnetism, an in-field Mössbauer measurement is effective. The spectra recorded at 10 K with and without external magnetic fields are shown in Fig. 2 (c) and (d). An intensity ratio of 2nd and 5th peaks to 3rd and 4th peaks, I_{25}/I_{34} , for the zero-field spectrum was close to 2, the value for the case of randomly oriented magnetization, and the value for the in-field spectrum was not zero but 4. This result indicates that magnetic moments are aligned in the direction perpendicular to the magnetic field of 5 T. It supports that the sort of magnetism of FeNiN at low temperature is antiferromagnetism [5].

References

- [1] J. B. Goodenough et al., J. Appl. Phys. 31 (5) (1960) S342.
- [2] S. Goto et al. Scientific Reports 7 (2017) 13216.
- [3] SpectroMAG, Oxford Instruments, London.
- [4] MossWinn 4.0, Z. Klencsár, Hyperfine Interact. 217 (2013) 117.
- [5] S. Goto et al., ACS Appl. NANO Mater. 2(11) (2019) 6909, and its supporting information, https://pubs.acs.org/doi/suppl/10.1021/acsnm.9b01405/suppl_file/an9b01405_si_001.pdf

4.7 Simultaneous detection of light elements under non-Rutherford scattering

H. Naramoto, M. Sataka, H. Kudo, K. Sasa

Our ion beam analysis system is equipped with the high-precision rotational systems for sample alignment and sample-detector arrangement. The rotational systems are required to be calibrated referring to the beam direction which depends on the beam transport carried out every time for individual experiments. We have been concerned with the sensitive analysis of low Z elements, especially hydrogen, employing the non-Rutherford scattering process [1], and the angle calibration method has been developed based on the elastic recoil process under transmission using the model film of Mylar(0.9 μm)/Al(8 μm)/Mylar(0.9 μm)/Al(80 μm) on a modified sample holder. The angle calibration of sample-detector arrangement system was performed by evaluating the peak-energy change of hydrogen recoil spectra from the 1st Mylar layer (the topmost layer) of the same model film [2], which reflects the relevant collision kinetics directly. In this report, are described the calibration procedure of sample alignment system and the subsequent study of simultaneous detection of hydrogen and oxygen on a 4N pure Fe film (50 μm) surface.

Figure 1 shows a set of transmitted hydrogen recoil spectra at 0° from the model film under different incident angles of 8 MeV $^4\text{He}^{2+}$ around the surface normal of sample holder. In this calibration, attention was paid to the recoil spectra from the 2nd Mylar layer of the model film because more pronounced peak shift than for the 1st layer can be expected to occur by reflecting the energy loss of incident $^4\text{He}^{2+}$ at the inserted Al(8 μm) layer. By assuming the symmetric change of recoil-peak energies with the sample holder rotation, the surface normal was determined to be +4.09° as illustrated in Fig. 2. The more refined calibration can be realized by designing a sample holder capable of the in-plane rotation.

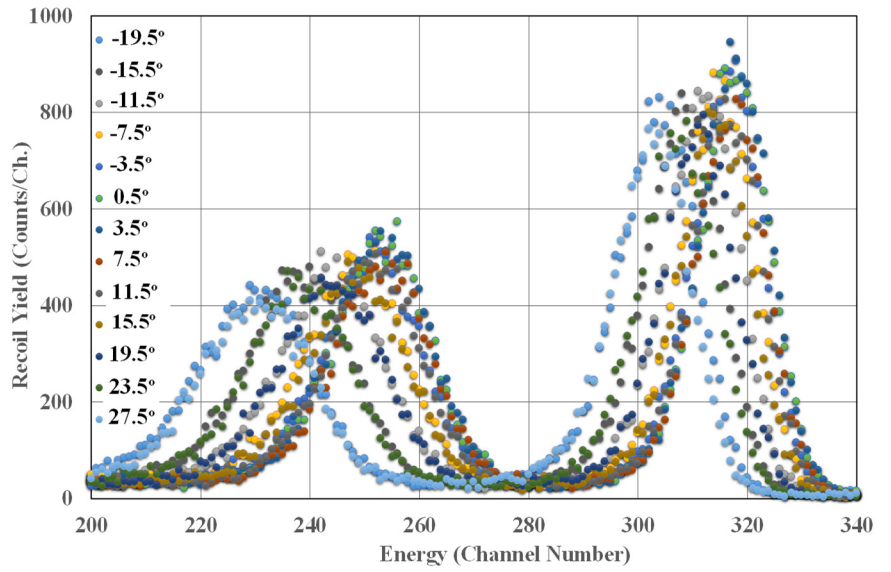


Fig. 1. Transmitted hydrogen recoil spectra at 0° from the model film for nominal incident angles of 8 MeV $^4\text{He}^{2+}$.

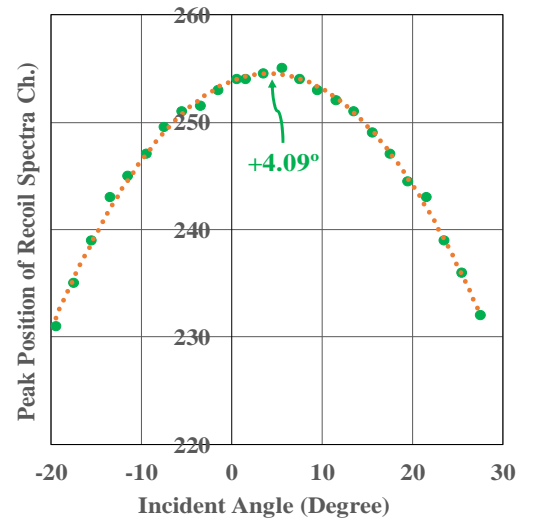


Fig. 2. The surface normal calibration of sample holder based on transmitted hydrogen recoil spectra from the 2nd Mylar in Fig. 1.

Following the establishment of angular calibration method, we have analyzed the possible contamination of water molecules on the 4N pure Fe film surface in order to obtain the information on the origin of background in recoil hydrogen spectra and also on the simultaneous detection of other low Z elements together with hydrogen on a high Z substrate.

Figure 3 shows three kinds of recoil spectra at 0° under the normal incidence of 8-10 MeV $^4\text{He}^{2+}$ onto the 4N pure Fe film. One can see the sensitive detection of hydrogen recoils from the water molecules just on the 4N pure Fe surface. The features of background spectra are rather smooth irrespective of the energy change of incident $^4\text{He}^{2+}$, and it would be easy to subtract such smooth backgrounds.

Figure 4 shows backscattering spectra at 168.5° from the same Fe sample, which were measured for 8, 9, and 10 MeV $^4\text{He}^{2+}$. These spectra were recorded simultaneously with the recoil spectra shown in Fig. 3. The spectral features are basically smooth, but the appearance of the sharp peak at 312 Ch. on the smooth backscattering spectrum can be seen only for 10 MeV $^4\text{He}^{2+}$. The more distinctive peaking was confirmed on the oxidized Cu sample (not shown for the simplicity), which can be associated with $^{16}\text{O}(\alpha, \alpha_0)^{16}\text{O}$ resonant elastic scattering [3].

As suggested above, the combined use of transmission recoiling and resonant elastic backscattering with 8-10 MeV $^4\text{He}^{2+}$ can be beneficial for the simultaneous detection of hydrogen and other low Z elements on the surface region of substrates with high Coulomb barriers. The process of simultaneous detection can be effectively applied for the position-sensitive composition analysis by taking advantage of a micro-beam scanning system for high-energy ions [4].

References

- [1] A. Yamazaki et al., AIP Advances 9 (2019) 105111.
- [2] H. Naramoto et al., UTTAC Annual Report 2017, UTTAC-87 (2018) 47.
- [3] IBANDL (Ion Beam Analysis Nuclear Data Library). <https://www-nds.iaea.org/exfor/ibandl.htm>
- [4] A. Yamazaki et al., Nucl. Instr. Meth. Phys. Res. B 404 (2017) 92.

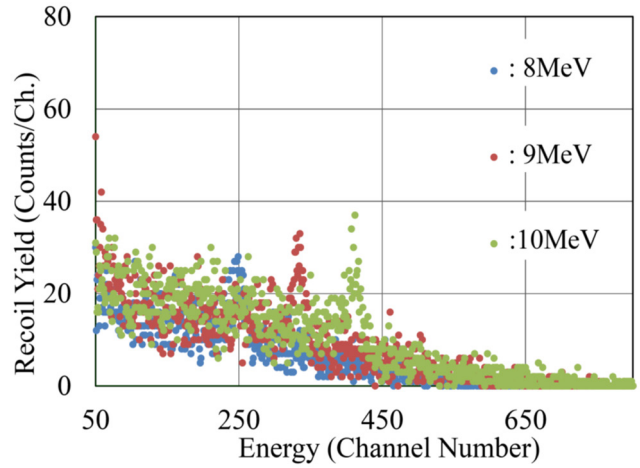


Fig. 3. Transmitted recoil spectra at 0° under the normal incidence of 8-10 MeV $^4\text{He}^{2+}$ ions onto the 4N pure Fe film. The recoil yields in the spectra are normalized to the accumulated charge of $10\mu\text{C}$.

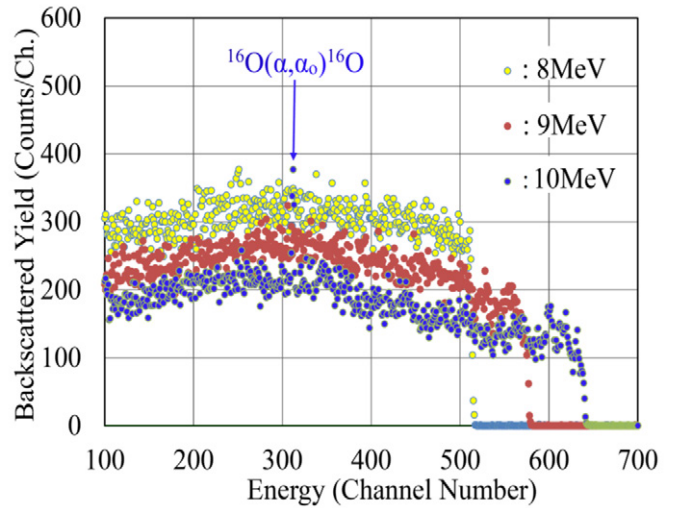


Fig. 4. Backscattering spectra from the 4N pure Fe film at 168.5° simultaneously taken with those in Fig. 3. The yield was normalized under the same condition.

4.8 Recombination effect in the output pulse height of superconducting tunnel junction for the incidence of keV ions

S. Tomita, S. Shiki¹, G. Fujii¹, T. Takahashi, K. Sasa, M. Ukibe¹

Superconducting tunnel junction (STJ) has a sandwich structure of superconductor-insulator-superconductor (SIS) tunnel junctions which enables the detection of low-energy particles through phonon excitation at the detector surface [1]. The phonons whose energy is greater than 2Δ can subsequently be absorbed by Cooper pairs, producing a number of quasiparticles which can quantum mechanically tunnel through the thin insulating barrier. The magnitude of the tunneling current pulse is proportional to the number of quasiparticles which is proportional to the energy deposited into the detector by the impacting particle. Thus, STJ can be used for the energy-sensitive detection of particles, especially keV molecules which are unable to detect with standard surface-barrier semiconductor detectors. Actually, STJ has been successfully used for detection of X-ray and keV molecules [2]. But, the energy resolution for the detection of molecules is relatively poor compared to that of X-ray. Even more, it has been reported that there is a significant pulse height defect for the large molecules [3]. The reason for the difference is not fully understood yet. The energy loss due to secondary particle emission, such as, secondary ion emission and electron emission, could be a possible mechanism. Another possibility is the increase of leak current stems from the infrared light shed on the STJ surface.

To understand the difference in the STJ response of X-ray and ions, we have measured X-ray and ions in same experimental conditions (temperature, infrared light, electronic noises). The experiments were performed with double-focusing mass spectrometer (JEOL JMS-600W). The ions generated with electron impact ionization of air was accelerated with potential difference of 3 kV and the mass analyzed ions according to their mass to charge ratio impinged on the STJ. The size of STJ was 100 μm square with a layer of Nb/Al/ AlO_x /Al/Nb electrode. The STJ was mounted on ^3He cryostat with the base temperature of about 300 mK with a blocking filter of infrared light [4]. An X-ray emitter was arranged in parallel to the ion beam line so that the STJ can be moved in front of the source to perform X-ray measurement with the same condition as ion measurements.

The pulse height distributions of the STJ signal of 3keV H^+ and N^+ are shown in Fig. 1, together with that of X-ray of Al-K α (1.486 keV). The small peak located at higher channel corresponds to N_2^{2+} ions of 6keV which has the same velocity as 3keV N^+ . The pulse height is scaled according to the kinetic energy of impinging particle. The scaled pulse heights of ions are almost the same to that of X-rays, thus, the pulse height defect due to loss of secondary particle emission is negligible at least in this case. The absolute energy resolution of an X-ray signal is poorer than that of normal X-ray measurement with protection of infrared light. Thus, the detector temperature and the amount of infrared light shed on the detector surface seems to be important for the energy resolution. However, the absolute width of the peak is not the same for the X-ray and ions, thus the fluctuation of the leak current is not the main cause of the energy resolution. The pulse

¹ National Institute of Advanced Industrial Science and Technology (AIST)

height for H^+ is higher than that of X-ray or N^+ . This could be the result of the density effect of excited particles rather than that of difference in the excitation process of quasi particles. Because the pulse height of N_2^{2+} ion is much lower than the twice of the pulse height of N^+ ion, even though both ions have the same velocity. The relaxation process of their kinetic energy is the same for both cases. This means that density effect of excited particles, e.g., recombination of quasi particles, may play an important role for the pulse height defect process.

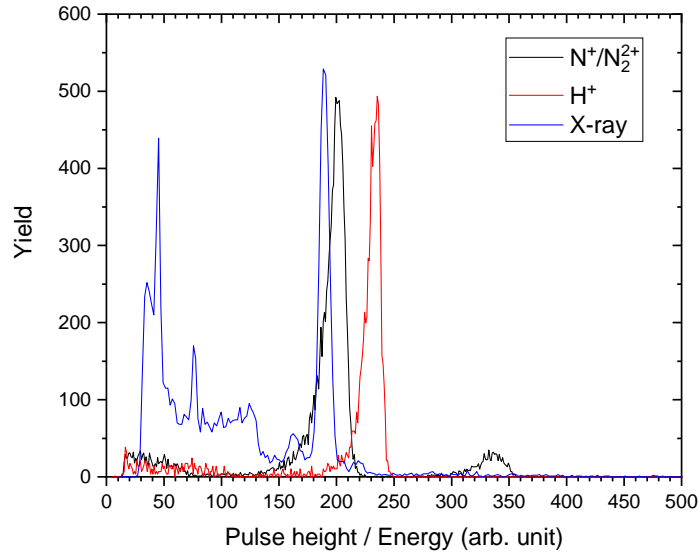


Fig. 1. Pulse height spectra of H^+ (3keV) (red line), N^+ / N_2^{2+} (3keV) (black line), and Al- $K\alpha$ X-ray (1.486 keV) (blue line). Pulse heights are scaled according to the kinetic energy of the impinging particle.

References

- [1] P. Lerch and A. Zehnder, in *Cryogenic Particle Detection*, edited by C. Enss (Springer Berlin Heidelberg, 2005), pp. 217.
- [2] M. Ohkubo et al., *IEEE Transactions on Applied Superconductivity* 24 (2014) 1.
- [3] S. Tomita et al., *Appl. Phys. Lett.* 91 (2007) 053507.
- [4] S. Shiki, et al, *Nucl. Instr. Meth. Phys. Res. A* 595 (2008) 391.

4.9 Heteroepitaxial growth of thin films of the perovskite oxynitride CaTaO_2N by reactive magnetron sputtering

T. Wakasugi¹, Y. Hirose¹, Y. Sugisawa, D. Sekiba

Perovskite oxynitrides have been studied because of their visible light driven photocatalytic activity and novel electronic functions.¹ Assessment of the intrinsic physical and/or electrochemical properties of oxynitrides requires the epitaxial growth of single crystalline films. However, the heteroepitaxy of perovskite oxynitrides has not yet matured compared to the progress realized in work with perovskite oxides. Herein, we studied the heteroepitaxial growth of CaTaO_2N thin films with $(100)_{\text{pc}}$, $(110)_{\text{pc}}$ and $(111)_{\text{pc}}$ crystallographic surface orientations on SrTiO_3 substrates (where the subscript pc denotes a pseudo-cubic cell), along with investigations of crystallinity and surface morphology.

CaTaO_xN_y thin films were deposited by reactive RF magnetron sputtering using a CaTaO_x ceramic target. During the thin film deposition process, the substrate temperature was maintained at 630 °C and Ar and N_2 were introduced into the chamber. The total gas pressure and total gas flow rate were set at 0.75 Pa and 20 standard $\text{cc} \cdot \text{min}^{-1}$, respectively. The N_2 partial pressure, P_{N_2} , was varied between 0 and 0.3 Pa to adjust the N content in the films. The input RF power and the target-substrate distance were set at 100 W and 12 cm, respectively. The N to Ta ratios (N/Ta) of the thin films were estimated from the N amounts determined by heavy ion elastic recoil detection analysis (ERDA) and the Ta amounts determined by Rutherford backscattering spectrometry (RBS) with a 38.4 MeV ^{35}Cl beam generated by a 5 MV tandem accelerator (MALT).² The crystal structures were analyzed using X-ray diffraction (XRD).

Figure 1(a) shows the θ -2 θ XRD patterns obtained from a series of the CaTaO_xN_y thin films grown on SrTiO_3 (100) substrates under various P_{N_2} . Each of these patterns confirms the epitaxial growth of $(100)_{\text{pc}}$ -oriented perovskite. Nevertheless, the N/Ta ratios vary from 0 to 1 in the present range of P_{N_2} , as seen in Fig. 1(b). The perovskite structure is evidently kept even in the case of the film containing no N ($P_{\text{N}_2} = 0$), possibly due to the formation of cation vacancies. Notably, the N/Ta ratio increases with increasing P_{N_2} and reaches a plateau of the level

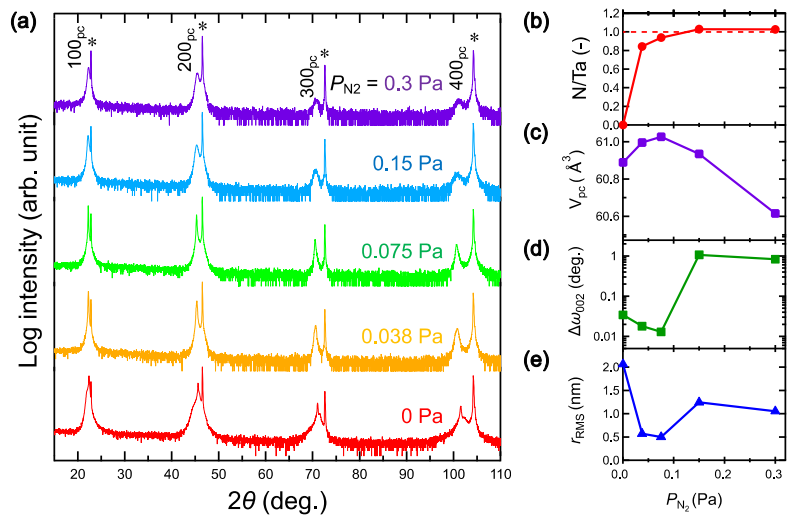


Fig. 1. (a) The θ -2 θ XRD patterns of CaTaO_xN_y thin films grown on SrTiO_3 (100) under various P_{N_2} (asterisks denote diffraction peaks from the substrate). (b) N/Ta ratios, (c) full width at half maximum of the 200 diffraction rocking curves, (d) unit cell volumes based on a pseudo-cubic approximation, and (e) root mean square roughness values of films, r_{RMS} , all plotted against P_{N_2} .

¹ The University of Tokyo

approximately equal to 1 at $P_{N_2} \geq 0.075$ Pa. This result suggests that the N concentration is self-limited by crystallization into the perovskite structure. With increasing P_{N_2} , the cell volume per formula unit, V_{pc} , of the CaTaO_xN_y thin films increases up to the maximum of 0.0610 nm^3 at $P_{N_2} = 0.075$ Pa, as seen in Fig. 1(c). This V_{pc} value is in good agreement with the calculated value for biaxially strained CaTaO_2N assuming a Poisson's ratio of 0.30 which is a typical value for oxynitrides. Further increase in P_{N_2} causes decrease in V_{pc} , suggesting the formation of lattice defects. Figures 1(d) and (e) show the P_{N_2} -dependence of the full width at half maximum of the rocking curve for the 200_{pc} diffraction and the root mean square roughness of the CaTaO_xN_y thin film, respectively. In both cases, the measured quantity decreases as P_{N_2} increases from 0 to 0.075 Pa, and reach a minimum at $P_{N_2} = 0.075$ Pa. We speculate that the degradation of crystallinity and volume reduction at P_{N_2} higher than 0.075 Pa originate from slight off-stoichiometry such as excess nitrogen, which could not be detected by the compositional analysis.

Figure 2(a) presents the θ - 2θ XRD patterns of 20-nm thick CaTaO_2N films grown on the (100), (110) and (111) planes of SrTiO_3 substrates, while Figs. 2(b)-(d) are the reciprocal space maps (RSMs) of these films. Both the XRD patterns and RSMs confirm the epitaxial growth of CaTaO_2N thin films with the same orientations (in a pseudo-cubic approximation) as the substrate surfaces. The RSMs also indicate that the in-plane lattice constants of the CaTaO_2N are locked to those of the SrTiO_3 substrates. Comparing the three RSMs for different crystallographic orientations leads to concluding that the $(110)_{pc}$ oriented film is

more highly crystalline than the films with other orientations, since the films grown on SrTiO_3 (100) and (111) substrates generate broader diffraction spots along the in-plane direction than that on the (110) substrate. Because all these films have the same N/Ta ratios within an experimental error, we attribute this evident variation in crystallinity not to deviations from stoichiometry but rather to reflected symmetry mismatch between CaTaO_2N (orthorhombic) and SrTiO_3 (cubic), which results in formation of multiple domains with different in-plane crystallographic orientations for $(100)_{pc}$ - and $(111)_{pc}$ -oriented thin films.³

References

- [1] T. Takata et al., Sci. Technol. Adv. Mater. 16 (2015) 033506.
- [2] I. Harayama et al., Nucl. Instr. Meth. Phys. Res. B 384 (2016) 61.
- [3] T. Wakasugi et al., ACS Omega 5 (2020) 13396.

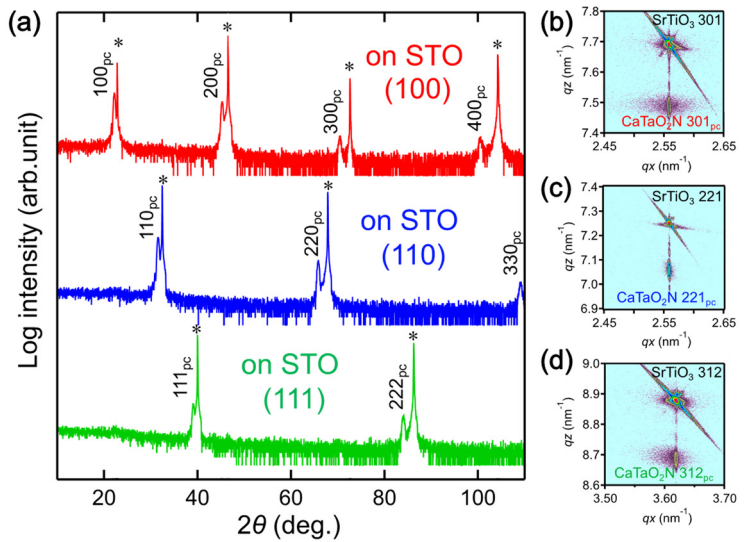


Fig. 2. (a) The θ - 2θ XRD patterns of 20 nm-thick CaTaO_2N thin films grown on SrTiO_3 (100), (110) and (111) substrates (asterisks denote diffraction peaks from the substrates). (b-d) The XRD RSMs for the films grown on SrTiO_3 (b) (100), (c) (110), and (d) (111) substrates.

4.10 Electric properties of magnesium titanium oxynitride thin films

A. Ogura, Y. Sugisawa, D. Sekiba, H. Yanagihara

One of the ways to evolve the spintronics is to improve the performance of magnetic tunnel junctions (MTJs). A device structure of conventional MTJs is a tri-layer system composed of two ferromagnetic metal layers/electrodes separated by a very thin non-magnetic insulator layer/tunneling barrier. As an alternative, spin-filter devices are proposed, in which the tunneling barrier is *ferromagnetic* insulator. Ferromagnetic insulator can be expected to generate highly-spin-polarized tunneling current because the band gaps dependent on spin state is much different [1]. Among the various ferromagnetic insulating compounds, spinel ferrites are promising materials for the tunneling barrier of the spin-filter devices because of the high Curie temperature and high electric resistivity. Some spin-filter devices with the spinel ferrite barrier have been reported, however, the observed magnetoresistance ratios are very small [2]. In order to realize ideal spin-filter devices with spinel ferrites, we have to carefully control the film growth process and also to explore appropriate buffer layers at the first onset. In this case, the buffer layer works not only as a template for the epitaxial growth of upper layer/barrier but also as a bottom electrode of MTJs. Since non-negligible amount of defects such as anti-phase boundaries occur at the initial growth of spinel ferrite thin films on (001)-plane of cubic system with a lattice constant approximately half of the spinel like MgO [3], we need to find conductive compounds with the lattice constant comparable to that of the spinel ferrites. As a candidate, we focused on magnesium titanium oxynitrides (MTON). We attempted to grow epitaxial MTON films. In this report, we show how the growth condition affects the composition, structure, and electric properties.

We grew samples with a reactive magnetron sputtering technique introducing process gases of argon and/or nitrogen. The sputtering target was MgTi_2O_4 ceramics and the substrates were single crystal $\text{MgO}(001)$. Crystal structures of the films were investigated by x-ray diffraction (XRD) technique as well as *in situ* reflection high energy electron diffraction (RHEED) images. Composition of the films were determined by TOF-E telescope ERDA (Elastic Recoil Detection Analysis) at UTTAC. $^{35}\text{Cl}^{4+}$ ions extracted from the sputtering ion source were charge-exchanged and accelerated up to 4 MeV and used as a probe beam after shaped as $1 \times 1 \text{ mm}^2$ by a double slit system. The recoils were detected at the angle of 30 degree with respect to the beam direction. Temperature dependences of both electric resistivity and Hall conductivity were measured by van der Pauw method.

Figures 1(a) and (b) show RHEED images of $\text{MgO}(001)$ substrate and MTON(001) films grown with nitrogen gas without argon gas at 500°C ,

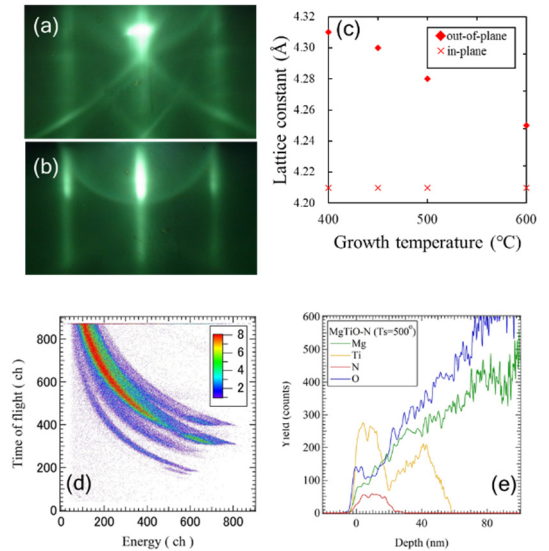


Fig. 1. (a) and (b): RHEED images, (c): lattice constants, (d): ERDA/RBS spectra, and (e): depth profile of the elements.

respectively. The streak pattern from MTON(001) is similar to that from the substrate, implying that the crystal structure of the film is a rock-salt, rather than spinel, type. This is consistent with the XRD results since observed Bragg points of the film grown with pure nitrogen gas also indicates a rock-salt structure. On the other hand, when the film is grown with a mixture gas of argon and nitrogen, some films exhibit a spinel structure. The process (or growth) temperature dependent lattice constants both for in-plane and out-of-plane axes determined by XRD are summarized in Fig. 1(c). The lattice constant of out-of-plane axis decreases with increasing the growth temperature, while that of in-plane seems to be independent of the temperature. The in-plane lattice constant could be locked to the substrate.

TOF-E telescope ERDA results for the film grown at 500°C are shown in Fig. 1(d) and (e). The depth-profiles shown in Fig. 1(e) which is obtained from Fig. 1 (d) indicate that oxygen and nitrogen coexist in the film, meaning the obtained film is a mixed anion compound. The composition of the film is estimated as Mg: 21%, Ti: 53%, O:19%, and N: 6%.

We have prepared more than 10 films under different growth conditions with and without argon gas. Among them, the films grown at 500 and 600°C without argon gas, i.e., with nitrogen gas only, become conductive at room temperature. The observed values of electrical resistivity of the films at 500 and 600°C are $3.7 \times 10^{-3} \Omega \text{ cm}$ and $1.1 \times 10^{-3} \Omega \text{ cm}$, respectively. The sample grown at a higher temperature seems to have lower resistivity. According to Fig. 1(d) and (e), the films sputtered with nitrogen gas only are composed of nitrogen and oxygen. Since both the ceramic target and the films grown with argon gas only are electrically insulating, the mixed-anion state [4] of MTON is a key to understand the emergence of conductivity.

References

- [1] Jagadeesh S. Moodera et al., J. Phys. Condens. Matter 19 (2007)165202.
- [2] Y. K. Takahashi et al., Appl. Phys. Lett. 96 (2010) 072512.
- [3] S. Celotto et al., Eur. Phys. J. B 36 (2003) 271.
- [4] Hyun-Suk Kim et al., Sci. Rep. 3 (2013) 1459.

5.

BEAM IRRADIATION EFFECT



Vacuum chamber for radiation tolerance test of semiconductor devices used in space. The built-in mechanism enables ion-beam scanning on A5 size area.

5.1 Study on microalgae mutagenesis with ^{15}N -resonant nuclear reaction

I. Suzuki, R. Morioka, K. Sasa, S. Ishii, K. Tomita¹, Y. Iwata¹

Natural products such as oils, polysaccharides, and pigments are now being reinvented as essential to a sustainable society. Microalgae are superior to both the edible and inedible plants in synthesizing and accumulating such natural products in high density and in a short term. Accordingly, microalgae are attracting attention in a wide industrial field of energetics, dietary, nutrition, cosmetics, and pharmaceuticals. There is still strong resistance in industry to the improvement through GMO (genetically modified organisms), even though a breeding program of microalgae is necessary to develop more desirable strains with high productivity. Random mutagenesis, which is optimized in terms of the dose of mutagen such as effective heavy ion beams as well as typical UV, X-rays, gamma-rays, and also such chemical agent as ethyl-methane sulfonate, is exempt from the regulation of GMO. However, such random mutagenesis requires time-consuming processes for selecting the target mutants, much less to induce a genetic mutation expressing the target phenotypic trait in microalgae.

The authors focused on nitrogen atom N which is the main constituent in DNA (deoxyribonucleic acid); seven nitrogen atoms are in every pair of adenine and thymine (AT pair) and eight nitrogen atoms in every pair of guanine and cytosine (GC pair). Substituting every nitrogen atom in DNA with a stable nitrogen isotope ^{15}N enriched higher than 98% in abundance, we can obtain DNA labeled with ^{15}N isotope ($^{15}\text{N_DNA}$). Proton irradiation to $^{15}\text{N_DNA}$ induces the $^{15}\text{N}(p, \alpha_1\gamma)^{12}\text{C}$ resonant nuclear reaction at resonant energy of 0.897 MeV, and then deletion of the target ^{15}N nucleus and high-density excitation of molecules near the target ^{15}N by secondary ions of α ($^4\text{He}^{2+}$) and $^{12}\text{C}^{6+}$ happen inside $^{15}\text{N_DNA}$. Resultantly, ^{15}N -specific mutagenesis to DNA is possibly realized since the electronic excitation effect of proton at the resonant energy is much smaller than that of the secondary heavy ions. This new mutagenesis has an advantage exceeding heavy ion irradiation of the conventional random mutagenesis, where a whole cell is exposed to high-density excitation. Furthermore, the 4.43 MeV gamma-rays from the ^{15}N -resonant nuclear reaction possess high penetration power through matter, hence they are detectable from the outside of the vacuum irradiation system. The detection of 4.43 MeV gamma-rays enables to accurately monitor the number of ^{15}N -resonant nuclear reaction occurring in $^{15}\text{N_DNA}$ during proton beam irradiation. Careful analyses of the relation between mutant strains and 4.43 MeV gamma-ray yields lead to establishing a new art of a simultaneous counting system of genetic mutation.

We performed an examination of the new mutagenesis to an artificial DNA and freeze-dried *Escherichia coli* (JM109) [1, 2]. ^{15}N -enriched Oligo DNA of 84 bps (base pairs) containing ^{15}N with abundance higher than 98% was artificially generated by the PCR (polymerase chain reaction) method. The ^{15}N -labeled Oligo DNA has a molecular mass of 51,773 Da and contains 549 ^{15}N atoms. The proton-irradiated Oligo DNA specimens were ligated with the plasmid DNA harboring the ampicillin resistance gene. The plasmid DNA ligated with a non-damaged Oligo DNA specimen forming a ring shape plays a role of the plasmid annular

¹ National Institute of Advanced Industrial Science and Technology (AIST).

vector to *Escherichia coli*, which can grow to form colonies on the medium with ampicillin. The number of colonies of JM109 grown in the agar medium containing the plasmid DNA ligated with ^{15}N -labeled Oligo DNA were obviously reduced. The result indicated that the ^{15}N -labeled Oligo DNA was ruptured by proton beam irradiation and failed to form a plasmid annular vector in JM109 comparing to the non-irradiation conditions.

Freeze-dried cells of *Escherichia coli* (JM109) were possibly alive in the vacuum system for proton beam irradiation. ^{15}N -labeled JM109 cells grown in the agar medium fed with $^{15}\text{NH}_4^+$ ions contain ^{15}N in every cell organ such as the protein, the nucleic acid, and the cortex. Glutamine synthetase inhibitor of MSX (methionine sulfoximine) plays a role to stop the ^{15}N flow to the system synthesizing the protein and the cortex through the glutamyl cycle. We obtained *Escherichia coli* (JM109) strains that have the specific nucleic acid labeled with ^{15}N .

Proton beam irradiation was carried at energies from 0.884 MeV to 0.906 MeV around the center of the resonant energy of 0.897 MeV using both the 1 MV Tandetron at UTTAC and 4 MV Van de Graaff accelerator at AIST. Typical beam current was 1 nA for irradiation to the artificial DNA and 0.1 nA for microalgae. 4.43 MeV gamma-ray yields were detected with a BGO ($\text{Bi}_4\text{Ge}_3\text{O}_{12}$) detector. Figure 1 shows measured gamma-ray spectra, where the natural background is so low as to detect the signals from the 4.43 MeV gamma-rays with high efficiency.

The authors will clarify in future works the validity of the new mutagenesis with the ^{15}N -resonant nuclear reaction: the effects of deletion of the target ^{15}N nucleus and high-density excitation of molecules near the target ^{15}N , and the art of introduction of ^{15}N inside the target genes or the nearest position to them.

References

- [1] Y. Iwata et al., European Advanced Materials Congress (EAMC2019), Stockholm, August 11 – 14, 2019.
- [2] R. Morioka et al., The 2019 International Postgraduate Academic Forum, China University of Geosciences, Beijing, September 20 – 23, 2019.

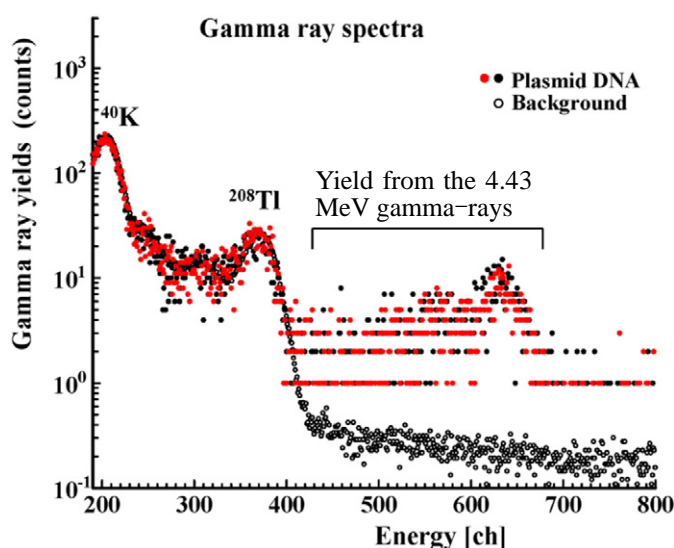
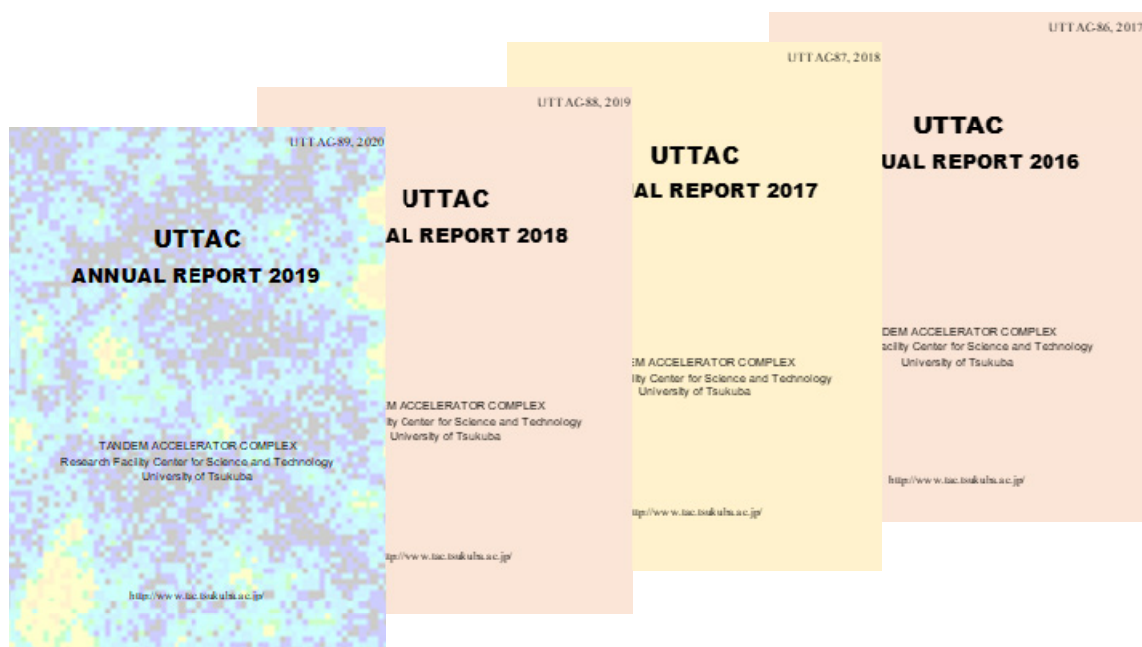


Fig. 1. Gamma ray spectra emitted from $^{15}\text{N}(^1\text{H}, \alpha_1\gamma)^{12}\text{C}$ resonant nuclear reaction. ^{40}K and ^{208}Tl indicate the natural 1.4608 MeV and 2.6145 MeV peaks, respectively.

6.

LIST OF PUBLICATIONS AND PRESENTATIONS



Research reports published on the UTTAC web since 2016 when the 6MV tandem accelerator started regular operation after 2 years of construction.

6.1 Journals

ACCELERATOR AND RELATED FACILITIES

1. H. Nakamura, H. Matsumura, G. Yoshida, A. Toyoda, K. Masumoto, T. Miura, K. Sasa, and T. Moriguchi, “Investigation of neutron-fluence measurement methods for estimating neutron-induced activity from an electrostatic accelerator source”, *Environmental Radiochemical Analysis VI*, Royal Society of Chemistry (2019) 152.

NUCLEAR AND ATOMIC PHYSICS

1. M. Tanaka, M. Takechi, A. Homma, M. Fukuda, D. Nishimura, T. Suzuki, Y. Tanaka, T. Moriguchi, D.S. Ahn, A. Aimaganbetov, M. Amano, H. Arakawa, S. Bagchi, K.-H. Behr, N. Burtebayev, K. Chikaato, H. Du, S. Ebata, T. Fujii, N. Fukuda, H. Geissel, T. Hori, W. Horiuchi, S. Hoshino, R. Igosawa, A. Ikeda, N. Inabe, K. Inomata, K. Itahashi, T. Izumikawa, D. Kamioka, N. Kanda, I. Kato, I. Kenzhina, Z. Korkulu, Y. Kuk, K. Kusaka, K. Matsuta, M. Mihara, E. Miyata, D. Nagae, S. Nakamura, M. Nassurlla, K. Nishimuro, K. Nishizuka, K. Ohnishi, M. Ohtake, T. Ohtsubo, S. Omika, H. J. Ong, A. Ozawa, A. Prochazka, H. Sakurai, C. Scheidenberger, Y. Shimizu, T. Sugihara, T. Sumikama, H. Suzuki, S. Suzuki, H. Takeda, Y.K. Tanaka, I. Tanihata, T. Wada, K. Wakayama, S. Yagi, T. Yamaguchi, R. Yanagihara, Y. Yanagisawa, K. Yoshida, and T.K. Zholdybayev, “Swelling of doubly magic ^{48}Ca core in Ca isotopes beyond $N = 28$ ”, *Phys. Rev. Lett.* 124 (2020) 102501.
2. T. Moriguchi, M. Amano, A. Ozawa, W. Horiuchi, Y. Abe, T. Fujii, R. Kagesawa, D. Kamioka, A. Kitagawa, M. Mukai, D. Nagae, M. Sakaue, S. Sato, S. Suzuki, T. Suzuki, T. Yamaguchi, and K. Yokota, “Energy dependence of total reaction cross sections for ^{17}Ne on a proton target”, *Nucl. Phys. A* 994 (2020) 121663.
3. S. Omika, T. Yamaguchi, N. Tadano, Y. Abe, M. Amano, Z. Ge, D. Kamioka, T. Moriguchi, D. Nagae, S. Naimi, A. Ozawa, F. Suzaki, S. Suzuki, T. Suzuki, T. Uesaka, M. Wakasugi, K. Wakayama, and Y. Yamaguchi, “Development of a new in-ring beam monitor in the Rare-RI Ring”, *Nucl. Instrum. Methods B* 463 (2020) 241.
4. Z. Ge, T. Uesaka, S. Naimi, D. Nagae, Y. Abe, S. Omika, F. Suzaki, T. Yamaguchi, Y. Yamaguchi, M. Wakasugi, H. Li, K. Wakayama, H. Arakawa, K. Inomata, K. Nishimuro, T. Kobayashi, A. Ozawa, S. Hosoi, Y. Inada, S. Suzuki, T. Moriguchi, M. Mukai, M. Amano, D. Kamioka, and Y. Yano, “Scheme of high-resolution identification and selection of secondary ions for mass measurements with the Rare-RI Ring”, *Hyperfine Interact.* 92 (2019) 240.

5. M. Machida, D. Nishimura, M. Fukuda, S. Yagi, T. Sugihara, S. Kanbe, S. Yamaoka, M. Takechi, M. Tanaka, M. Amano, J. Chiba, K. Chikaato, H. Du, S. Fukuda, A. Homma, T. Hori, A. Ikeda, R. Ishii, T. Izumikawa, Y. Kamisho, N. Kanda, R. Kehl, A. Kitagawa, K. Matsuta, M. Mihara, E. Miyata, A. Mizukami, T. Moriguchi, M. Nagashima, S. Nakamura, M. Nassurlla, K. Ohnishi, T. Ohtsubo, S. Sato, J. Shimaya, T. Suzuki, S. Suzuki, T. Tahara, Y. Tanaka, T. Yamaguchi, and R. Yanagihara, “Development of prototype RICH detector with multi-anode photomultipliers for radioactive ions”, Nucl. Instrum. Methods A 931 (2019) 23.

6. X. Xu, J.H. Liu, C.X. Yuan, Y.M. Xing, M. Wang, Y.H. Zhang, X.H. Zhou, Yu.A. Litvinov, K. Blaum, R.J. Chen, X.C. Chen, C.Y. Fu, B.S. Gao, J.J. He, S. Kubono, Y.H. Lam, H.F. Li, M.L. Liu, X.W. Ma, P. Shuai, M. Si, M.Z. Sun, X.L. Tu, Q. Wang, H.S. Xu, X.L. Yan, J.C. Yang, Y.J. Yuan, Q. Zeng, P. Zhang, X. Zhou, W.L. Zhan, S. Litvinov, G. Audi, S. Naimi, T. Uesaka, Y. Yamaguchi, T. Yamaguchi, A. Ozawa, B.H. Sun, K. Kaneko, Y. Sun, and F.R. Xu, “Masses of ground and isomeric states of ^{101}In and configuration-dependent shell evolution in odd-A indium isotopes”, Phys. Rev. C 100 (2019) 051303.

7. F.C. Ozturk, B. Akkus, D. Atanasov, H. Beyer, F. Bosch, D. Boutin, C. Brandau, P. Bühler, R.B. Cakirli, R.J. Chen, W.D. Chen, X.C. Chen, I. Dillmann, C. Dimopoulou, W. Enders, H.G. Essel, T. Faestermann, O. Forstner, B.S. Gao, H. Geissel, R. Gernhäuser, R.E. Grisenti, A. Gumberidze, S. Hagmann, T. Heftrich, M. Heil, M.O. Herdrich, P.-M. Hillenbrand, T. Izumikawa, P. Kienle, C. Kraushofer, C. Kleffner, C. Kozhuharov, R.K. Knöbel, O. Kovalenko, S. Kreim, T. Kühl, C. Lederer-Woods, M. Lestinsky, S.A. Litvinov, Yu.A. Litvinov, Z. Liu, X.W. Ma, L. Maier, B. Mei, H. Miura, I. Mukha, A. Najafi, D. Nagae, T. Nishimura, C. Nociforo, F. Nolden, T. Ohtsubo, Y. Oktem, S. Omika, A. Ozawa, N. Petridis, J. Piotrowski, R. Reifarth, J. Rossbach, R. Sánchez, M.S. Sanjari, C. Scheidenberger, R.S. Sidhu, H. Simon, U. Spillmann, M. Steck, Th. Stöhlker, B.H. Sun, L.A. Susam, F. Suzuki, T. Suzuki, S. Yu. Torilov, C. Trageser, M. Trassinelli, S. Trosenko, P.M. Walker, M. Wang, G. Weber, H. Weick, N. Winckler, X.L. Tu, D.F.A. Winters, P.J. Woods, T. Yamaguchi, X.D. Xu, X.L. Yan, J.C. Yang, Y.J. Yuan, Y.H. Zhang, X.H. Zhou, and the FRS-ESR, ILIMA, SPARC, and TBWD Collaborations, “New test of modulated electron capture decay of hydrogen-like ^{142}Pm ions: Precision measurement of purely exponential decay”, Phys. Lett. B 797 (2019) 134800.

8. X. Xu, M. Wang, K. Blaum, J.D. Holt, Yu.A. Litvinov, A. Schwenk, J. Simonis, S.R. Stroberg, Y.H. Zhang, H.S. Xu, P. Shuai, X.L. Tu, X.H. Zhou, F.R. Xu, G. Audi, R.J. Chen, X.C. Chen, C.Y. Fu, Z. Ge, W.J. Huang, S. Litvinov, D.W. Liu, Y.H. Lam, X.W. Ma, R.S. Mao, A. Ozawa, B.H. Sun, Y. Sun, T. Uesaka, G.Q. Xiao, Y.M. Xing, T. Yamaguchi, Y. Yamaguchi, X.L. Yan, Q. Zeng, H.W. Zhao, T.C. Zhao, W. Zhang, and W.L. Zhan, “Masses of neutron-rich $^{52-54}\text{Sc}$ and $^{54,56}\text{Ti}$ nuclides: The $N = 32$ subshell closure in scandium”, Phys. Rev. C 99 (2019) 064303.

9. J.T. Zhang, K. Yue, H.X. Li, X.L. Tu, C.J. Shao, P. Ma, B. Mei, X.C. Chen, Y.Y. Yang, X.Q. Liu, Y.M. Xing, K.H. Fang, Z.Y. Sun, M. Wang, Yu.A. Litvinov, T. Yamaguchi, P. Egelhof, Y.H. Zhang, and X.H. Zhou, “The development of in-ring reaction measurements at the HIRFL-CSR”, Nucl. Instrum. Methods A 948 (2019) 162848.
10. S. Suzuki, A. Ozawa, D. Kamioka, Y. Abe, M. Amano, H. Arakawa, Z. Ge, K. Hiraishi, Y. Ichikawa, K. Inomata, A. Kitagawa, T. Kobayashi, H. Fu Li, T. Matsumoto, T. Moriguchi, M. Mukai, D. Nagae, S. Naimi, S. Omika, S. Sato, Y. Tajiri, K. Wakayama, and T. Yamaguchi, “Efficiency and timing performance of time-of-flight detector utilizing thin foils and crossed static electric and magnetic fields for mass measurements with Rare-RI Ring facility”, Nucl. Instrum. Methods A 965 (2020) 163807.

ACCELERATOR MASS SPECTROMETRY

1. M. Matsumura, K. Sasa, T. Matsunaka, K. Sueki, T. Takahashi, and H. Matsuzaki, “Assessing the effect of laboratory environment on sample contamination for I-129 accelerator mass spectrometry”, Anal. Sci. 36 (2020) 631.
2. T. Matsunaka, K. Sasa, T. Takahashi, M. Matsumura, K. Sueki, and H. Matsuzaki, “Pre- and post-accident ^{14}C activities in tree rings near the Fukushima Dai-ichi Nuclear Power Plant”, Radiocarbon 61 (2019) 1633.
3. J. Chen, H. Shen, K. Sasa, H. Lan, T. Matsunaka, M. Matsumura, T. Takahashi, S. Hosoya, M. He, Y. He, Z. Li, Z. Zhao, Z. Zhao, M. Liu, S. Wei, M. Qi, Q. Zhao, X. Qin, X. Chen, and S. Jiang, “Radio carbon dating of Chinese ancient tea trees”, Radiocarbon 61 (2019) 1741.
4. H. Shen, K. Sasa, Q. Meng, M. Matsumura, T. Matsunaka, S. Hosoya, T. Takahashi, M. Honda, K. Sueki, M. He, B. Huang, Q. Zhao, K. Dong, Y. Guan, X. Ruan, and S. Jiang, “Exposure age dating of Chinese tiankengs by ^{36}Cl -AMS”, Nucl. Instrum. Methods B 459 (2019) 29.
5. H. Shen, K. Sasa, Q. Meng, M. Matsumura, T. Matsunaka, S. Hosoya, T. Takahashi, M. Honda, K. Sueki, L. Chen, H. Lu, M. He, B. Huang, Y. Qin, Z. Li, H. Lan, Z. Li, Z. Zhao, N. Liu, S. Wei, M. Qi, Q. Zhao, K. Dong, Y. Guan, and S. Jiang, “ ^{36}Cl preparation method for Chinese karst samples (Tiankeng)”, Nucl. Instrum. Methods B 458 (2019) 126.

1. A. Yamazaki, H. Naramoto, K. Sasa, S. Ishii, S. Tomita, M. Sataka, H. Kudo, M. Ohkubo, and A. Uedono, “Two-dimensional mapping of hydrogen and other elements in materials with microbeam-based transmission ERDA and PIXE”, *Nucl. Instrum. Methods B* 450 (2019) 319.
2. Y. Yamashita, Y. Takahara, T. Sato, K. Toko, A. Uedono, and T. Suemasu, “Simple way of finding Ba to Si deposition rate ratios for high photoresponsivity in BaSi₂ films by Raman spectroscopy”, *Appl. Phys. Express* 12 (2019) 055506.
3. H.J. Zhang, S. Sellaiyan, K. Sako, A. Uedono, Y. Taniguchi, and K. Hayashi, “Effect of free-volume holes on static mechanical properties of epoxy resins studied by positron annihilation and PVT experiments”, *Polymer* 190 (2020) 122225.
4. M. Shimizu, R. Álvarez-Asencio, N. Nordgren, and A. Uedono, “Preparation and characterization of cellulose acetate membranes with TEMPO-oxidized cellulose nanofibrils containing alkyl ammonium carboxylates”, *Cellulose* 27 (2019) 1357.
5. S. Sellaiyan, A. Uedono, L.V. Devi, and K. Sivaji, “Er³⁺ induced point defects in ZnO and impact of Li⁺/Na⁺/K⁺ on the vacancy defects in ZnO:Er studied by positron annihilation spectroscopy”, *Appl. Phys. A* 125 (2019) 498.
6. H. Iguchi, T. Narita, K. Kataoka, M. Kanechika, and A. Uedono, “Impact of defects on the electrical properties of p-n diodes formed by implanting Mg and H ions into N-polar GaN”, *J. Appl. Phys.* 126 (2019) 125102.
7. S. Ishibashi, A. Uedono, H. Kino, T. Miyake, and K. Terakura, “Computational study of positron annihilation parameters for cation mono-vacancies and vacancy complexes in nitride semiconductor alloys”, *J. Phys.: Condens. Matt.* 47 (2019) 475401.
8. A. Uedono, H. Iguchi, T. Narita, K. Kataoka, W. Egger, T. Koschine, C. Hugenschmidt, M. Dickmann, K. Shima, K. Kojima, S.F. Chichibu, and S. Ishibashi, “Annealing behavior of vacancy-type defects in Mg- and H-implanted GaN studied using monoenergetic positron beams”, *Phys. Status Solidi B* 256 (2019) 1900104.
9. S.F. Chichibu, K. Shima, K. Kojima, S. Takashima, K. Ueno, M. Edo, H. Iguchi, T. Narita, K. Kataoka, S. Ishibashi, and A. Uedono, “Room temperature photoluminescence lifetime for the near-band-edge emission of epitaxial and ion-implanted GaN on GaN structures”, *Jpn. J. Appl. Phys.* 58 (2019) SC0802.

10. A. Uedono, A.-M. Siladie, J. Pernot, B. Daudin, and S. Ishibashi, “Vacancy-type defects in GaN self-assembled nanowires probed using monoenergetic positron beam”, *J. Appl. Phys.* 125 (2019) 175705.
11. A. Uedono, K. Sako, W. Ueno, and M. Kimura, “Free volumes introduced by fractures of CFRP probed using positron annihilation”, *Composites Part A* 122 (2019) 54.
12. M. Sumiya, K. Fukuda, S. Takashima, S. Ueda, T. Onuma, T. Yamaguchi, T. Honda, and A. Uedono, “Structural disorder and in-gap states of Mg-implanted GaN films evaluated by photothermal deflection spectroscopy”, *J. Crys. Growth* 511 (2019) 15.
13. S. Sellaiyan, L. Vimala Devi, K. Sako, A. Uedono, and K. Sivaji, “Effect of dopant concentration and annealing of Yttrium doped CuO nanocrystallites studied by positron annihilation spectroscopy”, *J. Alloy. Compd.* 788 (2019) 549.
14. Y. Sato, S. Shibata, A. Uedono, K. Urabe, and K. Eriguchi, “Characterization of the distribution of defects introduced by plasma exposure in Si substrate”, *J. Vac. Sci. Technol. A* 37 (2019) 011304.
15. Y. Yamashita, Y. Takahara, T. Sato, K. Toko, A. Uedono, and T. Suemasu, “Simple way of finding Ba to Si deposition rate ratios for high photoresponsivity in BaSi₂ films by Raman spectroscopy”, *Appl. Phys. Express* 12 (2019) 05506.
16. A. Uedono, W. Egger, C. Hugenschmidt, and S. Ishibashi, “Effect of illumination on positron states in wide bandgap semiconductors”, 18th Int. Conf. Positron Annihilation (ICPA-18), *AIP Conf. Proc.* 2182 (2019) 050006.
17. A. Yamazaki, K. Sasa, S. Tomita, S. Ishii, H. Naramoto, M. Sataka, H. Kudo, G. Itoh, and M. Ohkubo, “Microscopic 3-dimensional mapping of hydrogen bubbles in polycrystalline Al by elastic recoil detection analysis under transmission geometry”, *AIP Advances* 9 (2019) 105111.
18. Y. Shiina, R. Kinoshita, S. Funada, M. Matsuda, M. Imai, K. Kawatsura, M. Sataka, K. Sasa, and S. Tomita, “Measurement of Auger electrons emitted through Coster-Kronig transitions under irradiation of fast C₂⁺ ions”, *Nucl. Instrum. Methods B* 460 (2019) 30.
19. S. Goto, H. Kura, H. Yanagihara, E. Kita, M. Tsujikawa, R. Sasaki, M. Shirai, Y. Kobayashi, T. Honda, and K. Ono, “Positive Weiss temperature in layered antiferromagnetic FeNiN for high-performance permanent magnets”, *ACS Appl. Nano Mater.* 2 (2019) 6909.

20. H. Latiff, M. Kishimoto, J. Inoue, E. Kita, H. Yanagihara, and T. Devillers, “Strain-induced magnetic anisotropy via the Jahn-Teller effect and the magnetoelastic coupling of tetragonally distorted (Cu,Co)Fe₂O₄ particles”, J. Magn. Magn. Mater. 489 (2019) 165380.
21. Y. Hase, K. Satoh, A. Chiba, Y. Hirano, S. Tomita, Y. Saito, and K. Narumi, "Experimental study on the biological effect of cluster ion beams in bacillus subtilis spores", Quantum Beam Sci. 3 (2019) 8.
22. S. Fujiwara, Y. Kurauchi, Y. Hirose, I. Harayama, D. Sekiba, T. Hasegawa, “Modification of electrical and magnetic properties of Fe₃O₄ epitaxial thin films by nitrogen substitution for oxygen”, ACS Applied Electronic Materials 1 (2019) 595.
23. D. Kutsuzawa, Y. Hirose, Y. Sugisawa, J. Kikuda, D. Sekiba, and T. Hasegawa, “Enhanced ferromagnetic transition temperature in NdO_xDy epitaxial thin films”, Phys. Rev. Mater. 3 (2019) 044408.
24. R. Kitahara, K. Hirota, S. Ieki, T. Ino, Y. Iwashita, M. Kitaguchi, J. Koga, K. Mishima, A. Morishita, N. Nagakura, H. Oide, H. Otono, Y. Seki, D. Sekiba, T. Shima, H. M. Shimizu, N. Sumi, H. Sumino, K. Taketani, T. Tomita, T. Yamada, S. Yamashita, M. Yokohashi, and T. Yoshioka, “Improved accuracy in the determination of the thermal cross section of ¹⁴N(n, p)¹⁴C for neutron lifetime measurement”, Prog. Theor. Exp. Phys. 093C01 (2019).
25. I. Harayama, T. Tamura, S. Ishii, K. Ozeki, and D. Sekiba, “Improvement of detection limit for hydrogen in high-resolution ERDA by using scanning solid state detector”, Nucl. Instrum. Methods B 456 (2019) 74.
26. D.J. Junttila, K. Yoneda, and I. Suzuki, “Genetic modification of the thraustochytrid *Aurantiochytrium* sp. 18W-13a for cellobiose utilization by secretory expression of β-glucosidase from *Aspergillus aculeatus*”, Algal Res. 40 (2019) 101503.
27. C. Degraeve-Guilbault C., R.E. Gomez, C. Lemoigne, N. Pankasem, S. Morin, K. Tuphile, J. Joubes, J. Jouhet, J. Gronnier, I. Suzuki, D. Frédéric, and F. Corellow, “Plastidic Δ6 fatty-acid desaturases with distinctive substrate specificity regulate the pool of c18-pufas in the ancestral picoalga *Ostreococcus tauri*” bioRxiv, doi: <https://doi.org/10.1101/2020.03.10.986216> (2020)

6.2 Reviews and books

1. T. Matsunaka and K. Sasa, Chapter 6.4, “Distribution and migration of radioiodine in terrestrial environment”, Environmental Contamination from the Fukushima Nuclear Disaster, Cambridge

6.3 Poster and oral presentations at academic meetings

1. A. Uedono, W. Egger, C. Hugenschmidt, and S. Ishibashi, “Control of vacancy-type defects in Mg implanted GaN studied by positron annihilation spectroscopy”, SPIE Photonics West, OPTO, San Francisco, USA (Feb. 4, 2020). (Invited talk)
2. S.F. Chichibu, K. Shima, K. Kojima, S. Ishibashi, and A. Uedono, “Origin and dynamic properties of major intrinsic nonradiative recombination centers in wide bandgap nitride semiconductors”, SPIE Photonics West, OPTO, San Francisco, USA (Feb. 4, 2020). (Invited talk)
3. A. Uedono, W. Egger, T. Koschine, C. Hugenschmidt, M. Dickmann, M. Sumiya, and S. Ishibashi, “Open spaces in Al₂O₃ film deposited on widegap semiconductors probed by monoenergetic positron beams”, American Vacuum Society Int. Sym. Ohio, USA (Oct. 23, 2019). (Invited talk)
4. A. Uedono, W. Egger, T. Koschine, C. Hugenschmidt, M. Dickmann, and S. Ishibashi, “Annealing behaviors of open spaces in thin Al₂O₃ films deposited on semiconductors studied using monoenergetic positron beams”, 15th Int. Workshop Slow Positron Beam Techniques and Applications, Prague, Czech Republic (Sept. 3, 2019). (Invited talk)
5. S.F. Chichibu, K. Shima, K. Kojima, S. Ishibashi, and A. Uedono, “Impact of Vacancy Complexes on the Nonradiative Recombination Processes in III-N Devices”, 13th Int. Conf. Nitride Semiconductors, Bellevue, USA (Jul. 10, 2019). (Invited talk)
6. A. Uedono, W. Egger, C. Hugenschmidt, and S. Ishibashi, “Vacancy-type defects in GaN-based power device structure - defect characterization in ion implanted GaN and Al₂O₃/GaN -“, Compound Semiconductor Week 2019, Nagoya, Japan (May 22, 2019). (Invited talk)
7. T. Yamaguchi, “ILIMA status report and phase-0 program”, Nuster Week 2019, CNRS, Gif-sur-Yvette, France (Sept. 23–27, 2019). (Invited talk)
8. Y. Shiina, R. Kinoshita, S. Funada, S. Tomita, M. Matsuda, M. Imai, K. Kawatsura, M. Sataka, and K. Sasa, “Cluster effect on the yield of Auger electrons emitted through Coster–Kronig transitions”, ISIAC, XXXIst International Conference on Photonic, Electronic, and Atomic Collisions, Deauville, France (Jul. 23–30, 2019). (Invited Talk)
9. H. Matsumura, G. Yoshida, A. Toyoda, K. Masumoto, K. Nishikawa, H. Nakamura, T. Miura,

- K. Bessho, K. Sasa, T. Moriguchi, F. Nobuhara, and Y. Nagashima, “Nondestructive high-sensitivity measurement method for activation estimation in accelerator room concrete”, The 10th International Symposium on Radiation Safety and Detection Technology (ISORD-10), Taiyuan, China (Jul. 16-19, 2019). (Invited Talk)
10. 笹 公和, ”イオンビーム分析法を用いた材料中の水素を含む多元素同時イメージング”, 軽金属学会 アルミニウム中の水素と材料物性研究部会第 2 回研究会, 日本アルミニウム協会東京事務所, 東京 (2019 年 11 月 6 日). (招待講演)
 11. 鈴木石根, ”光合成の環境適応からカーボンリサイクル”, 第 138 回バイオ e-カフェ, 筑波大学, つくば (2019 年 11 月 12 日). (招待講演)
 12. 岩田康嗣, ”加速器を利用した Protist 遺伝子変異”, 第 58 回つくば藻類プロティストフォーラム, 筑波大学, つくば(2019 年 10 月 7 日). (招待講演)
 13. Y. Iwata, R. Morioka, I. Suzuki, K. Tomita, N. Orita, T. Matsumoto, A. Masuda, and K. Sasa, ”Mutagenesis to the target genes of microalgae with the ^{15}N -resonant nuclear reaction”, 27th European Advanced Materials Congress, Stockholm, Sweden (Aug. 11–14, 2019). (Invited talk)
 14. A. Uedono, “Current trends of electronics and a study of defects in materials for semiconductor devices”, Martin Luther University, Halle, Germany (Nov. 7-8, Jun. 19–20, 2019).
 15. A. Uedono, W. Egger, T. Koschine, C. Hugenschmidt, M. Dickmann, and S. Ishibashi, “Vacancy-type defects in ion-implanted GaN probed by monoenergetic positron beams”, MLZ User Meeting 2019, Munich, Germany (Dec. 10, 2019).
 16. C. Vallee, M. Bonvalot, B. Pelissier, J.-H. Tortai, S. David, S. Belahcen, V. Pesce, M. Jaffal, A. Bsiesy, R. Gassilloud, N. Posseme, T. Grehl, P. Bruner, and A. Uedono, “In line and ex situ metrology and characterization to enable area selective deposition”, American Vacuum Society Int. Sym., Columbus, USA (Oct. 22, 2019).
 17. K. Shima, H. Iguchi, T. Narita, K. Kataoka, K. Kojima, A. Uedono, and S.F. Chichibu, “Photoluminescence studies of sequentially Mg and H ion-implanted GaN with various implantation depths and crystallographic planes”, 13th Int. Conf. Nitride Semiconductors, Bellevue, USA (Jul. 10, 2019).
 18. M. Zhao, V. Spampinato, A. Franquet, D. Hein, L. Chang, and A. Uedono, “The influence of AlN nucleation layer on radio frequency (RF) Transmission Loss of GaN-on-Si Structure”, 13th Int. Conf. Nitride Semiconductors, Bellevue, USA (Jul. 9, 2019).

19. S. Takashima, R. Tanaka, K. Ueno, H. Matsuyama, Y. Fukushima, M. Edo, K. Shima, K. Kojima, S.F. Chichibu, and A. Uedono, “Evaluation of subsequent implantation effect into Mg implanted region in GaN”, 13th Int. Conf. Nitride Semiconductors, Bellevue, USA (Jul. 8, 2019).
20. 秩父重英, 嶋 紘平, 小島一信, Moody Baxter, 三田清二, Collazo Ramon, Sitar Zlatko, 熊谷義直, 上殿明良, “PVT 成長 AlN 上に HVPE 成長させた Si 添加 AlN 基板の陰極線蛍光評価”, 第 67 回応用物理学会春季学術講演会, 上智大学, 東京 (2020 年 3 月 12–15 日).
21. 嶋 紘平, 中須大蔵, 正直花奈子, 上杉謙次郎, 小島一信, 上殿明良, 三宅秀人, 秩父重英, “高温アニールしたスパッタ AlN 上に成長させた AlN の陰極線蛍光評価(1)”, 第 67 回応用物理学会春季学術講演会, 上智大学, 東京 (2020 年 3 月 12–15 日).
22. 中須大蔵, 嶋 紘平, 正直花奈子, 上杉謙次郎, 小島一信, 上殿明良, 三宅秀人, 秩父重英, “高温アニールしたスパッタ AlN 上に成長させた AlN の陰極線蛍光評価(2)”, 第 67 回応用物理学会春季学術講演会, 上智大学, 東京 (2020 年 3 月 12–15 日).
23. 上殿明良, 上野 航, 細井卓治, W. Egger, T. Koschine, C. Hugenschmidt, M. Dickmann, 渡部平司, “陽電子消滅による SiO₂/GaN 構造の空隙と空孔型欠陥の検出”, 第 67 回応用物理学会春季学術講演会, 上智大学, 東京 (2020 年 3 月 12–15 日).
24. 角谷正友, 高原悠希, 矢代秀平, 本田 徹, Dickerson Kindole, 竹端寛治, 今中康貴, 上殿明良, “InGaN/GaN ヘテロ構造成長における AlN テンプレートの変化”, 第 67 回応用物理学会春季学術講演会, 上智大学, 東京 (2020 年 3 月 12–15 日).
25. 秩父重英, 小島一信, 羽豆耕治, 石川陽一, 古澤健太郎, 三田清二, Collazo Ramon, Sitar Zlatko, 上殿明良, “気相成長 m 面自立 AlN 基板およびホモエピタキシャル層の偏光特性と発光ダイナミクス”, 第 80 回応用物理学会秋季学術講演会, 北海道大学, 札幌 (2019 年 9 月 19 日).
26. N. Nitta, Y. Murao, H. Tsuchida, S. Tomita, K. Sasa, K. Hirata, H. Shibata Y. Hirano K. Yamada, A. Chiba, Y. Saitoh, K. Narumi, and Y. Hoshino, “Surface structures on Ge and Si irradiated with C60 cluster ion beams”, 23rd International Workshop on Inelastic Ion-Surface Collisions (IISC-23), Matsue, Japan (Nov.17–22, 2019).
27. 景澤怜央 他, “固体水素標的を用いた ¹⁷F の反応断面積測定”, 日本物理学会第 75 回年次大会、名古屋大学, 名古屋 (2020 年 3 月 16–19 日).

28. T. Moriguchi et al., “Energy dependence of reaction cross section for ^{17}Ne on proton target”, The International Nuclear Physics Conference (INPC) 2019, Scottish Event Campus, Glasgow, UK (Jul. 29–Aug. 2, 2019).
29. A. Ozawa et al., “Mass measurements for Ni-isotopes in Rare-RI Ring RIBF”, China-Japan Collaboration Workshop on “Nuclear Mass and Life for Unraveling Mysteries of R-process”, ITP/CAS, Beijing, China (Oct. 9–12, 2019).
30. 向井もも 他, “薄膜を利用した飛行時間検出器の開発”, 日本物理学会 2019 年秋季大会, 山形大学, 山形 (2019 年 9 月 17- 20 日).
31. M. Mukai et al., “Measurement of nuclear magnetic dipole moments of $^{196-198}\text{Ir}$ from laser spectroscopy at KISS”, INPC2019, Glasgow, UK (Jul. 28–Aug. 2 2019).
32. T. Yamaguchi et al., “New experimental plan and detector R&D at the Rare-RI Ring facility”, China-Japan Collaboration Workshop on “Nuclear Mass and Life for Unraveling Mysteries of R-process”, ITP/CAS, Beijing, China (Oct. 9–12, 2019).
33. K. Sasa, M. Matsumura, T. Matsunaka, T. Takahashi, Y. Satou, N. Kinoshita, H. Matsuzaki, and K. Sueki, “Distribution of ^{129}I in the terrestrial environment around the Fukushima Daiichi Nuclear Power Plant before and after the accident”, 5th International Conference on Environmental Radioactivity, Prague, Czech Republic (Sept. 8–13, 2019).
34. Y. Ochiai, K. Sasa, Y. Tosaki, T. Takahashi, M. Matsumura, and K. Sueki, “Variation of Chlorine-36 deposition flux in precipitation at Tsukuba, Japan”, 5th International Conference on Environmental Radioactivity, Prague, Czech Republic (Sept. 8–13, 2019).
35. K. Sasa, T. Takahashi, M. Matsumura, Y. Ochiai, T. Matsunaka, A. Sakaguchi, H. Shen, and K. Sueki, “Progress of ultrasensitive detection techniques for the 6 MV multi-nuclide AMS system at the University of Tsukuba”, The 8th East Asia Accelerator Mass Spectrometry Symposium (EA-AMS 8), Nagoya University, Nagoya, Japan (Dec. 3–6, 2019).
36. K. Kanzawa, F. Miyake, Y. Tada, K. Horiuchi, K. Ohtani, K. Sasa, Y. Motizuki, K. Takahashi, Y. Nakai, H. Motoyama, and H. Matsuzaki, “Variation of cosmogenic ^{10}Be for cosmic ray event in ~5480 BC from Antarctic Dome Fuji ice core”, The 8th East Asia Accelerator Mass Spectrometry Symposium (EA-AMS 8), Nagoya University, Nagoya, Japan (Dec. 3–6, 2019).

37. Y. Ochiai, K. Sasa, Y. Tosaki, T. Takahashi, M. Matsumura, and K. Sueki, “Variations of Beryllium-10 and Chlorine-36 deposition flux at Tsukuba, Japan”, The 8th East Asia Accelerator Mass Spectrometry Symposium (EA-AMS 8), Nagoya University, Nagoya, Japan (Dec. 3–6, 2019).
38. 笹 公和, 石井 聡, 高橋 努, 大和良広, 田島義一, 松村万寿美, 森口哲朗, 上殿明良, “筑波大学タンデム加速器施設 UTTAC の現状(2018 年度)”, 第 32 回タンデム加速器及びその周辺技術の研究会, 神戸大学, 神戸 (2019 年 7 月 5–6 日).
39. 笹 公和, 石井 聡, 高橋 努, 大和良広, 田島義一, 松村万寿美, 森口哲朗, 上殿明良, “筑波大学タンデム加速器施設の現状報告”, 第 16 回日本加速器学会年会, 京都大学, 京都 (2019 年 7 月 31 日 – 8 月 3 日).
40. 笹 公和, 落合悠太, 高橋 努, 松村万寿美, 末木啓介, “カルシウム 41 の加速器質量分析法による高感度検出手法の開発”, 2019 年第 80 回応用物理学会秋季学術講演会, 北海道大学, 札幌 (2019 年 9 月 18–21 日).
41. 菅澤佳世, 三宅美沙, 堀内一穂, 笹 公和, 望月優子, 高橋和也, 中井陽一, 本山秀明, 松崎浩之, “ドームふじアイスコア中 ^{10}Be と ^{36}Cl 濃度の測定による BC5480 年宇宙線イベントの調査”, 山形大学, 山形 (2019 年 9 月 17–20 日).
42. 落合悠太, 笹 公和, 高橋 努, 松村万寿美, 末木啓介, “加速器質量分析法を用いた塩素 36 測定における低バックグラウンド検出手法の開発”, 2019 年第 80 回応用物理学会秋季学術講演会, 北海道大学, 札幌 (2019 年 9 月 18–21 日).
43. 横山大輝, 笹 公和, 松中哲也, 高橋 努, 松村万寿美, 高野健太, 落合悠太, 長谷川 涼, 太田裕貴, 末木啓介, “福島県の避難指示区域における I-129 の分布と Cs-137 との関係性”, 日本放射化学会第 63 回討論会(2019), いわき産業創造館, いわき (2019 年 9 月 24–26 日).
44. 松中哲也, 笹 公和, 高橋 努, 松村万寿美, 末木啓介, 松崎浩之, “樹木年輪に記録された福島第一原子力発電所発事故由来 C-14 の分布”, 日本放射化学会第 63 回討論会(2019), いわき産業創造館, いわき (2019 年 9 月 24–26 日).
45. 松村万寿美, 森口哲朗, 笹 公和, 上殿明良, “筑波大学 6MV タンデム加速器ビームラインの放射線サーベイ”, 公益社団法人日本アイソトープ協会 放射線安全取扱部会年次大会, 倉敷市芸文館, 倉敷 (2019 年 10 月 24–25 日).
46. 松中哲也, 後藤章夫, 渡邊隆広, 土屋範芳, 平野伸夫, 笹 公和, “蔵王山における火山活動と熱水系ヨウ素同位体比の変動”, 日本陸水学会 第 84 回金沢大会, 金沢大学, 金沢 (2019 年

9月27–30日).

47. 菰田誉大, 村尾吉輝, 新田紀子, 土田秀次, 富田成夫, 笹 公和, 平田浩一, 柴田裕実, 平野貴美, 山田圭介, 千葉敦也, 斉藤勇一, 鳴海一雅, 星野 靖, ”C60 クラスターイオンを照射した Si の照射角度依存性”, QST 高崎サイエンスフェスタ 2019, 高崎シティギャラリー, 高崎 (2019 年 12 月 10–11 日).
48. 菅澤佳世, 三宅美沙, 多田悠馬, 堀内一穂, 大谷 昂, 笹 公和, 高橋 努, 松村万寿美, 落合悠太, 望月優子, 高橋和也, 中井陽一, 本山秀明, 松崎浩之, ”BC5480 年宇宙線イベントにおける ^{10}Be と ^{36}Cl の変動 : ドームふじアイスコアからの証拠”, 応用物理学会 2020 年春季学術講演会, 上智大学, 東京 (2020 年 3 月 12–15 日).
49. 笹 公和, 山崎明義, 石井 聡, 富田成夫, 左高正雄, 檜本 洋, 工藤 博, “構造材料用マイクロビーム分析装置を用いた水素を含む多元素同時分析法の開発”, 応用物理学会 2020 年春季学術講演会, 上智大学, 東京 (2020 年 3 月 12–15 日).
50. S. Tomita, S. Shiki, G. Fujii, and M. Ukibe, “Characteristics of kinetic energy sensitive detection of keV particles using superconducting tunnel junction”, 23rd International Workshop on Inelastic Ion-Surface Collisions, Matsue, Japan (Nov. 17–22, 2019).
51. 富田成夫, 志岐成友, 藤井 剛, 浮辺雅弘, “超伝導トンネル接合検出器のイオン検出特性”, 応用物理学会秋季学術講演会, 北海道大学, 札幌 (2019 年 9 月 18–21 日).
52. 新家弘也, 副島敬佑, 山下 晃, 岩田康嗣, 長谷純宏, 大野 豊, 鈴木石根, “重イオンビーム照射変異によるオイル分解抑制藻の解析, QST 高崎サイエンスフェスタ 2019, 高崎シティギャラリー, 高崎 (2019 年 12 月 10–11 日).
53. T. Inada and I. Suzuki, “Production of the ω -1 hydroxy fatty acids in *Synechocystis* sp. PCC 6803”, 12th International Marine Biotechnology Conference, Shimidzu, Japan (Sept. 9–12, 2019).
54. N. Pankasem, R.K. Bakku, S. Machida, F. Corellou, F. Domergue, N. Nomura, and I. Suzuki, “Substrate specificity of the cytochrome b5 -containing $\Delta 6$ fatty acid desaturase localized in the chloroplast of the marine prasinophyte, *Ostreococcus tauri*”, 12th International Marine Biotechnology Conference, Shimidzu, Japan, (Sept. 9–12, 2019).
55. M. Junaid, A. Otero, and I. Suzuki, “Development of the reversible regulatory system for gene expression using an acyl-homoserine lactone-mediated sensor and a lactonase in the cyanobacterium *Synechocystis* sp. PCC 6803”, 12th International Marine Biotechnology

Conference, Shimidzu, Japan (Sept. 9-12, 2019).

56. T. Kashiwagi, K. Hayashi, M. Yoshimura, and I. Suzuki, “Development of a device for efficient dissolution of carbon dioxide into the mass culture of algae”, 12th International Marine Biotechnology Conference, Shimidzu, Japan (Sept. 9–12, 2019).
57. 岩田康嗣, 鈴木石根, 鈴木裕司, 細田 忍, 西川暢子, “ ^{15}N 共鳴核反応による微細藻標的遺伝子改変とエネルギー生産性利用を目指して”, 第7回「機能性バイオ」ミニシンポ, 東京大学, 東京 (2019年7月4日).
58. Y. Sugisawa, D. Sekiba, I. Harayama, “Development of low-energy TOF-E telescope ERDA for depth profiling of light elements at UTTAC in the University of Tsukuba”, 24th International Conference on Ion Beam Analysis, Antibes, France (Oct. 13–18, 2019).
59. 杉澤悠紀, 関場大一郎, 廣瀬 靖, 原山 勲, “多層膜中軽元素の深さ分布測定に向けた TOF-E telescope ERDA 装置の開発”, 日本物理学会 2019 年秋季大会, 岐阜大学, 岐阜 (2019 年 9 月 10–13 日).
60. 岡部宏紀, 日野正裕, 広田克也, 家城 斉, 猪野 隆, 岩下芳久, 北口雅暁, 北原龍之介, 古賀 淳, 三島賢二, 森下 彩, 中野祐輔, 長倉直樹, 小田達郎, 生出秀行, 音野瑛俊, 関 義親, 関場大一郎, 嶋 達志, 清水裕彦, 角 直幸, 角野浩史, 竹谷 薫, 富田龍彦, 上原英晃, 山田崇人, 山下 了, 横橋麻美, 吉岡瑞樹, “J-PARC/BL05 における中性子寿命測定実験: SFC アップグレード”, 日本物理学会 2019 年秋季大会, 山形大学, 山形 (2019 年 9 月 17–20 日).
61. 三島賢二, 広田克也, 家城 斉, 猪野 隆, 岩下芳久, 梶原昇吾, 加藤 悠, 北口雅暁, 北原龍之介, 古賀 淳, 牧瀬 壮, 茂木駿紀, 森下 彩, 長倉直樹, 中野祐輔, 生出秀行, 岡部宏紀, 音野瑛俊, 関 義親, 関場大一郎, 嶋 達志, 清水裕彦, 杉澤悠紀, 角 直幸, 角野浩史, 竹谷 薫, 田辺友彦, 富田龍彦, 上原英晃, 山田崇人, 山下 了, 矢野浩大, 横橋麻美, 吉岡瑞樹, “J-PARC/BL05 における中性子寿命測定実験: ^3He 数密度導出法の改良”, 日本物理学会 2019 年秋季大会, 山形大学, 山形 (2019 年 9 月 17–20 日).
62. 市川 豪, 広田克也, 家城 斉, 猪野 隆, 岩下芳久, 梶原昇吾, 加藤 悠, 北口雅暁, 北原龍之介, 古賀 淳, 牧瀬 壮, 三島賢二, 茂木駿紀, 森川滉己, 森下 彩, 長倉直樹, 中野祐輔, 生出秀行, 岡部宏紀, 音野瑛俊, 関 義親, 関場大一郎, 嶋 達志, 清水裕彦, 杉澤悠紀, 角 直幸, 角野浩史, 竹谷 薫, 田辺友彦, 富田龍彦, 上原英晃, 山田崇人, 山下 了, 矢野浩大, 横橋麻美, 吉岡瑞樹, “J-PARC/BL05 における中性子寿命測定実験: バックグラウンドと系統誤差の評価”, 日本物理学会第 75 回年次大会, 名古屋大学, 名古屋 (2020 年 3 月 16–19 日).

63. 森川滉己, 広田克也, 市川 豪, 家城 斉, 猪野 隆, 岩下芳久, 梶原昇吾, 加藤 悠, 北口雅暁, 北原龍之介, 古賀 淳, 牧瀬 壮, 三島賢二, 茂木駿紀, 森下 彩, 長倉直樹, 中野祐輔, 生出秀行, 岡部宏紀, 音野瑛俊, 關 義親, 関場大一郎, 嶋 達志, 清水裕彦, 杉澤悠紀, 角 直幸, 角野浩史, 竹谷 薫, 田辺友彦, 富田龍彦, 上原英晃, 山田崇人, 山下 了, 矢野浩大, 横橋麻美, 吉岡瑞樹, “J-PARC/BL05 における中性子寿命測定実験 : TPC 動作ガス中の ^3He 含有率評価”, 日本物理学会第 75 回年次大会、名古屋大学, 名古屋 (2020 年 3 月 16–19 日).
64. 岡部宏紀, 日野正裕, 広田克也, 家城 斉, 猪野 隆, 岩下芳久, 北口雅暁, 北原龍之介, 古賀 淳, 三島賢二, 森下 彩, 中野祐輔, 長倉直樹, 小田達郎, 生出秀行, 音野瑛俊, 關 義親, 関場大一郎, 嶋 達志, 清水裕彦, 角 直幸, 角野浩史, 竹谷 薫, 富田龍彦, 上原英晃, 山田崇人, 山下 了, 横橋麻美, 吉岡瑞樹, “J-PARC/BL05 における中性子寿命測定実験 : SFC アップグレード”, 日本物理学会第 75 回年次大会、名古屋大学, 名古屋 (2020 年 3 月 16–19 日).
65. 福本通孝, 廣瀬 靖, 杉澤悠紀, 関場大一郎, 長谷川哲也, “パイクロア型 $\text{Sn}_2\text{Ta}_2\text{O}_7$ エピタキシャル薄膜への p 型ドーピング”, 応用物理学会 2020 年春季学術講演会, 上智大学, 東京 (2020 年 3 月 12–15 日).

6.4 UTTAC seminars

- 2019.10.21 Neutron skins of Ca isotopes across neutron magic number $N=28$, *Masaomi Tanaka* (*Research Center for Superheavy Elements, Kyushu University*)
- 2019.10.31 Passivation and Compensation of Mg-doping in GaN and AlGaIn, *Andrew Klump* (*North Carolina State University*)
- 2019.11.8 Introduction of materials science studies by means of the beta-NMR technique, *Mototsugu Mihara* (*Osaka University*)
- 2019.11.14 Nano-Scale Materials Modification and Materials Analysis, *Leonard C. Feldman* (*Rutgers University*)
- 2019.11.14 Observation of quantum diffusion of hydrogen in Palladium by electrical measurement, *Takahiro Ozawa* (*University of Tokyo*)
- 2019.11.14 Proposal of site-selective electronic structure investigation by ion beam, *Daiichiro Sekiba* (*University of Tsukuba*)
- 2019.11.14 High-resolution imaging of soft materials and direct nano-patterning of graphene by helium ion microscopy, *Shinichi Ogawa* (*National Institute of Advanced Industrial Science and Technology [AIST]*)
- 2020.1.7 Neutral mesons production in jets in p-Pb collisions at $\sqrt{s_{NN}} = 5.02$ TeV in LHC-ALICE experiment, *Masahiro Takamura* (*University of Tsukuba*)
- 2020.1.7 Elliptic flow of electrons from heavy-flavour hadron decays in Pb-Pb collisions at $\sqrt{s_{NN}} = 5.02$ with ALICE at the LHC, *Kenichi Tadokoro* (*University of Tsukuba*)
- 2020.1.7 Fluctuation by unfolding of net-proton distribution in $\sqrt{s_{NN}} = 27$ GeV Au+Au collisions at the RHIC-STAR experiment, *Kana Nakagawa* (*University of Tsukuba*)
- 2020.1.7 Azimuthal anisotropic flow in Au+Au collisions with collider and fixed-target mode at $\sqrt{s_{NN}} = 7.7$ GeV with RHIC-STAR experiment, *Mina Hatakeyama* (*University of Tsukuba*)
- 2020.1.7 Azimuthal anisotropic flow of charged particles in Au+Au collisions at $\sqrt{s_{NN}} = 27$ GeV with RHIC-STAR experiment, *Yukiko Hoshi* (*University of Tsukuba*)

- 2020.1.7 Reaction cross section measurements for proton-rich nucleus ^{17}F using solid hydrogen target, *Reo Kagesawa (University of Tsukuba)*
- 2020.1.7 Variations of cosmogenic Be-10 and Cl-36 in rainwater with cosmic-ray intensity, *Yuta Ochiai (University of Tsukuba)*

7.

THESES



Writing down the new findings

Master theses

Miya Hashimoto	Measurement of trace-iodine isotope in the environment using mass spectrometry-application to marine chemistry
Reo Kagesawa	Reaction cross section measurements for proton-rich nucleus ^{17}F using solid hydrogen target
Yuta Ochiai	Variations of cosmogenic Be-10 and Cl-36 in rainwater with cosmic-ray intensity
Ruri Suganuma	Pulse height distribution of Channeltron signal for the detection of keV particles

Undergraduate theses

Natsuko Kishi	Determination of Li depth profile by nuclear reaction analysis
Kaito Nishizuka	Reconstruction of ^{14}C introduction history in the Japan Sea using a coral core sample

8.

LIST OF PERSONNEL



Emergency response training for the staff and students working in the experimental facilities including UTTAC.

Tandem Accelerator Complex

A. Uedono	Director, Professor
K. Sasa	Associate Professor
D. Sekiba	Lecturer
T. Moriguchi	Assistant Professor
Y. Tajima	Mechanical Engineer
S. Ishii	Mechanical Engineer
T. Takahashi	Electrical Engineer
Y. Yamato	Electrical Engineer
M. Matsumura	Technical Staff
S. Kuramochi	Administrative Staff
M. Satoh	Administrative Staff
H. Muromachi	Administrative Staff

Research Members¹

Division of Physics

A. Ozawa	T. Moriguchi	K. Sasa	M. Mukai
T. Yamaguchi (Cross appointment from Saitama University)			

Division of Applied Physics

E. Kita	D. Sekiba	S. Sharmin	S. Tomita
A. Uedono	H. Yanagihara		

Division of Geoscience

M. Kurosawa

Department of Biology

I. Suzuki

Division of Chemistry

K. Sueki	A. Sakaguchi	S. Yamasaki
----------	--------------	-------------

Division of Information and Systems

T. Kameda

¹ The “research members” include the authors and coauthors within 5 years back from this fiscal year, as well as the members of research projects running at UTTAC.

Staff of Open Advanced Facilities Initiative

H. Kudo H. Naramoto M. Satoka
K. Awazu (National Institute of Advanced Industrial Science and Technology [AIST])
S. Aoki (Comprehensive Research Organization for Science and Society [CROSS])

Graduate students

Graduate School of Pure and Applied Sciences, and Graduate School of Life and Environmental Sciences

Y. Liu	H. Onoda	H. Koizumi	Y. Sugisawa
Y. Ochiai	R. Kagesawa	K. Tomita	R. Suganuma
T. Itou	A. Ogura	N. Onozato	S. Yamada
M. Hashimoto	H. Yokoyama	R. Mase	M. Inoue
W. Ueno	S. Ando	R. Abe	Y. Takahara
R. Yaguchi	Y. Kurosaki		

Undergraduates

A. Taira	N. Kishi	K. Kimura	T. Okamoto
K. Nishizuka	Y. Gao	D. Hirose	K. Sakakura
T. Narita	K. Yoshimura		

External users and collaborators

Y. Iwata	National Institute of Advanced Industrial Science and Technology (AIST)
K. Tomita	National Institute of Advanced Industrial Science and Technology (AIST)
T. Ishizuka	National Institute of Advanced Industrial Science and Technology (AIST)
S. Shiki	National Institute of Advanced Industrial Science and Technology (AIST)
T. Matsunaka	Kanazawa University
Y. Inada	Saitama University
S. Hosoi	Saitama University
M. Sakaue	Saitama University
K. Yokota	Saitama University
D. Hamakawa	Saitama University
D. Kajiki	Saitama University
H. Tou	Saitama University
M. Fukami	Saitama University
F. Miyake	Nagoya University
K. Kanzawa	Nagoya University